

Azimuthal differences of quenched jets

D.L.D. Keijdener

A catalogue record is available from the Utrecht University Library

ISBN 978-94-6419-842-3

Copyright © 2023 by D.L.D. Keijdener

All rights reserved. No part of this book may be reproduced, stored in a database or retrieval system, or published in any form of any way, electronically, mechanically, by print, photoprint, microfilm, or any other means without prior written permission of the author. Typeset using \LaTeX . Printed by Gildeprint.

Azimuthal differences of quenched jets

Azimuthale verschillen in gequenchede jets

(met een samenvatting in het Nederlands)

Proefschrift

ter verkrijging van de graad van doctor aan de Universiteit Utrecht
op gezag van de rector magnificus, prof.dr. H.R.B.M. Kummeling,
ingevolge het besluit van het college voor promoties in het openbaar te verdedigen
op vrijdag 1 september 2023 des middags te 12.15 uur door

Darius Laurens David Keijdener
geboren op 15 oktober 1989 te Utrecht

Promotor: Prof. dr. R.J.M. Snellings

Copromotor: Dr. M. van Leeuwen

Beoordelingscommissie:

Prof. dr. C.F.F. Van Den Broeck

Dr. A. Ohlson

Prof. dr. J. Rojo

Prof. dr. S.J.G. Vandoren

Prof. dr. W. Verkerke

Contents

Prelude	10
1 The quark gluon plasma and jet quenching	11
1.1 QCD and the strong interaction	11
1.1.1 The strong force	13
1.1.2 Quark gluon plasma	14
1.2 Collider experiments	15
1.2.1 Kinematic variables and coordinate system	16
1.2.2 Heavy ion collisions	17
1.2.3 Multiplicity and centrality	17
1.3 Flow	17
1.3.1 Reaction plane and event plane	19
1.4 Jets	20
1.4.1 Parton energy loss and jet quenching	20
1.4.2 Jet definition	21
1.4.3 Measurements of jet quenching	22
1.5 Azimuthal dihadron correlations	28
1.5.1 Dihadron correlations	28
1.5.2 Dihadron correlations as convolutions	30
1.5.3 Event plane restriction	31
1.5.4 Background model with correlated event planes	34
1.5.5 Measurements in dihadron correlations	39
2 Toy Monte Carlo simulations	41
2.1 Setup	41
2.1.1 Implementation	42
2.2 Results	43
2.2.1 Event plane resolution/correlation factors	43
2.2.2 Quality of the fit	44
2.2.3 The quality of the errors resulting of the fit	45
2.3 Conclusion	51
3 The experimental environment	52
3.1 Large Hadron Collider	52

3.2	ALICE detector	53
3.2.1	Inner Tracking System (ITS)	55
3.2.2	Time Projection Chamber (TPC)	56
3.2.3	V0 detector	58
3.3	Event and track reconstruction	58
3.3.1	Event reconstruction	58
3.3.2	Track reconstruction	59
3.4	Software	61
4	The analysis	63
4.1	Analysis concept	63
4.2	Data selection	63
4.2.1	Cuts on events	64
4.2.2	Hybrid tracks	64
4.2.3	Cuts on track pairs	65
4.3	Efficiency corrections	67
4.3.1	Efficiency corrections from Monte-Carlo simulations	67
4.3.2	Dihadron efficiency from mixed events	68
4.4	Jet yield determination in pp	69
4.4.1	Weighted average projection	70
4.5	Jet yield determination in PbPb, with trigger selection	70
4.5.1	Fitting the background	70
4.5.2	Determining the interaction between event planes	73
4.5.3	Determining parameter consistency	79
4.5.4	Determining charged jet yield	79
4.6	Jet yield determination with low statistics	82
4.7	Jet yield determination in PbPb, without trigger selection	84
4.7.1	Determining background	84
4.7.2	Determining charged jet yield	85
4.8	Quality of the background fit	85
4.9	Systematic uncertainties	85
4.9.1	Uncertainty due to event and track cuts	85
4.9.2	Tension within the background fit	88
4.9.3	Inserting pp-jets into PbPb-collisions	89
4.9.4	Quantifying difference between fit methods	91
5	Analysis on Monte Carlo simulations	94
5.1	Generator	94
5.2	Similarities and differences with data	95
5.3	Event plane resolution in AMPT	96
5.4	Differences in the fitting procedure	97
5.5	Examples of the fit at low p_T	97
6	Results	101
6.1	Associated yield ratio	101
6.1.1	Results	101

6.1.2	Comparing background subtraction methods	102
6.1.3	Conclusion	102
6.2	Jet orientation yield ratio	106
6.2.1	Results	106
6.2.2	Comparing background subtraction methods	107
6.2.3	Conclusion	111
7	Conclusion and outlook	112
7.1	Summarised conclusions	112
7.2	Prospects with larger data samples	112
7.3	Differences between background models	113
7.3.1	Fourier-analysis	113
7.3.2	Simultaneous fit method	114
7.3.3	Background model extensions	114
7.4	Path length dependence	116
A	Fitting results	118
A.1	pp-collisions	118
A.2	PbPb-collisions, without trigger selection	118
A.3	PbPb-collisions, with selected trigger	118
B	Associated yield ratio	134
C	Comparison with other work	136
	Bibliography	137
	Samenvatting	143
	Summary	145
	Acknowledgements	147
	Curriculum Vitae	149

Prelude

The ancient Greek atomists posed that a smallest indivisible unit of matter existed, naming it the ‘atom’, the indivisible. This marked the start for a scientific search for finding these smallest building blocks of nature and the rules that govern them. Several times things previously assumed to be ‘atoms’ turned out to be in fact divisible. The most notable example hereof is the current scientifically defined atom. However scientists kept on searching for the smaller structures underneath those previous ‘atoms’.

I’m not aware of research about what sparks a fascination with this particular idea and its variations. Maybe this is due to that discovering such an ‘atom’ and the rules it is governed by, gives us the impression that all larger structures can be explained by ‘simply’ studying their underlying mechanics. It is not at all certain that larger scale systems can be easily understood from their building blocks. Considering, for instance, chaotic systems where the underlying rules are clear, but tiny variations in the beginning cause radically different behaviour. Nevertheless, the quest for ‘the most’ fundamental understanding of nature is probably one of the aspects that draws people to this research.

In this thesis we will discuss dihadron measurements of jet quenching, a phenomenon that can contribute to our understanding of the strong force. In order to do so, we will start with the underlying theory in chapter 1. In chapter 2 we will discuss a Toy Monte Carlo model that is used to test some newly introduced theory in chapter 1. The ALICE experiment, which provided the data on which this work is based, is discussed in chapter 3. Chapter 4 is devoted to an explanation of how the analysis is performed on the data. It is important, as we will explain in chapter 1, to compare such an analysis with an analysis that is as similar as possible on a sample of events generated by a physical model of heavy-ion collisions. This will be discussed in chapter 5 before in chapter 6 the results of both analyses will be discussed and compared. Chapter 7 will contain an discussion along with several avenues for improvement on this research.

Chapter 1

The quark gluon plasma and jet quenching

This chapter will begin with a very brief description the strong interaction, one of natures fundamental forces. After discussing some staples of, and definitions used in, collider experiments, we can discuss the topic of flow, which constitutes the background and the main challenge for this study. This is followed by a discussion of parton energy loss and jet quenching, leading up to the definition of a jet, which are the experimental signatures of high-energy quarks and gluons. This chapter is concluded by a discussion of dihadron correlations, the tool used in this work to study jet-like correlated partons.

1.1 QCD and the strong interaction

The current widely accepted description of reality at the smallest scale has been developed during the second half of the 20th century, and is somewhat generically called ‘the standard model’. It is a quantum field theory incorporating three of the four fundamental forces, the electromagnetic force, the weak force and the strong force. The fourth force, gravity, is not properly incorporated in the standard model, since as of yet there is not an agreed upon theory of quantum gravity that can be unified with the quantum field theory at the basis of the standard model. The corresponding particle description of the field theory of the standard model contains six quarks, six leptons and five force carrying bosons from Figure 1.1.¹

The electromagnetic force couples to all particles with an electric charge with the photon as its force carrier. The weak force interacts through the W and Z-bosons as its force carriers. Both forces have a large experimental history with, for instance Millikan’s experiment to determine the charge of the electron [61], as well as a range

¹The numbers dependent on the definition of ‘unique’ particle. Once can further distinguish particles and anti-particles, or a different colour charge, spin or helicity state.

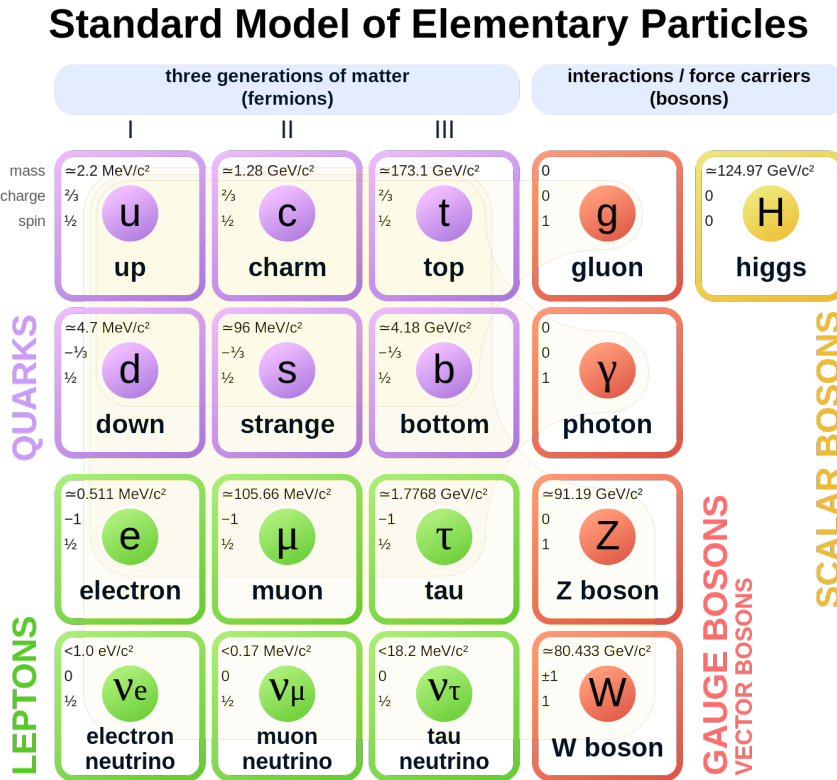


Figure 1.1: The standard model

Source: [44]

of experiments on the decay of unstable atoms and the Wu experiment to establish P-violation in the weak interaction.[81] With the advent of quantum field theory, it was relatively quickly realised by Glashow, Salam and Weinberg [64] that these forces could be unified in one electroweak theory.

1.1.1 The strong force

Probing the strong force, though, is considerably more challenging. The main culprit is the fact that at the current temperature and density of the universe, there is no such thing as a single, naked, colour charge, the corresponding charge for the strong force, as we will discuss later in this section. It is arguable that it is possible to study aspects of the strong force through the nuclear force, also known as the residual strong force, that binds nuclei together despite of them having only positive electric charges. But before Gell-Mann [52] and Zweig [83] posed that baryons and mesons were composed of quarks and gluons, there was no theoretical framework to study the strong force directly.

The current understanding of the strong force is formulated in a $SU(3)$ gauge theory: Quantum Chromo Dynamics (QCD). In a simplified picture it dictates that there are three different strong charges named colours. This name has been chosen because the three colour charges together become ‘white’. A ‘white’ object does not couple directly via the strong force. All quarks and antiquarks carry a colour charge: red, blue, green, anti-red, anti-blue or anti-green. This creates effectively 6 variants of any quark, which makes them able to bind together to hadrons in combinations that are colour neutral (or white). A baryon consists of three quarks (with either three different colours, or three anti-colours), and a meson consists of a colour-anti-colour pair. In theory all combinations with more colours, like pentaquarks, are also possible, as long as they are colour neutral. Recently, such states have also been found in experiments, though they are not stable over a longer period of time. [49]

Gluons are the force carriers that carry the force in strong interactions. Since the theory should allow two quarks with a different colour to interact strongly, it follows that the gluon has a colour charge in order to preserve colour in that interaction. This crucial difference with the electroweak force leads to a force that has wildly different behaviour and a theory that is harder to probe. It means that a gluons interact via the strong force with other gluons. This poses a huge complication for QCD, since the usual perturbative methods do not always apply. Higher order Feynman diagrams do not necessarily have lower contributions to the cross section of an interaction.

Another consequence of gluon self-interaction is that the coupling constant² of the strong force is not constant as a function of the momentum scale of the interaction. A compilation of measurements of this so called ‘running coupling constant’ are shown in Figure 1.2.

When a quark is separated from a hadron, the potential energy of the configuration increases rapidly due to the running coupling constant, until there is enough energy

²The theoretical quantity prescribing how strong the forces are with respect to each other and for one fundamental charge.

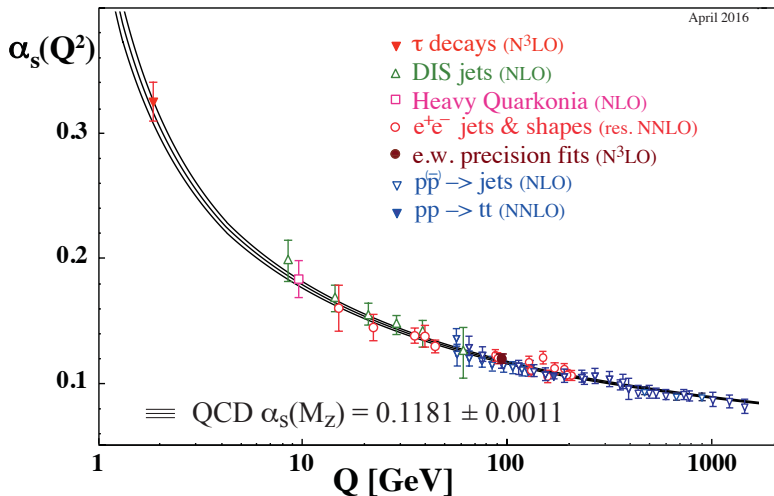


Figure 1.2: The running coupling constant.

Source: [26]

available to create a quark–anti-quark pair. The new pair is generated with a colour configuration that two new colourless hadrons can be formed.

1.1.2 Quark gluon plasma

The running of the strong coupling constant, and in particular the fact that the coupling becomes very large at momentum scales close to $\Lambda_{\text{QCD}} \approx 250$ MeV, mean that perturbative techniques have only limited application in theoretical calculations of QCD processes, whilst it is simultaneously hard to directly probe it through a naked charge. The field of plasma physics can provide an opportunity to study naked charges.

A plasma is a state of matter in which the mean free path of a particle (the average time before colliding into another particle) is shorter than the Debye screening length (the average length a force is active over).³ For the strong force this means that the distance between colour carriers is so short everywhere, that colour carriers at larger distances are ‘screened’, and their behaviour can be described by interactions with the average medium instead of single charges. This allows quarks to move freely in a sea of other quarks and gluons over distances much larger than the screening length. The deconfinement of quarks from hadrons allows closer study of the strong force in these free quarks. Being free in this context does not mean being free of the strong force, but it means that it will interact strongly with the collective plasma, instead of being confined to interactions within a hadron. On the theoretical side a QGP simplifies the situation as well. Since the coupling constant is small at short distances, it is possible to do some perturbative calculations in order to create predictions on

³This is slightly reductive, but it is the relevant restriction for this argument.

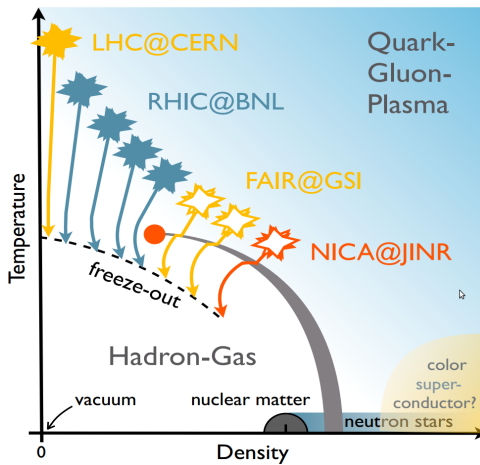


Figure 1.3: The QCD phase diagram, a schematic impression what the state of matter is depending on the net baryon density and temperature.

Source: [70]

everything from the initial hard scattering up to but not including the hadronization of the plasma.

Creating such a Quark-Gluon Plasma (QGP) requires a high energy density and temperature. Figure 1.3 shows the phase structure of QCD, as a function of net baryon density, i.e. the excess of quarks over anti-quarks on the horizontal axis, and the temperature on the vertical axis. Most of the hadronic matter in our known universe is currently in the form of protons, neutrons, and their bound combinations. This is represented by the dark grey ‘nuclear matter’ area in the diagram. Changing the net baryon density, the baryon density after subtracting the number of anti-baryons from baryons, or temperature in any possible direction will lead to a hadron gas, which covers most of the space in the low density and energy at the lower left corner. At large temperature and/or baryon density, strongly interacting matter enters the QGP phase. Between the two is a first order phase transition, with a critical point at the end of it. The exact location of the transition at higher baryonic density is not yet known. Results from lattice QCD show that the transition at a baryonic density of 0 is a cross-over. At high density there are indications it should be a first order transition. This would suggest there is a critical point somewhere in the middle regime.[45] Hypothetically the phase space also contains a colour superconductor phase at high density and low energy, where the colours are bound to quark flavours.[18]

1.2 Collider experiments

There is currently no known example of a Quark Gluon Plasma in nature that is accessible to study. However it is possible to create suitable conditions to produce

and study a QGP in a lab–environment at particle colliders. These are experimental installations where beams of particles moving in opposite direction are accelerated with electric fields to high velocities in a particle accelerator, before they are collided. In order to study QCD in the regime of high temperature and density, an experimental program to investigate high-energy collisions of heavy ions started in the 1980s. Initial experiments using collisions of high-energy beams with a fixed target showed that the energy densities achieved in these collisions are sufficient to form a QGP. A new generation of collider-based experiments, achieving much higher collision energies, started with the Relativistic Heavy Ion Collider in Brookhaven National Laboratory, and continues at even higher energy at the Large Hadron Collider at CERN. These collisions can create energy-densities high enough to create a short-lived QGP. This QGP quickly expands, cools, and hadronizes into baryons and mesons, and its remnants can be studied. The Large Hadron Collider and ALICE–detector used in this work will be discussed in Section 3.1 and Section 3.2 respectively. Figure 1.3 also indicates the parts of the phase diagram that can be probed with several modern and near-future colliders.

1.2.1 Kinematic variables and coordinate system

As always in a collision of two objects the description and resulting equations simplify by studying the collision in the centre of mass frame. In this frame, the centre of mass energy \sqrt{s} is equal to the sum of the energies of the incoming particles. By convention the z-axis is chosen as the direction along which the incoming beams travel just before the collision.

Given the overall rotational symmetry of the collisions around the beam axis, it is convenient to use an alternate coordinate system (p_T, η, ϕ) in lieu of the Cartesian momentum components. The transverse momentum p_T is the component of the momentum of a particle perpendicular to the beam axis. The azimuthal angle ϕ is the angle around the z-axis, measured between the x-axis of the experiment and the particle trajectory. For the longitudinal variable, it is convenient to use the rapidity y or pseudo-rapidity η . The rapidity

$$y = \frac{1}{2} \ln \frac{E + p_z c}{E - p_z c}, \quad (1.1)$$

where p_z is the momentum of the particle along the z-axis, is additive under Lorentz boosts along the beam axis. This is convenient since collisional remnants travel often at still near-light speeds. y can be interpreted as the hyperbolic angle of the Lorentz boost of the particle. In practice it is common to use the approximation

$$\eta = -\ln \left(\tan \frac{\theta}{2} \right), \quad (1.2)$$

with θ the angle between the track and the beam axis. Pseudo-rapidity approaches the rapidity for high energy particles and the quantities are equal for massless particles.

1.2.2 Heavy ion collisions

In heavy ion collisions there are clear signatures that suggest the formation of a hot and dense QGP, such as flow which we will discuss in Section 1.3. Studies into QGP often involve comparisons of certain quantities in heavy ion collisions with the same in pp-collisions at identical \sqrt{s} .

1.2.3 Multiplicity and centrality

For a heavy-ion collision the impact parameter b is defined as the distance between the centers of the nuclei in the plane perpendicular to the beam axis. Perfectly central collisions at $b = 0$ fm have all nucleons ‘participating’ in the collision and produce a lot of particles, while peripheral collision with a b slightly lower than 15 fm leave a large part of the nucleons as ‘spectators’ on their initial trajectory and as such produce less particles. Since the impact parameter is impossible to measure directly in an experimental context, usually the multiplicity N , the amount of particles produced, is used as a proxy to determine how central the collision is. The largest influence on the multiplicity is how many nucleons are involved in the collision, and this increases when the collision is more central. Each nucleon can collide multiple times to other nuclei, but the multiplicity is most tightly correlated with the number of participating nucleons in the collision N_{part} . This is modelled in a so-called Glauber model, which uses the nucleon distribution in both nuclei to model the number of participants and by extension the multiplicity as function of the impact parameter.[59] In principle fitting the multiplicity distribution to such a model could be used to translate the multiplicity to an estimated impact parameter,[60] or a number of participating nucleons, but in practice most experimental results are reported in centrality percentile bins due to the model dependence of a translation to impact parameter. These centrality bins are a model-independent measure of the multiplicity, where a number of randomly selected events can be divided in percentile classes. These percentile classes are then called centrality, with by convention the 0 – 1% centrality class the 1% events with the highest multiplicity and the lowest impact parameters.

1.3 Flow

The physical dimensions of the heavy ion collision also introduce asymmetries in azimuthal direction. The most obvious one is the second order asymmetry that emerges when the impact parameter is non-zero. This causes the overlap area between the incoming ions to take roughly the shape of a flattened American football like in Figure 1.4. This is the shape the emerging QGP takes, and when it starts expanding, it will do so in the direction of the highest pressure gradient, which is roughly in the direction inside the reaction plane: the plane spanned by the the vector of the beam axis and the vector between the centre of the colliding nuclei. This, and higher order asymmetries, create an azimuthal angle distribution of produced particles that can

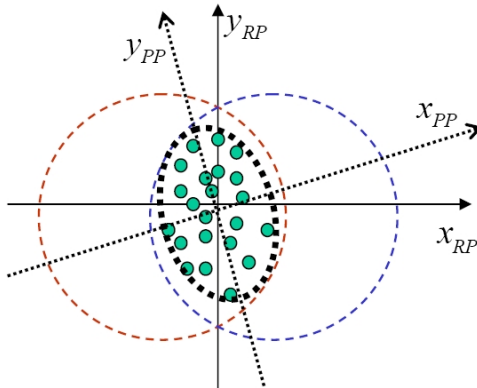


Figure 1.4: A schematic that illustrates the difference of the reaction plane (spanned by x_{RP} and z) and the participant plane (spanned by x_{PP} and z). It shows two colliding heavy ions, and the ellipsoid overlap volume between the two. x_{RP} lies in the direction through the middle of the colliding ions. y_{PP} is the major axis of the participant distribution in the transverse plane. The participant plane is the basis for the second order symmetry plane Ψ_2^{SP} .

Source: [78]

be expressed as a Fourier series:

$$\frac{dN}{d\phi}(\phi) = B \left(1 + \sum_{n=1}^{\infty} 2v_n \cos(n(\phi - \Psi_n^{SP})) \right), \quad (1.3)$$

where B is an average level, Ψ_n^{SP} is the angle of the symmetry plane (related to the reaction plane as we will discuss in more detail in Section 1.3.1) and v_n the n -th order flow coefficient. The flow coefficient v_n is defined as $\langle \cos(n(\phi_i - \Psi_n^{SP})) \rangle_{i \in \{1, \dots, N\}}$, an average of the cosine term for all N particles in the event. In this equation, the dependence of $\frac{dN}{d\phi}$ and v_n on transverse momentum, pseudorapidity, and centrality have been suppressed for the sake of readability. When studying a larger range of one of these dependent variables, one can substitute the flow coefficient for an effective value over that range. The average flow over a large p_T -range is often called an ‘integrated flow coefficient’.

The different orders in the Fourier series can have different symmetry planes Ψ_n^{SP} . Each order corresponds with some symmetry-axis in the initial state of the collision. The corresponding flow coefficients do decrease rapidly for increasing n . The v_2 is called the elliptic flow coefficient, and is heavily dependent on centrality due to the [19] initial shape of the overlapping area of the colliding ions. The triangular flow coefficient (v_3) and fourth order flow coefficient (v_4) are far smaller but still relevant for this work.

There is a variety of techniques to measure the flow coefficients in an experimental setting. In this study it is the main source of background present when measuring jets.

Flow coefficients will be determined indirectly with the help of a model (Section 1.5.4) and the study of dihadron histograms (Section 1.5). Because we will not directly determine flow coefficients, we will not discuss all of the many methods and results in this field. It suffices to say that flow parameters are a field of study in their own right, with subjects like multi-particle cumulants [29, 28] or studying it via Bessel transforms[77], and they contain valuable information on the properties of the QGP.

1.3.1 Reaction plane and event plane

Figure 1.4 illustrates the geometry of a non-central nuclear collision with the reaction plane and participant plane. As discussed before the reaction plane is a pre-collision quantity that is determined by the geometry of the incoming nuclei. The participant plane is the short axis of the shape of the participating nucleons in the collision, and it is a major contributor in the difference between the reaction plane and the symmetry plane, which is the symmetry plane of the resulting particles from the collision. Unfortunately, it is impossible to measure the reaction plane angle in practice due to the fact that the impact parameter is of the order of magnitude of 10^{-15} meter. Neither the participant nor the symmetry plane Ψ_n^{SP} can be detected directly, and therefor a proxy, the event plane Ψ_n^{EP} is used.

The second order event plane is the plane of the highest particle yield found inside the detector, and is therefor a approximation of the second order symmetry plane. It can be calculated using the Q -vector, the directivity or flow vector, of the event.[76, 78]

$$Q_n = (\sum_i w_i \cos(n\phi_i), \sum_i w_i \sin(n\phi_i)), \quad (1.4)$$

where the summation takes place over all particles in an event, with ϕ_i the azimuthal angle in the detector frame and w_i the weight associated to the particle. Ideally the weight w_i should be the $v_n(p_{T,i}, y_i)$, the n -th order flow coefficient for that particle. However, since v_n scales almost linearly with p_T ,[78] and we are only interested in the direction of Q_n , the choice $w_i = p_{T,i}$ suffices.

The direction of the flow vector Q_n is an experimental measure of the n -th order symmetry plane. Azimuthal anisotropy in the detector efficiency can cause small deviations. To correct for this effect the Q -vector is recentered, by subtracting the average Q_n vector over many events from each vector. This procedure is justified due to the fact that there is no preferred direction of the event plane in the laboratory. In order to retrieve the event plane angle Ψ_n^{EP} , we can take the inverse tangent of $Q_{n,y}/Q_{n,x}$. Within the ALICE experiment, the common convention is to use the `arctan2` function from the C programming language, which maps a (x, y) point in a two-dimensional space to the angle with respect to the positive x-axis in the range $(-\pi, \pi]$, to find

$$\Psi_n^{\text{EP}} = \frac{1}{n} \text{arctan2}(Q_{n,x}, Q_{n,y}). \quad (1.5)$$

There are two reasons the event plane Ψ_n^{EP} is not equal to the reaction plane Ψ_n^{SP} which we are actually interested in. First of all the detector has a limited precision, and one can only measure the event plane based on a limited number of particles. Secondly an event has a finite multiplicity, and even with a perfect detector fluctuations would

cause deviations from the ideal plane. The amount of imprecision can be expressed via the event plane resolution

$$R_n = \langle \cos(n\Delta\Psi) \rangle \quad (1.6)$$

where $\Delta\Psi \equiv \Psi_2^{\text{SP}} - \Psi_2^{\text{EP}}$ is the difference between the two kinds of planes. The event plane resolution is dependent on the angular resolution or segmentation of the detector and angular differences in its efficiency and the multiplicity of the collision. It is also used as a correction factor when computing for instance the flow coefficients, and is therefore a commonly reported property. A common method to determine the event plane resolution is by subdividing the event into two and performing two independent measurements.

1.4 Jets

In order to get a clear understanding of a jet, we will first give a practical and intuitive description of a jet by discussing the parton shower and its usefulness as a probe for QCD. In Section 1.4.2 we will give the formal definition, alongside with some comments on some of the associated uncertainties of the first description. In Section 1.4.3 a selection of research in jet quenching is shown.

1.4.1 Parton energy loss and jet quenching

A pair of high energy scattering products is most certainly the result of a hard scattering between two partons in the collision. The outgoing partons fragment into a parton shower. After this fragmentation process, the resulting products, hadronize into baryons and mesons. From measurements on the production of direct photons and W/Z -bosons (that do not interact strongly with the medium), we know that the hard scattering process responsible for the creation of the initial partons is identical in pp -collisions and heavy ion collisions.[4] They can therefore act as hard probes to study the influence of the QGP on these partons and their fragmentation/hadronization products.

When travelling through the QGP, the constituents of the particle shower scatter with the plasma, which results in ‘energy loss’ of the shower and a boost of the low energy domain of the QGP.[67] Furthermore the shape of the shower changes, since it broadens[68] and the longitudinal momentum distribution of particles in the jet, known as the fragmentation function, changes. We would expect the size of those changes to be dependent on the path length the parton and its products have travelled through the QGP.

All these effects are described by Monte Carlo models that simulate the way that partons fragment and interact with the QGP and the subsequent hadronisation process. To compare these results to experimental data, we make use of jet algorithms to cluster fragments of parton showers in both experimental data and in theoretical calculations as an approximation of the theoretical idea. The collection of effects of the QGP on the parton shower is known as jet quenching. The comparison of measurements of jet quenching with theoretical models further restrict the parametrisation

of the models and the types of models themselves, leading to a better theoretical understanding of the process.

1.4.2 Jet definition

In pp -collisions, the parton shower is often quite isolated in space, and therefore a reasonable estimate can be made of which particles are actually part of the shower. There are several types of algorithms that group particles that are close together, called jet finding algorithms. In pp -collisions for most jets the energy of the jet will correspond with energy of the initial parton.

That becomes less clear when studying jets in heavy ion collisions, or for pp -collisions in cases where jets intersect with each other. The fragmentation products of the jet are technically indistinguishable from the hadronized results of the QGP itself and parts of other jets.⁴ As such it is good to keep in mind that ultimately the definition of a jet is dependent on the choices made during the analysis, in particular the jet algorithm. We work with a dihadron study in this work (Section 1.5), and as such measure jet signatures without directly interacting with this definition. But in generality there is some scientific consensus on two restriction that a jet finding algorithm should adhere to in order to produce consistent results in theoretical few-parton final states and in a full hadronic final state in experiments.[69]

- It should be infrared safe, meaning that the addition of low energetic particles should not suddenly change which jets are found. This is due to the fact that at low enough energy the particles generated in an event will not be found in an experimental setting, while on the theory-side the low energy spectrum is not well understood either since perturbative QCD does not suffice.
- It should be collinear safe, meaning that the p_T of a jet is not allowed to change significantly when one of its partons decays into two collinear partons. The jet finding algorithm should recognise that both decay products are still part of that particular jet, and add their momentum together to arrive at the total jet- p_T .

A common choice [43] for a jet finding algorithm is the anti- k_T algorithm.[31] It consecutively groups the pairs of ‘closest’ particles, starting with the high energetic ones, within a typical distance called the jet radius R , the Euclidean distance between two points in (η, ϕ) -space. It keeps on doing this until it considers all jets ‘done’ (having no more high momentum particles close enough to the jet) and assigned all particles in the event to a jet candidate.

This way the entire event is divided into areas that are jet candidates. Some of these candidates are not a product of a hard scattering but a combination of soft background. This problem is especially prevalent in heavy ion collisions where a

⁴And even in theory there are challenges to determine what counts as part of the jet. If a soft gluon is emitted by the jet in its direction and it interacts strongly with a gluon in the medium. Then are the gluons both part of the jet? Or is neither of them? Even counting one of them doesn’t specify which one you should count, since in a quantum mechanical picture it’s not possible to tell which one is the ‘original’.

dense background is present. These fake jets (alternatively called combinatorial jets) can be removed by placing restrictions on the jets.

Even if the jet candidate is a ‘true’ jet, associated with an energetic parton from hard scattering, it still contains background partons coming from hadronized QGP that just happens to be within the jet cone. Since there is no unique prescription for this subtraction, different experiments have used different approaches.[43] As a result, care has to be taken when comparing between different experimental results. It is often informative to compare multiple experimental results with a single event generator, which allows to apply the appropriate kinematic selections and background subtraction procedures to compare.

1.4.3 Measurements of jet quenching

Three types of measurements will be discussed here. The nuclear modification factor, di-jet asymmetries, and measurements on the fragmentation function. We will also discuss the broad implications the measurements have on the collective knowledge of jet physics. Section 1.5 will discuss a fourth approach, which is the basis for analysis in this work.

R_{AA} and R_{CP}

One of the simplest quantity that is sensitive to jet energy loss are the transverse momentum distributions of jet production. The ratio of jet production in pp-collisions versus heavy ion collisions is known as the jet nuclear modification factor R_{AA} , after it has been scaled by the factor of the average number of hard scatterings in a heavy ion collision.[43] To be precise

$$R_{\text{AA}}(p_T) = \frac{1}{\langle N_{\text{bin}} \rangle} \left(\frac{dN_{\text{AA}}}{dp_T} \Big/ \frac{dN_{\text{pp}}}{dp_T} \right), \quad (1.7)$$

with $\langle N_{\text{bin}} \rangle$ is the average number of binary nucleon-nucleon collisions. In this case dN_{AA}/dp_T and dN_{pp}/dp_T are transverse momentum distributions of charged particles or jets in the heavy ion collisions and pp-collisions respectively.

In order to verify the scaling of the hard production cross sections with the number of binary collisions, the R_{AA} has also been measured for direct photons and W and Z bosons. These do not interact strongly with the medium. Therefor the measurements of a R_{AA} around 1 for the W boson[4] can be used as proof that the production of high energetic partons in PbPb-collisions can be described as a superposition of pp-collisions.

For strong coupling particles, such as hadrons, this is not the case as can be seen in Figure 1.5. Studying the R_{AA} of particles with high transverse momentum already provides useful information on what happens with the remnants of hard scatterings in the collision, since high- p_T particles are unlikely to be formed in the background. These charged particle R_{AA} measurements [8, 22] are usually among the first analyses published on new data, given their relative simplicity. It is also possible to first

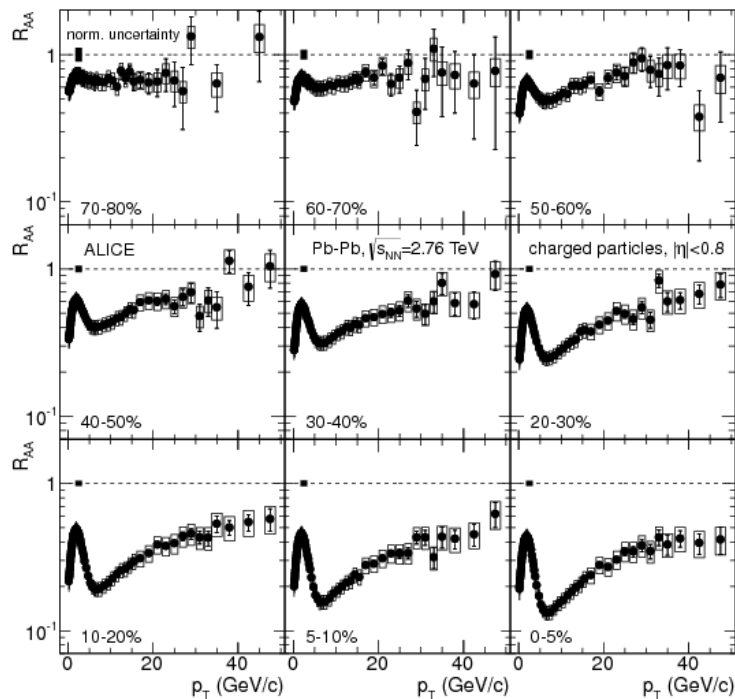


Figure 1.5: The charged particle R_{AA} as measured by the ALICE experiment at $\sqrt{s} = 2.76$ TeV for different centrality bins. Central collisions show a larger modification due to the QGP.

Source: [8]

construct jets with a jet finding algorithm, and use their total momentum as a base for the R_{AA} . Several examples of such analyses are [23, 41].

Alternatively it is also possible to compare central and peripheral heavy ion collisions

$$R_{CP}(p_T) = \left(\frac{1}{\langle N_{\text{bin}}^{\text{cent}} \rangle} \cdot \frac{dN_{\text{AA}}^{\text{cent}}}{dp_T} \right) \Bigg/ \left(\frac{1}{\langle N_{\text{bin}}^{\text{peri}} \rangle} \cdot \frac{dN_{\text{AA}}^{\text{peri}}}{dp_T} \right), \quad (1.8)$$

where the variables are identical, but now the distinction is made between central and peripheral events. In the peripheral events one would expect not a QGP with a lower density and a lower particle production, so it is to be expected that $R_{CP} < 1$. This is confirmed by measurements.[11]

As we have seen measurements of non-unity R_{AA} and R_{CP} are signifiers of the presence of jet quenching and have been measured to great precision, though they are subject to criticism. At high p_T the R_{AA} is mainly sensitive to the leading fragments in the jet, and therefore represents a measure for the energy loss of the particles. At low p_T the interpretation of the R_{AA} is more difficult. Because of conservation of energy and momentum, we in principle know that the energy of the jet cannot vanish in interaction with the medium. So the ‘missing’ energy at high p_T has to be present somewhere at lower energy and possibly at larger angles. It is very difficult to distinguish this ‘missing’ energy from the soft partons emitted during the cooling of the QGP, especially since it is not a given that the shape of the jet is similar at high and low energy. And if a significant part of the physics does take place at these low momenta, changes at this level do matter.[43]

Di-jet asymmetry

The path-length dependence of jet quenching can be tested by comparing different jets in heavy ion collisions that on average encounter a different amount of QGP. Momentum conservation ensures that with the creation of every jet a jet of equal momentum should travel the other way. The points of origin of these di-jet systems does not have to be in the exact centre of the collision. This means that one of the jets travels further through the QGP than the other. As shown in Figure 1.6 the top jet has a shorter travel path and experiences less quenching than the opposite facing jet. To compensate for processes that do not relate to the QGP, it is common to study both pp-collisions and heavy ion collisions for the di-jet imbalance

$$A_J = \frac{p_{T,1} - p_{T,2}}{p_{T,1} + p_{T,2}}, \quad (1.9)$$

with $p_{T,1}$ the momentum of the faster jet in the di-jet system, and $p_{T,2}$ the momentum of the slower one in the other hemisphere of the event. This is an often measured quantity. [74, 21, 47] Theoretical simulations can then be compared to these measurements to test the physical mechanisms implemented in these models.[66] Studies in p–Pb collisions show that these effects are not due to initial-state effects.[36] However due to energy loss fluctuations it is possible that the energy of the jet with a shorter path length, E_{T1} in Figure 1.6, is smaller than the energy of the jet with a longer

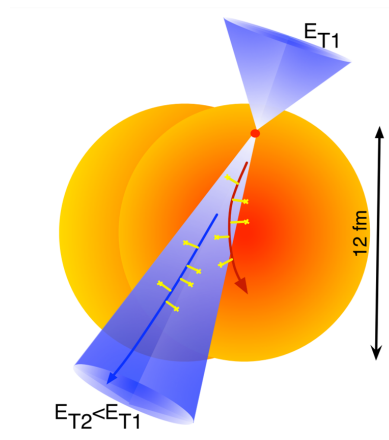


Figure 1.6: A schematic view of a di-jet system. It is not created in the centre of the collision, and therefore it is to be expected that usually jet 1 has a higher energy than jet 2 due to the path length difference.

Source: [32]

path length, E_{T2} in the figure. This makes the interpretation of di-jet asymmetry as a measure of path length dependence more difficult.

On the top row of Figure 1.7 there are distributions of the di-jet asymmetry amongst detected di-jet systems in the ATLAS experiment. The HIJING+PYTHIA model consists of simulated jets inserted into a simulated heavy ion background, without any model for quenching. That di-jets in this model have only relatively small differences from the di-jets in pp-collisions, shows that the differences between PbPb-collisions and pp-collisions are not merely due to the jet energy fluctuations introduced by the background in heavy-ion collisions. The shift of the distributions to higher asymmetries when considering more central events is evidence that this is largely due to the jet interacting with the QGP. In the 10% most central events the mode of di-jet systems have one jet which lost about half its energy. In pp-collisions and peripheral collisions this mode is around 0 to 10% of the energy. The bottom row shows the distribution of the angles between the two jets, which shows a clear peak at 180 degrees ($\Delta\phi = \pi$) and a small increase of near-side ($\Delta\phi = 0$) jet pairs in central PbPb collisions, but that for central events there is a small deviation from the distribution for pp-collisions.

Describing di-jet imbalance implicates that the jet on the away-side loses energy. The underlying hadron shower does still obey the law of conservation of energy. Instead it can be shown that the energy is emitted at lower energies and larger angles.[54]

While it is natural to interpret the increased imbalance in PbPb collisions as being due path-length differences, fluctuations of the energy loss also play a role. A recent study has shown that even if all di-jets are produced in the center of the collisions zone, fluctuations of energy loss lead to an asymmetry that is of similar size as the

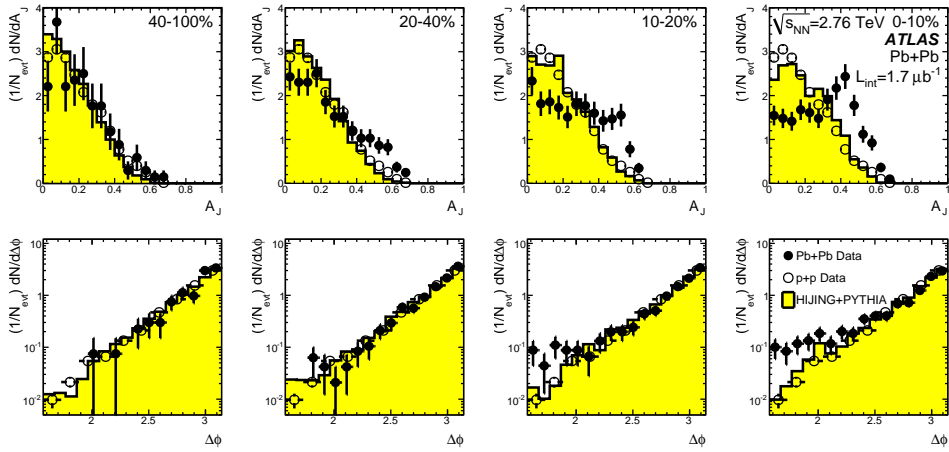


Figure 1.7: Top row: The distribution of di-jet asymmetry amongst the detected di-jet systems as measured by the ATLAS experiment at $\sqrt{s} = 2.76$ TeV for peripheral (left) to central (right) events. Jets have been reconstructed using the anti- k_T algorithm with jet radius $R = 0.4$. Bottom row: The distribution of the azimuthal angle ($\Delta\phi$) between the leading and subleading jet.

Source: [21]

effect that is measured at the LHC.[58] For instance the mass of the parton originating the jet could also heavily influence the energy loss. This would also mean that the assumption that the leading jet in the di-jet system is not necessarily associated with the parton that traveled the shorter distance through the plasma. It seems theoretical consensus on this subject has not yet been reached, so additional probes could help in this respect.

Jet fragmentation function

Another tool to study the effect of the QGP on a jet, is an energetic distribution profile of the jet called the fragmentation function. It is the distribution of the parameter $z = \frac{\mathbf{p}_{\text{hadron}} \cdot \mathbf{p}_{\text{parton}}}{p_{\text{parton}}^2} \approx \frac{p_{\text{T,hadron}} \cos(\Delta r)}{p_{\text{T,parton}}}$ for all the hadrons in a jet, with the experimental approximation using $\Delta r = \sqrt{\Delta\phi^2 + \Delta\eta^2}$, the distance in (η, ϕ) -space between the initial parton direction and the hadron direction. The momentum of the initial parton is often approximated by the momentum of a (background-subtracted) jet, which is accurate for pp-collisions.⁵ The fragmentation function in PbPb-collisions can then be divided through the one in pp-collisions to study which momentum fraction domains are affected in the quenching.

ATLAS results for the ratio of the fragmentation functions can be found in Figure 1.8

⁵This approximation is not perfect in PbPb-collisions, especially not for smaller jet radii, and can be a source of bias.

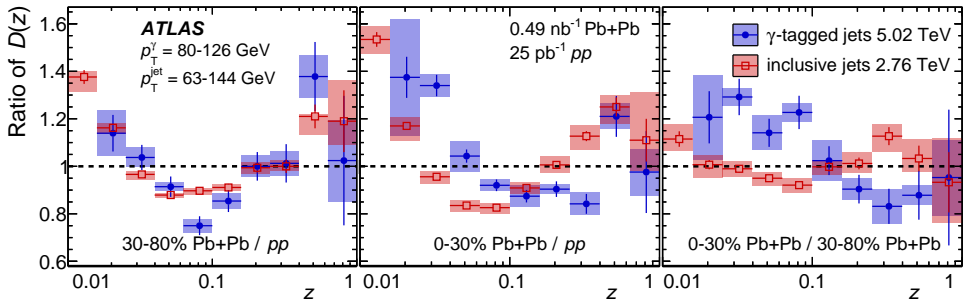


Figure 1.8: The ratio of the fragmentation function for two centrality bins, 30-80% and 0-30%, and their respective fraction. The red points are for inclusive jets at $\sqrt{s} = 2.76$ TeV, and the blue points for photon-tagged jets at $\sqrt{s} = 5.02$ TeV. The inclusive jets have a different centrality selection: 30-40% (instead of 80) and 0-10% (instead of 30). Jets were reconstructed with anti- k_T algorithm and $R = 0.4$

Source: [2], where [3] is cited for the inclusive jet data.

in the red points. In both the central and mid-central events a depletion is present in the middle momentum range of the jet, and a enhancement can be found at the low momentum fractions. This indicates that higher momentum particles in the jet are lose momentum by radiative and/or elastic processes, leading to an increase of yield in the low p_T -domain of the jet. Similar results have been obtained by the CMS experiment.[35, 1]

The fragmentation function gives a broader picture of how jets are affected by the medium, instead of the ‘one number’ a jet R_{AA} or di-jet asymmetry provides. However unquenched jets with energy E are more prevalent than quenched jets with a resulting energy of E . As a result, when using a jet selection with a certain energy threshold, jets with higher energies are usually ‘less’ quenched than the ‘average’ jet.

To counteract this bias, photon-tagged jets can be used. The transverse momentum of these photons is balanced by a jet with a high p_T , from a quark that is produced in the same hard scattering. Then the jet at nearly opposite ϕ of high enough p_T can be matched with the photon, leading to a photon-jet system where the energy on one side is known due to the photon not interacting with the QGP. Therefor the photon energy can be used as the p_{parton} , rather than the p_{jet} . As can be seen in the blue points in 1.8 such an analysis causes the increase at high z to vanish,⁶ suggesting that the fragmentation function ratio does not go above 1 for high z . More studies with photon-tagged jets have been performed.[71]

⁶The blue point is most likely an outlier in the pp-data used to normalize the result, since the central/peripheral fraction shows a more consistent picture.

1.5 Azimuthal dihadron correlations

In this work we use the correlations between two hadrons as function of their difference in azimuthal angle and pseudorapidity to study jets. Then jets with different angles with respect to the event plane are selected in order to study the path length dependence. We will discuss a method to subtract the combinatorial background when these jets are studied as a function of on their angle to the event plane.

After a short introduction into the topic, we will study a model for the flow background. This model will then be extended for the case that only a subset of the trigger particles is selected based on their orientation with respect to the event plane. In earlier work, the background distribution has been calculated assuming that the event plane orientations for all harmonic orders are identical. A new derivation without for the more general case where the symmetry plane orientations are not identical is presented. This is then discussed in the light of other equivalent work, and other experimental work in this field.

1.5.1 Dihadron correlations

Depending on the p_T -region studied, the background from soft production processes can be significant if not dominant with respect to particle production due to jets. However the momenta of the products of a hard scattering are significantly larger than those of the combinatorial background. In addition the splitting parton has a mass which is typically small compared to the jet energy, which ensures that the boost is more relevant to the resulting direction of the particle. Therefor the spray of particles in a jet is strongly correlated in one direction, in contrary to the background. It is possible to exploit this behaviour with the study of dihadron correlations in order to learn more about hadron production in jets.

To analyse particles that are likely produced in jets, we analyse pairs of hadrons: one with a momentum in a higher range, the trigger particle, and the other with a momentum in a lower range, the associated particle. The distribution of pairs as a function of their azimuthal and pseudorapidity separation angle shows a clear peak at the near side ($(\Delta\phi, \Delta\eta)$ near $(0, 0)$) that is produced by jet fragments coming from a single jet as well as a peak at $\Delta\phi \approx \pi$, containing particles from the away-side jet. The away-side peak is elongated in $\Delta\eta$. To obtain a per-trigger yield it is customary to normalise this by the number of triggers. The trigger/leading particle, with its momentum $p_{T,t}$, is selected to have momentum in a certain range, as is the case for the associated particle with momentum $p_{T,a}$ ($< p_{T,t}$).

The choice of these momentum ranges has a large impact on the resulting distribution. For high $p_{T,a}$ (and a higher $p_{T,t}$) a clear jet contribution becomes visible like in Figure 1.9a, since high p_T particles are most likely part of jets. This jet contribution takes the shape of a roughly 2D-Gaussian near-side peak, and a 1D-Gaussian in $\Delta\phi$ for the away-side. The away-side peak is smeared out in this way, because even though the peaks are produced back-to-back in the centre of mass frame of the collision between partons that produced them. And even though in the transverse plane, the centre-of-mass is at rest in the lab-frame, since the partons have a negligible

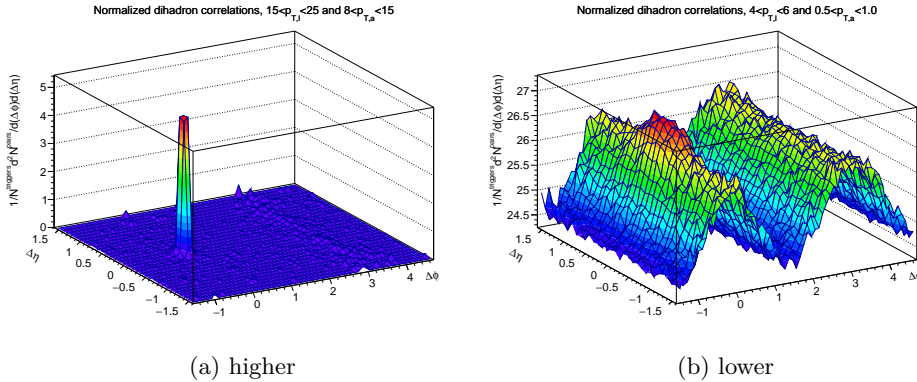


Figure 1.9: An example of dihadron distributions in semi-central PbPb–collisions for $12 < p_{T,t} < 25$ GeV/c and $4 < p_{T,a} < 6$ GeV/c (left), and $4 < p_{T,t} < 6$ GeV/c and $0.5 < p_{T,a} < 1$ GeV/c (right).

transverse momentum. However, this is not the case for the longitudinal direction. Here the parton-parton center of mass typically has a large boost, since the colliding partons of the two beams have different momenta. The boost in the z –direction necessary to translate between these two, smears out the peak to be flat in $\Delta\eta$ for reasonably small values of $\Delta\eta$. For low $p_{T,a}$, the distribution in addition has a significant flow background below the jet-like peaks. This background is uniform in $\Delta\eta$, and a sinusoid in $\Delta\phi$. This might effectively hide the away-side peak if the width of the away-side peak roughly coincides with the sinusoid. Figure 1.9b shows an example of this being the case. There are several processes that can contaminate this as a pure measurement of jet contributions. There are for instance resonances: strongly decaying particles that create short range (in $\Delta\eta, \Delta\phi$) correlations. These strong decays are impossible to separate with the help of a vertex restriction since they happen close to the initial vertex.

In this study the observable of interest is the jet yield Y for the near and the away-side: a measure of the average number of particles with a momentum of $p_{T,a}$ that are produced in one jet. In the high $p_{T,a}$ –limit, the background is negligible and the yields can be obtained by simply integrating the area around $(0, 0)$ for the near-side, and the area around $\Delta\phi = \pi$ for the away side. In other cases there are several ways to proceed with subtracting the flow-background from these histograms. In pp–collisions the distribution looks like Figure 1.9a.

In order to estimate the background, a region free of signal has to be identified. At high p_T , the signal peaks are narrow and a background-dominated range is clearly visible between the near and away-side peaks. At lower p_T , the peaks become broader and the background level is more difficult to measure. In this regime, some analyses resort to using the assumption that the associated yield is zero in the minimum of the distributions, the so-called ‘zero yield at minimum’ (ZYAM) method. This approach might also suffice in heavy ion collisions at high enough momenta. At lower p_T the

background becomes considerable, and a more involved approach has to be taken to separate the azimuthal modulation due to flow effects from the jet structure.

This work will be heavily involved with the question of subtracting background in the lower momentum region, so it will be discussed much more in depth. But for now two relatively simple approaches will form the basis for further discussion.

- The first approach uses the fact that the near-side peak vanishes at large $\Delta\eta$ to measure the background. The azimuthal distribution at large $\Delta\eta$ is scaled and subtracted from the histogram at all $\Delta\eta$. The resulting pair density is close to zero in most of the $\Delta\eta$ -space, with a clear signal peak around $(0, 0)$. This is a very simple and stable method as we will show later, but the disadvantage is that it is not possible to find a signal for the away-side peak, since it is uniform in $\Delta\eta$.
- The second approach is to fit the first contributions of a Fourier-series to the background outside the jet peak areas. In Section 1.5.2 we will continue on this idea.

1.5.2 Dihadron correlations as convolutions

In order to understand the contributions of flow, i.e. the collective azimuthal anisotropy observed in heavy-ion collisions, to the di-hadron distributions, we can build up expressions for the two-particle distributions from the single-particle azimuthal distribution. This can be used to formulate a model for the flow background in a dihadron histogram. As was discussed around Equation 1.3 the distribution for the background particles with respect to the symmetry planes can be expressed as follows with the flow coefficients:

$$\frac{dN}{d(\phi - \Psi_n^{\text{SP}})}(p_T) \propto 1 + \sum_{n=1}^{\infty} 2v_n \cos(n(\phi - \Psi_n^{\text{SP}})), \quad (1.10)$$

with v_n the n 'th flow coefficient and $\phi - \Psi_n^{\text{SP}}$ the angle between the particle and the symmetry planes.

When considering only the correlations induced by flow, we can calculate this as a convolution of the azimuthal angle difference between the distribution of the trigger particles and the distribution of the associated particles. All particle pairs with an opening angle $\Delta\phi$ and a leading and associate momentum of $p_{T,t}$ and $p_{T,a}$ will follow the following distribution

$$\frac{1}{\pi} \frac{dN_{\text{pairs}}}{d\Delta\phi}(\Delta\phi, p_{T,t}, p_{T,a}) \propto \int_{-\pi/2}^{3\pi/2} d\phi \frac{dN_{\text{trig}}}{d(\phi - \Psi_n^{\text{SP}})}(\phi, p_{T,t}) \cdot \frac{dN_{\text{asso}}}{d(\phi - \Psi_n^{\text{SP}})}(\phi + \Delta\phi, p_{T,a}), \quad (1.11)$$

where N_{trig} and N_{asso} are the single particle distributions for the trigger and associated particles respectively. We can explicitly perform the convolution with the expression

for the flow background from Equation 1.10. This results in a distribution that again can be expressed as a Fourier series like

$$B \left(1 + \sum_{n=1}^{\infty} 2p_n \cos(n\Delta\phi) \right), \quad (1.12)$$

where the dihadron flow parameters will be denoted with p_n from now on, and in this case they are given by

$$p_n(p_{T,t}, p_{T,a}) = v_n(p_{T,t})v_n(p_{T,a}). \quad (1.13)$$

This approach looks purely at the convolution of the (flow) background with the background. If we also have a jet signal with a finite number of particles per event, in principle the jets should be convoluted with the background as well to give a realistic model of the background in your dihadron spectrum. If the trigger hadrons have the same flow coefficient whether they are ‘part of a jet’ or ‘part of the background’, this still produces the composite flow coefficients from Equation 1.13. But if these ‘jet-hadrons’ exhibit a different correlation with respect to the symmetry plane then the ‘background-hadrons’, some deviations occur. This effect will be assumed to be negligible in this work, although this may be worth revising in light of the imperfect description of the measured background as we will discuss in the Section 7.3.3.

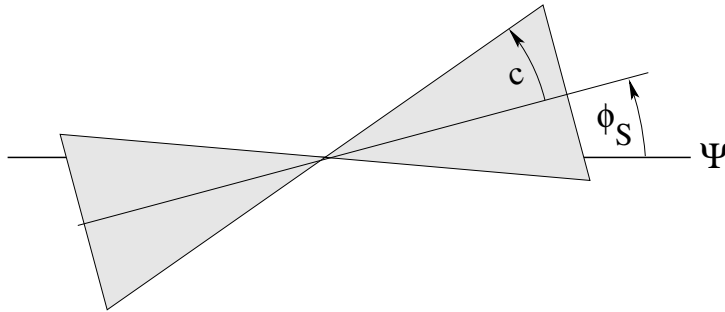
1.5.3 Event plane restriction

The path length dependence of energy loss could be studied by selecting pairs with specific orientations of the trigger particle with respect to the event plane. Trigger particles that are emitted in directions close to the reaction plane originate from jets that typically have a smaller path length than those that are emitted in directions perpendicular to the event plane. This will be discussed in more detail in Section 4.1.

To calculate the expected flow background in such measurements the integration range in Equation 1.11 can be restricted to only a certain section \mathcal{R} of the space with respect to the event plane. Let us consider an area $\mathcal{R}' = \{\phi \in \mathcal{C} \mid \phi \in \{\phi_S - c, \phi_S + c\}\}$, where \mathcal{C} is the circle with Ψ at $\phi_S = 0$ and $c \leq \frac{\pi}{2}$, and \mathcal{R} is its completion under point-symmetrization. This results in a bisector as in Figure 1.10. The convolution in Equation 1.11 becomes

$$\int_{\phi_S + \Delta\Psi - c}^{\phi_S + \Delta\Psi + c} d(\phi - \Psi_2^{\text{SP}}) \int_{-\pi}^{\pi} d(\Delta\Psi) \rho(\Delta\Psi) \frac{dN_{\text{trig}}}{d(\phi - \Psi_2^{\text{EP}})}(\phi - \Psi_2^{\text{SP}} + \Delta\Psi, p_{T,t}) \cdot \frac{dN_{\text{asso}}}{d(\phi - \Psi_2^{\text{EP}})}(\phi - \Psi_2^{\text{SP}} + \Delta\phi + \Delta\Psi, p_{T,a}), \quad (1.14)$$

where ρ is the distribution of the difference $\Delta\Psi \equiv \Psi_2^{\text{SP}} - \Psi_2^{\text{EP}}$ between the event plane and reaction plane angle, which is related to the experimental resolution of the event plane determination. Note that here it is assumed that the event plane orientation is identical for all harmonics $\Psi_n = \Psi_2^{\text{RP}}$. In Section 1.5.4 we will discuss what changes without this assumption.

Figure 1.10: The bi-sector \mathcal{R} .

Source: [27]

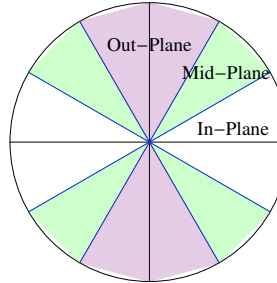


Figure 1.11: The definition of in-plane, mid-plane and out-of-plane.

In [27] it is shown that the composite flow coefficients then become

$$p_n^{\mathcal{R}} = v_n^a \cdot \frac{v_n^t + \delta_{n,\mathbb{E}} \cos(n\phi_S) \frac{\sin(nc)}{nc} R_n + \sum_{k \in \mathbb{E}} (v_{k+n}^t + v_{|k-n|}^t) \cos(k\phi_S) \frac{\sin(kc)}{kc} R_k}{1 + \sum_{k \in \mathbb{E}} 2v_k^t \cos(k\phi_S) \frac{\sin(kc)}{kc} R_k}, \quad (1.15)$$

where \mathbb{E} denotes the strict positive even numbers, $\delta_{n,\mathbb{E}}$ is 1 for $n \in \mathbb{E}$ and 0 otherwise, $R_n = \langle \cos(n\Delta\Psi) \rangle$ is the event plane resolution from Equation 1.6 and v_n^t, v_n^a are the n -th flow coefficients for the trigger and associated particles. The value of the flow coefficient v_n depends on p_T , and is therefore different for trigger particles v_n^t and associated particles v_n^a .

We will divide the space into three equal areas like indicated in Figure 1.11: in-plane, mid-plane and out-of-plane. Furthermore we assume that both the regular flow coefficients v_n and composite flow coefficients p_n for $n > 4$ are negligible. The p_n factors are identical in all disconnected bi-sectors due to symmetry arguments. This

means that we can perform the calculation once with the following parameters

$$\begin{aligned}
 \text{for in - plane :} \quad \phi_S &= 0, & c &= \frac{\pi}{6}, \\
 \text{for mid - plane :} \quad \phi_S &= \frac{\pi}{4}, & c &= \frac{\pi}{12}, \\
 \text{for out - of - plane :} \quad \phi_S &= \frac{\pi}{2}, & c &= \frac{\pi}{6}.
 \end{aligned}$$

Note that while c is smaller for the mid-plane region, the total angle range covered is the same for the three intervals because there are four disjunct mid-plane sectors and only 2 in- and out-of-plane (see Fig 1.11). Using these values in Equation 1.15 results in the following expressions for the composite flow:

$$\begin{aligned}
 p_{2,\text{in}} &= v_2^a \cdot \frac{v_2^t(1 + \frac{\alpha}{2}R_4) + \alpha R_2 + \alpha v_4^t R_2}{1 + 2\alpha v_2^t R_2 + \alpha v_4^t R_4}, \\
 p_{2,\text{mid}} &= v_2^a v_2^t \cdot \frac{1 - \alpha R_4}{1 - 2\alpha v_4^t R_4}, \text{ and} \\
 p_{2,\text{out}} &= v_2^a \cdot \frac{v_2^t(1 + \frac{\alpha}{2}R_4) - \alpha R_2 - \alpha v_4^t R_2}{1 - 2\alpha v_2^t R_2 + \alpha v_4^t R_4},
 \end{aligned} \tag{1.16}$$

for the second order,

$$\begin{aligned}
 p_{3,\text{in}} &= \frac{v_3^a v_3^t}{1 + 2\alpha v_2^t R_2 + \alpha v_4^t R_4}, \\
 p_{3,\text{mid}} &= \frac{v_3^a v_3^t}{1 - 2\alpha v_4^t R_4}, \text{ and} \\
 p_{3,\text{out}} &= \frac{v_3^a v_3^t}{1 - 2\alpha v_2^t R_2 + \alpha v_4^t R_4},
 \end{aligned} \tag{1.17}$$

for the third order under the assumption that the v_1 contribution is negligible, and

$$\begin{aligned}
 p_{4,\text{in}} &= v_4^a \cdot \frac{v_4^t(1 - \frac{\alpha}{4}R_8) + \frac{\alpha}{2}R_4 + \alpha v_2^t R_2}{1 + 2\alpha v_2^t R_2 + \alpha v_4^t R_4}, \\
 p_{4,\text{mid}} &= v_4^a \cdot \frac{v_4^t(1 + \frac{\alpha}{2}R_8) - \alpha R_4}{1 - 2\alpha v_4^t R_4}, \text{ and} \\
 p_{4,\text{out}} &= v_4^a \cdot \frac{v_4^t(1 - \frac{\alpha}{4}R_8) + \frac{\alpha}{2}R_4 - \alpha v_2^t R_2}{1 - 2\alpha v_2^t R_2 + \alpha v_4^t R_4},
 \end{aligned} \tag{1.18}$$

for the fourth order, where $\alpha = \frac{\sqrt{27}}{2\pi} \approx 0.83$ a recurring constant.

It is useful to note that the denominator is identical independent of the order of the composite flow coefficient. This is because it only reflects the changing background level due to the amount of triggers at a certain angle with the event plane. We also note that while the total amplitude due the p_3 does not depend on the orientation of the trigger particle with respect to the reaction plane, but the relative amplitude to the background does change. The $p_{2,\text{out}}$ coefficient can be negative depending on the choice of parameters.

In general, the relative amplitudes of the second and fourth harmonic (p_2 and p_4) are quite different in the trigger selected analysis compared to an analysis without trigger selection. In particular in the mid-plane bin, the p_2 can be small while it is still quadratic in v_2 , while p_4 has a term which is linear in v_4 .⁷

Restricting the plane will also influence the integral of the dihadron distribution. In [27] it is shown that the overall factor of Equation 1.12 in this restricted case becomes

$$B^{\mathcal{R}} = b' \cdot \frac{2c}{\pi} b \beta^{\mathcal{R}}, \quad (1.19)$$

where b is the total number of trigger particles in the analysed sample, b' is the analogous quantity for the associated particles, and

$$\beta^{\mathcal{R}} = 1 + \sum_{k \in \mathbb{B}} 2v_k^t \cos(k\phi_S) \frac{\sin(kc)}{kc} R_k. \quad (1.20)$$

In the following chapters we will always consider per trigger yield, which means that we divide by the factor $\frac{2c}{\pi} b \beta^{\mathcal{R}}$. In that case the overall multiplication factor therefore will be b' , independent of the angle to the event plane.

1.5.4 Background model with correlated event planes

In the results above, which are reproduced from [27], it is assumed that all Ψ_n are fully correlated, i.e. that $\Psi_2 = \Psi_3 = \Psi_4$ for every event. This assumption is not expected to be fulfilled in real events. From the $n = 2$ and $n = 3$ we know from both theoretical Glauber predictions [62] and experimental measurements [42] that they are very weakly correlated. We could instead more generally assume that the two distributions of the particles are

$$\frac{dN^{t/a}}{d(\phi - \Psi_2^{\text{SP}})} = B^{t/a} \left(1 + \sum_{n=1}^{\infty} 2v_n^{t/a} \cos(n(\phi - \Psi_n^{\text{SP}})) \right) \quad (1.21)$$

$$= B^{t/a} \left(\sum_{n=0}^{\infty} 2v_n^{t/a} \cos(n(\phi - \Psi_2^{\text{RP}}) - n\Delta\Psi_n) \right), \quad (1.22)$$

with t and a for the trigger and associate distribution respectively, Ψ_n the n 'th order symmetry plane, $v_0 \equiv \frac{1}{2}$ a shorthand for computation, and $\Delta\Psi_n \equiv \Psi_n^{\text{SP}} - \Psi_2^{\text{RP}}$. This last rewrite expresses all angles with respect to Ψ_2^{RP} , which is convenient later when integrating specific orientations of the trigger particle with respect to the reaction plane. Note that it is assumed that the symmetry plane is independent of the p_T and therefore not dependent on whether it is the trigger or associate distribution.

The distribution of the symmetry plane angle differences $\Delta\Psi_n$ is denoted $\rho_n(\Delta\Psi_n)$. ρ_n is normalised and symmetric in two respects. The entire distribution is symmetric in the plane $\Delta\Psi_n = 0$, and it is rotational/translational symmetric over $\Delta\Psi_n \pm m \cdot \pi$.⁸

⁷Neglecting the shared denominator, but that is identical in both.

⁸These symmetries are inherited from the second order event plane.

If the average over a function f , noted as $\langle f(\Delta\Psi_1, \Delta\Psi_2, \dots) \rangle$, is defined as

$$\prod_{k=1}^{\infty} \left(\int_{-\pi}^{\pi} d(\Delta\Psi_k) \rho_k(\Delta\Psi_k) \right) f(\Delta\Psi_1, \Delta\Psi_2, \dots). \quad (1.23)$$

There is an implicit assumption here that the distributions of $\Delta\Psi_n$ are independent here.⁹ This means that

$$\begin{aligned} \langle \cos(m\Delta\Psi_m - n\Delta\Psi_n) \rangle &= \delta_{nm} \\ &+ (1 - \delta_{nm}) \langle \cos(n\Delta\Psi_n) \rangle \langle \cos(m\Delta\Psi_m) \rangle \end{aligned} \quad (1.24)$$

and

$$\begin{aligned} \langle \cos(m\Delta\Psi_m + n\Delta\Psi_n) \rangle &= \delta_{nm} \langle \cos(2n\Delta\Psi_n) \rangle \\ &+ (1 - \delta_{nm}) \langle \cos(n\Delta\Psi_n) \rangle \langle \cos(m\Delta\Psi_m) \rangle. \end{aligned} \quad (1.25)$$

After performing the convolution, where we neglect the difference between the Ψ_2^{SP} and Ψ_2^{EP} and the symmetrization of region \mathcal{R}' for the time being,

$$\left\langle \int^{\mathcal{R}'} d(\phi - \Psi_2^{\text{SP}}) \frac{dN^t}{d(\phi - \Psi_2^{\text{SP}})} (\phi - \Psi_2^{\text{SP}}) \cdot \frac{dN^a}{d(\phi - \Psi_2^{\text{SP}})} (\phi - \Psi_2^{\text{SP}} + \Delta\phi) \right\rangle, \quad (1.26)$$

it follows that the composite distribution $\tilde{N}^{\mathcal{R}}$ is

$$\tilde{N}^{\mathcal{R}'}(\Delta\phi) = \sum_{n \geq 0} 2B^t B^a v_n^t \left(v_n^a \cdot \text{diag} + \sum_{m \neq n} v_m^a \cdot S_{n,n} S_{m,m} \cdot \text{off-diag} \right), \quad (1.27)$$

where the diagonal elements are

$$\text{diag} = 2c \cos(n\Delta\phi) + S_{2n,n} \frac{\sin(2nc)}{n} \cos(n(\Delta\phi - 2\phi_S)) \quad (1.28)$$

and the off-diagonal elements are

$$\begin{aligned} \text{off-diag} &= +2 \frac{\sin((m+n)c)}{m+n} \cos((m+n)\phi_S + m\Delta\phi) \\ &+ 2 \frac{\sin((m-n)c)}{m-n} \cos((m-n)\phi_S + m\Delta\phi) \end{aligned} \quad (1.29)$$

with

$$S_{m,n} = \langle \cos(m\Delta\Psi_n) \rangle, \quad (1.30)$$

⁹Note that here it is assumed that the distributions of $\Delta\Psi_n$ are independent, i.e. that $\rho(\Delta\Psi_1, \Delta\Psi_2, \dots) = \rho(\Delta\Psi_1) \cdot \rho(\Delta\Psi_2) \cdot \dots$. For the purpose of this work it is assumed that the correlation between two Ψ_n and Ψ_m with $m \neq n$ and both unequal to 2, the correlation between them is negligible with respect to the correlation between Ψ_2 and either of them. The computations can be repeated with relative ease for the more general case, the major disadvantage is that a lot more unique parameters will enter the model.

where $\langle \dots \rangle$ is the average as defined in Equation 1.23, and $\frac{\sin(ax)}{x} \equiv a$ for $x = 0$.¹⁰ Note that this definition of S is similar to the R defined for the event plane, and $S_{2,2} = 1$ by construction. Due to the symmetries in the $\rho_n(\Delta\Psi_n)$ distribution introduced by the fact that Ψ_2^{SP} is symmetric over half a rotation, we can find that for odd n it follows that $S_{n,n} = 0$.

These results are not necessarily symmetric in $\Delta\phi = 0$, when the integration interval is not symmetric with respect to the event plane (if $\phi_S \neq 0$ or π). However if we symmetrize the integration interval by studying $\int^{\mathcal{R}}$ over the bi-sector instead of $\int^{\mathcal{R}'}$ over the sector, the results simplify to

$$\text{diag}_{\text{sym}} = \left[4c + 2S_{2n,n} \frac{\sin(2nc)}{n} \cos(2n\phi_S) \right] \cos(n\Delta\phi) \quad (1.31)$$

and

$$\begin{aligned} \text{off-diag}_{\text{sym}} = & +4 \frac{\sin((m+n)c)}{m+n} \cos((m+n)\phi_S) \cos(m\Delta\phi) \\ & + 4 \frac{\sin((m-n)c)}{m-n} \cos((m-n)\phi_S) \cos(m\Delta\phi). \end{aligned} \quad (1.32)$$

In order to normalise the v_n coefficients properly, the constant terms with $\cos(0\Delta\phi)$ should be gathered. This results in

$$2B^t B^a \left(4c + \sum_{k>0} 8v_k S_{k,k} \cos(k\phi_S) \frac{\sin(kc)}{k} \right). \quad (1.33)$$

When gathering all the terms of the form $\cos(n\Delta\phi)$, all results should be divided by this value to retrieve the p_n , resulting in

$$\begin{aligned} p_n = & \frac{v_n^a}{1 + \sum_{k>0} 2v_k^t S_k \frac{\sin(kc)}{kc} \cos(k\phi_S)} \\ & \left\{ v_n^t \left(1 + S_{2n,n} \frac{\sin(2nc)}{2nc} \cos(2n\phi_S) \right) \right. \\ & + S_{n,n} \sum_{m \neq n, m \geq 0} S_{m,m} v_m^t \left[\frac{\sin((n+m)c)}{(n+m)c} \cos((n+m)\phi_S) \right. \\ & \left. \left. + \frac{\sin((n-m)c)}{(n-m)c} \cos((n-m)\phi_S) \right] \right\}, \end{aligned} \quad (1.34)$$

where S_n is 0 for odd n .

The next step is to introduce the event plane resolution that is caused by the difference $\Delta\Psi$ between the event plane and the reaction plane. Note that the difference between

¹⁰The entire proof works when adding ϵ to n taking $\lim_{\epsilon \rightarrow 0}$ for every step. This has been omitted for the sake of the reader.

higher order measured and true symmetry planes is irrelevant, since the higher order event planes are never used in the computation. It is however assumed that $\Delta\Psi$ and all $\Delta\Psi_n$ are uncorrelated, in other words: the accuracy of the measurement of the reaction plane is independent of the difference between Ψ_2 and other Ψ_n .

Note that in case all Ψ_n are aligned, this may not exactly hold, since all maxima in the angular distribution overlap which might make it easier to determine any Ψ_n . However, as discussed before, the Ψ_n are not expected to align exactly, and moreover the v_n decrease with n , so we expect that this approximation is good enough.

The average from Equation 1.23 from now on is redefined to include an integration over $\Delta\Psi$ and an extra factor $\rho(\Delta\Psi)$. Performing the calculations in almost identical fashion¹¹ results in

$$p_n = \frac{v_n^a}{1 + \sum_{k>0} 2v_k^t S_k R_k \frac{\sin(kc)}{kc} \cos(k\phi_S)} \left\{ v_n^t \left(1 + R_{2n} S_{2n,n} \frac{\sin(2nc)}{2nc} \cos(2n\phi_S) \right) + S_{n,n} \sum_{m \neq n, m \geq 0} S_{m,m} v_m^t \left[R_{n+m} \frac{\sin((n+m)c)}{(n+m)c} \cos((n+m)\phi_S) + R_{n-m} \frac{\sin((n-m)c)}{(n-m)c} \cos((n-m)\phi_S) \right] \right\}, \quad (1.35)$$

with $R_n = \langle \cos(n\Delta\Psi) \rangle$ the event plane resolution as defined in Equation 1.6. It is important to note that these results satisfy the following conditions:

- In the case that $\Psi_n^{\text{SP}} = \Psi_2^{\text{RP}}$, then $\rho(\Delta\Psi_n) = \frac{1}{2}(\delta(\Delta\Psi_n) + \delta(\Delta\Psi_n - \pi))$, and all $\langle \cos(n\Delta\Psi_n) \rangle$ are equal to $\delta_{n,\mathbb{E}}$, it simplifies to Equation 1.15.
- In the case that all event planes are fully uncorrelated, all $\langle \cos(n\Delta\Psi_n) \rangle$ for the case $n \geq 3$ are equal to 0 and the composite flow parameters in the higher orders simplify to

$$p_n = \frac{v_n^t \cdot v_n^a}{1 + 2 \cdot X \cdot v_2^t \cos(2\varphi_S) \frac{\sin(2c)}{2c} R_2}, \quad (1.36)$$

for $n \geq 3$, where X is +1 for the in-plane result, 0 for mid-plane and -1 for the out-of-plane. For $n = 2$ the result has an additional term due to the fact that $S_{2,2} = 1$ by construction. There it becomes

$$p_2 = \frac{v_n^t \cdot v_n^a \left(1 + R_4 \frac{\sin(4c)}{4c} \cos(4\varphi_S) \right)}{1 + 2 \cdot X \cdot v_2^t \cos(2\varphi_S) \frac{\sin(2c)}{2c} R_2}. \quad (1.37)$$

¹¹One can use the substitution $\phi_S \rightarrow \phi_S + \Delta\Psi$ to save on calculations.

Restricting this to the division of the angular space as defined in Figure 1.11, this results in:

$$p_{2,\text{in}} = \frac{v_2^a}{\beta^{\text{in}}} \left\{ v_2^t \left(1 + \frac{\alpha}{2} R_4 \right) + \alpha R_2 + R_2 S_{4,4} \alpha v_4^t \right\}, \quad (1.38)$$

$$p_{2,\text{mid}} = \frac{v_2^a v_2^t}{\beta^{\text{mid}}} (1 - \alpha R_4), \quad (1.39)$$

$$p_{2,\text{out}} = \frac{v_2^a}{\beta^{\text{out}}} \left\{ v_2^t \left(1 + \frac{\alpha}{2} R_4 \right) - \alpha R_2 - R_2 S_{4,4} \alpha v_4^t \right\}, \quad (1.40)$$

$$p_{3,\text{in}} = \frac{v_3^a v_3^t}{\beta^{\text{in}}}, \quad (1.41)$$

$$p_{3,\text{mid}} = \frac{v_3^a v_3^t}{\beta^{\text{mid}}}, \quad (1.42)$$

$$p_{3,\text{out}} = \frac{v_3^a v_3^t}{\beta^{\text{out}}}, \quad (1.43)$$

$$p_{4,\text{in}} = \frac{v_4^a}{\beta^{\text{in}}} \left\{ v_4^t \left(1 - \frac{\alpha}{4} R_8 S_{8,4} \right) + \frac{\alpha}{2} R_4 S_{4,4} + \alpha R_2 S_{4,4} v_2^t \right\}, \quad (1.44)$$

$$p_{4,\text{mid}} = \frac{v_4^a}{\beta^{\text{mid}}} \left\{ v_4^t \left(1 + \frac{\alpha}{2} R_8 S_{8,4} \right) - \alpha R_4 S_{4,4} \right\}, \quad (1.45)$$

$$p_{4,\text{out}} = \frac{v_4^a}{\beta^{\text{out}}} \left\{ v_4^t \left(1 - \frac{\alpha}{4} R_8 S_{8,4} \right) + \frac{\alpha}{2} R_4 S_{4,4} - \alpha R_2 S_{4,4} v_2^t \right\}, \quad (1.46)$$

with

$$\beta^{\text{in}} = 1 + 2\alpha v_2^t R_2 + \alpha v_4^t R_4 S_{4,4}, \quad (1.47)$$

$$\beta^{\text{mid}} = 1 - 2\alpha v_2^t R_2, \text{ and} \quad (1.48)$$

$$\beta^{\text{out}} = 1 - 2\alpha v_2^t R_2 + \alpha v_4^t R_4 S_{4,4}. \quad (1.49)$$

From now on we will define

$$p_{3,\text{red}} = v_3^a v_3^a \text{ and} \quad (1.50)$$

$$p_{4,\text{red}} = v_4^a v_4^a \quad (1.51)$$

as the reduced composite flow. It is useful to note that the equations above are only dependent on $p_{3,\text{red}}$, and not on the individual flow coefficients. The same is true for $p_{4,\text{red}}$ if and only if $S_{4,4} = 0$, i.e. when Ψ_2 and Ψ_4 are uncorrelated.

Towards the end of the work in this section we were made aware of the similar work in [63]. Both this work and that paper expand on the pre-existing literature by dropping the assumption that all orders of the symmetry planes are fully correlated. The assumptions taken in [63] are largely identical, but the vernacular used there and here are unfortunately partially different. In Appendix C the main differences between these two models will be discussed for completeness and ease of interpretation of the results.

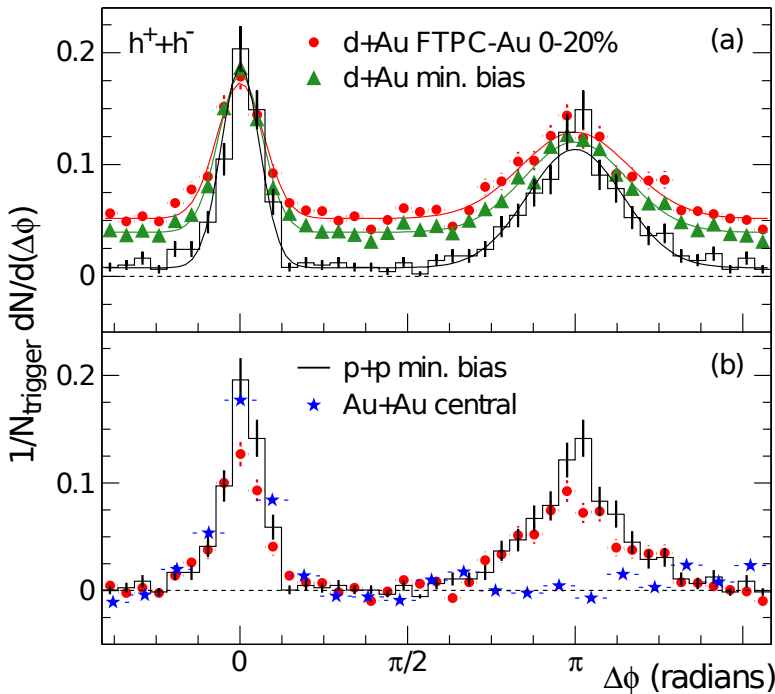


Figure 1.12: Azimuthal correlation distribution between hadrons as measured by the STAR collaboration.

Source: [12]

1.5.5 Measurements in dihadron correlations

To quantify the modification of the associated yield, we define the following the associated yield ratio I_{AA} and the central–peripheral associated yield ratio I_{CP} as

$$I_{\text{AA}} = \frac{Y_{\text{AA}}}{Y_{\text{pp}}} \quad \text{and} \quad I_{\text{CP}} = \frac{Y_{\text{central}}}{Y_{\text{peripheral}}}. \quad (1.52)$$

Both fractions can be computed for the near-side peak yield and for the away-side peak. Note that since the associated yields in I_{AA} are normalised per trigger particles, the effect of the number of binary collisions and the leading particle suppression are divided out in the I_{AA} ratio. This has the advantage that the $I_{\text{AA}}/I_{\text{CP}}$ has no need for input from a Glauber model to correct for the number of participants in the collision.

The first jet measurements at RHIC were based on the di-hadron correlation method to determine the associated yields. Fig 1.12 shows the result of such measurements in the STAR experiment. A striking suppression of the away side yield is seen in AuAu but not in dAu. Similar results were found in [14]. This is a good indication that the deviations from I_{AA} from unity are due to interactions with the QGP, and not

due to cold nuclear matter effects.

Comparing the I_{AA} for the near-side peak and for the away-side peak is a slightly different way to study di-jet asymmetry as discussed in Section 1.4.3. Though it is good to keep in mind that this still possesses a comparable selection bias.

Chapter 2

Toy Monte Carlo simulations

In order to test the stability of the fit and discover any indications of systematic uncertainties behind the background model discussed in Section 1.5.4, a toy Monte Carlo model (tMCm) was made and fitted with the theoretical model. Then the results of the fit could be confronted with the input parameters of the tMCm, to check for a bias in both the value of and the error on the resulting parameters. Several of the conclusions from this procedure can be used to validate the approach chosen on the data.

2.1 Setup

The tMCm was build specifically to check the validity of the results of equations 1.38 through 1.49. Monte Carlo events were generated with the following ingredients:

- Only flow is included in the model, no jet signals.
- The ‘background’ is based on the dihadron measurement of a set of trigger and an associated particles, with both their own distinct flow parameters. It should be sorted in three different bins depending on the orientation of the trigger to the participant plane.
- A participant plane measurement is simulated, dependent on a particular amount of correlation between the event planes $\Psi_{2,3,4}$.
- One-dimensional distributions in azimuthal angle differences $\Delta\phi$ are used.
- Based on the participant plane measurement, and an assumption about the correlation between event planes, the R and S parameters can be calculated.

Afterwards the generated $\Delta\phi$ distribution is fitted with the equations mentioned before. The results of this fit are then confronted with the input values. There is also the possibility to repeatedly generate MC-data, and perform a bootstrap error

calculation in this way to determine the statistical uncertainty on the parameters and compare these to the uncertainties estimated from the numbers of pairs.

2.1.1 Implementation

The tMCM adheres to the following procedure to generate an azimuthal angle difference distribution that simulates the background of one event:

- $\Psi_2 = 0$ is taken as the event plane orientation, which is possible due to the rotation symmetry of the problem. Then Ψ_3 and Ψ_4 are drawn from the distribution

$$\text{Gauss} \left[0, \frac{1}{C_i} - 1 \right] \mod \pi, i \in \{3, 4\} \quad (2.1)$$

where C_3 and $C_4 \in (0, 1)$ are parameters that control the correlation between Ψ_2 and Ψ_3, Ψ_4 . The special cases where the planes are uncorrelated ($C_4 \rightarrow 0$) and completely correlated ($C_4 \rightarrow 1$) are implemented as resulting in $U_{[0, 2\pi)}$ (the uniform distribution) and $\delta(0)$ respectively.

- Based on these symmetry plane angles, 3 sets of $\Delta\phi$ distributions are simulated:
 - T particles are generated with the distribution $1 + 2v_2^t \cos(2\phi) + 2v_3^t \cos(3(\phi - \Psi_3)) + 2v_4^t \cos(4(\phi - \Psi_4))$ to be used as the trigger particles.
 - A particles are generated with the distribution $1 + 2v_2^a \cos(2\phi) + 2v_3^a \cos(3(\phi - \Psi_3)) + 2v_4^a \cos(4(\phi - \Psi_4))$ to be used as the associated particles.
 - For the particles used in the event plane detection V particles with the distribution $1 + 2v_2^v \cos(2\phi) + 2v_3^v \cos(3(\phi - \Psi_3)) + 2v_4^v \cos(4(\phi - \Psi_4))$ are generated. In an experimental setting these particles are measured in a separate detector at a different rapidity.
- The participant plane of the event plane detection distribution is computed by filling the angles of the V particles in a histogram with V_{bins} bins, and the Q_2 -vector is computed using Equation 1.4. The resulting event plane angles are referred to as Ψ_p .
- The $\Delta\phi$ histograms for the trigger particles are filled. This is filled into separate histograms for the three cases where the leading particle is in/mid/out-of-plane with respect to Ψ_p .

This is repeated N_{ev} times. On the collection of these events, the following steps are performed:

- All $\Delta\phi$ histograms are added together, and divided by the number of triggers that have that particular angle to the event plane.
- All Ψ_p are used to fill a histogram, and the Ψ_3 and Ψ_4 (which are equal to $\Delta\Psi_3$ and $\Delta\Psi_4$ due to the $\Psi_2 = 0$ convention) are added to the histogram as

well. From these the resolutions R and S are computed using Equation 1.6 and Equation 1.30.

- A simultaneous fit using the expressions of equations 1.38 through 1.49 of the azimuthal angle difference distributions for the three different trigger particle orientations with respect to the event plane is performed. The R and S values which were computed earlier are used as a given, and v_2^t, v_2^a, p_3 ($= v_3^t \cdot v_3^a$), v_4^t , v_4^a and a common background level B are fitted to the data.

The resulting flow variables and their errors can be compared with the input values.

Parameter choices

Some parameters are constant in this work. First of all Ψ_3 is assumed to be uncorrelated from Ψ_2 , so $C_3 = 0$. As was discussed at the end of Section 1.3.1, experimentally it was determined that this correlation is very weak. Furthermore it would be inconsistent to assume non-zero C_3 , but ignore all v_n contributions higher than $n = 4$, since introducing a correlation between Ψ_2 and Ψ_3 would necessarily introduce a 6-fold rotational symmetry. Therefor here this approximation was chosen.

For the purpose of this chapter, unless otherwise stated, ‘representative’ values for the flow coefficients have been chosen, with $v_2^t = 0.15$, $v_3^t = 0.08$, $v_4^t = 0.04$, $v_2^a = 0.2$, $v_3^a = 0.1$ and $v_4^a = 0.05$.

A detector like the ALICE V0 detector is simulated. This is the detector which will determine the event plane in the experimental setting. We will discuss this detector in detail in Section 3.2.3. by taking $V_{\text{bins}} = 8$. A slightly lower value for the flow coefficient $v_2^t = 0.09$ is used. v_3^t and v_4^t are varied in Section 2.2.1, but taken to be 0 further on. The amount of particles in the virtual V0, V was varied until it resulted in a R_2 factor of 0.8, which is the same value of the event plane resolution that is found in the experiment (see the end of Section 3.3.1 and in Figure 3.6). This resulted in the value $V = 251$.¹

2.2 Results

2.2.1 Event plane resolution/correlation factors

In this section the values of R_2 , R_4 , $S_{4,4}$ and $R_8S_{8,4}$ are determined depending on a set of assumptions for the correlation between the event planes. For the $R_8S_{8,4}$, only the product is relevant for the simultaneous background fit, and as such only the product was computed. The uncertainty on the R/S -values is mainly determined by the number of events generated, which was chosen to be 1000 in order to limit computation time. The uncertainty is estimated by repeating the process 100 times and calculate the standard deviation of the results. The values of these resolution/correlation factors can then be used in fit using the background model.

¹In order to avoid artifacts in the computed participant plane, it needs to be relative prime with respect to V_{bins} .

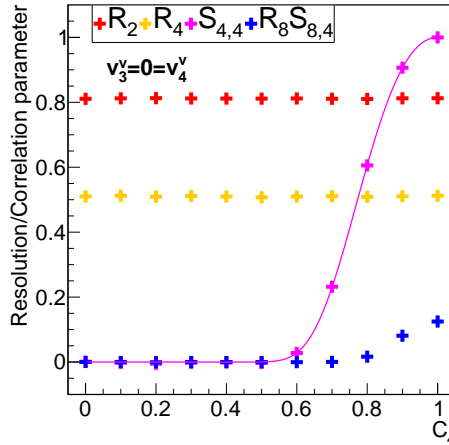


Figure 2.1: The value of the relevant event plane resolution and correlation parameters, depending on the amount of correlation between Ψ_2 and Ψ_4 , as determined by the tMCM by generating a thousand events. Errors determined via bootstrap, but smaller than markers. The model-parameters were tuned to result in a R_2 of about 0.8 at $C_4 = 1$. The line is a theoretical curve of $S_{4,4}$ as given by Equation 2.2. A test was performed with non-zero v_3^v and v_4^v , but the results were indistinguishable.

Figure 2.1 shows the result of this analysis. Note that $S_{4,4}$ varies from 0 to 1 in the extreme cases as expected. Note that the relation between C_4 and $S_{4,4}$ in principle could also be computed via

$$S(m, n) = \int_{-\infty}^{\infty} d\Delta\Psi_n \cos(m\Delta\Psi_n) \text{Gauss}\left[0, \frac{1}{C_n} - 1\right](\Delta\Psi_n) \\ = e^{-\frac{m^2}{2}(\frac{1}{C_n} - 1)^2}, \quad (2.2)$$

given the Gaussian assumption on the distribution of $\Delta\Psi_n$. Note that the behaviour of the S -parameters is not influenced by the value of $v_{3,4}$.

R_2 and R_4 are invariant under C_4 , which is to be expected since Equation 1.6 is not dependent on Ψ_4 . Due to orthogonality of the harmonics, the R_2 , R_4 and R_8 should not depend on v_3^v or v_4^v . A test confirmed that for these parameters the cases with $(v_3^v, v_4^v) = (0, 0)$ and $(v_3^v, v_4^v) = (0.1, 0.05)$ are indistinguishable.

The results further on are dependent on the values of the R - and S -factors, and not directly on v_3^v and v_4^v . Therefor they were fixed to 0 for the rest of this chapter.

2.2.2 Quality of the fit

In this section the dihadron correlation plots are studied. 10 thousands events have been generated, each with $T = 20$ triggers and $A = 100$ associated particles.

Param.	Input	Uncorrelated	Semi-Corr. (0.7)	Semi-Corr. (0.8)	Correlated
v_2^t	0.1500	0.1467 ± 0.0018	0.1480 ± 0.0017	0.1485 ± 0.0018	0.1495 ± 0.0018
v_2^a	0.0500	0.046 ± 0.004	0.053 ± 0.002	0.0505 ± 0.0009	0.0508 ± 0.0005
p_3	0.0080	0.00793 ± 0.00015	0.00829 ± 0.00015	0.00831 ± 0.00015	0.00799 ± 0.00015
v_4^t	0.0400	0.0400 ^a	0.032 ± 0.003	0.034 ± 0.003	0.037 ± 0.003
v_4^a	0.0500	0.046 ± 0.004	0.053 ± 0.002	0.0505 ± 0.0009	0.0508 ± 0.0005
χ^2		238	186	196	204

Table 2.1: A comparison of the fitted parameters with the input parameters.

^aThis value does not have an error, because in the uncorrelated case the equations are only dependent on the product p_4 . Therefor this value is fixed, and for v_4^a absorbs the entire error.

Figure 2.2 shows the azimuthal angle difference distributions generated by the toy Monte Carlo model for several values of the correlation parameter C_4 . The differences in the shape of the mid-plane dihadron correlations are quite significant for different C_4 . All plots show a green line, which based on the equations 1.38 through 1.49, with the model input parameters inserted.² The red line shows the model fit, which is based on the same model, but with fitted parameters instead. This red line of the fitted model is not always visible due to the overlap of the green line of the theoretical model, which indicates that the input parameters can be reproduced with good precision. In Table 2.1 the input parameters are confronted to the fitted parameters.

At first glance these results seem consistent. All fitted values are at most about 2σ removed from the input value. However upon closer study it turns out that 11 of the 19 parameters differ by more than a 1σ from the input value. The cumulative binomial distribution indicates that probability of this happening is about $1 - 2\%$.³ Furthermore the χ^2 values are larger than the number of degrees of freedom (180 bins minus the 5 or 6 parameters), yielding probabilities in the order of a couple percent for the semi-correlated cases to a per mille for the uncorrelated case. This warrants some closer inspection, which is performed in the next section.

2.2.3 The quality of the errors resulting of the fit

In order to study the precision of the determination of the errors resulting from the fit, the model was run 100 times to determine the standard deviation of the results and compare them to the estimated uncertainties. This way the root mean square (RMS) error of these iterations can be compared to the mean value of the error determined by the chi-square fit. On both estimations of the error, the error was computed as well. In total 100 iterations of 100 events have been run, with $T = 20$ and $A = 100$. A symmetry plane correlation parameter of $C_4 = 0.8$ has been chosen.

The black points in Figure 2.3 show an average of the uncertainty and its uncertainty.

²With exception from the overall background level B , which is taken from the fit.

³Assuming that all parameters are independent, which is not entirely true.

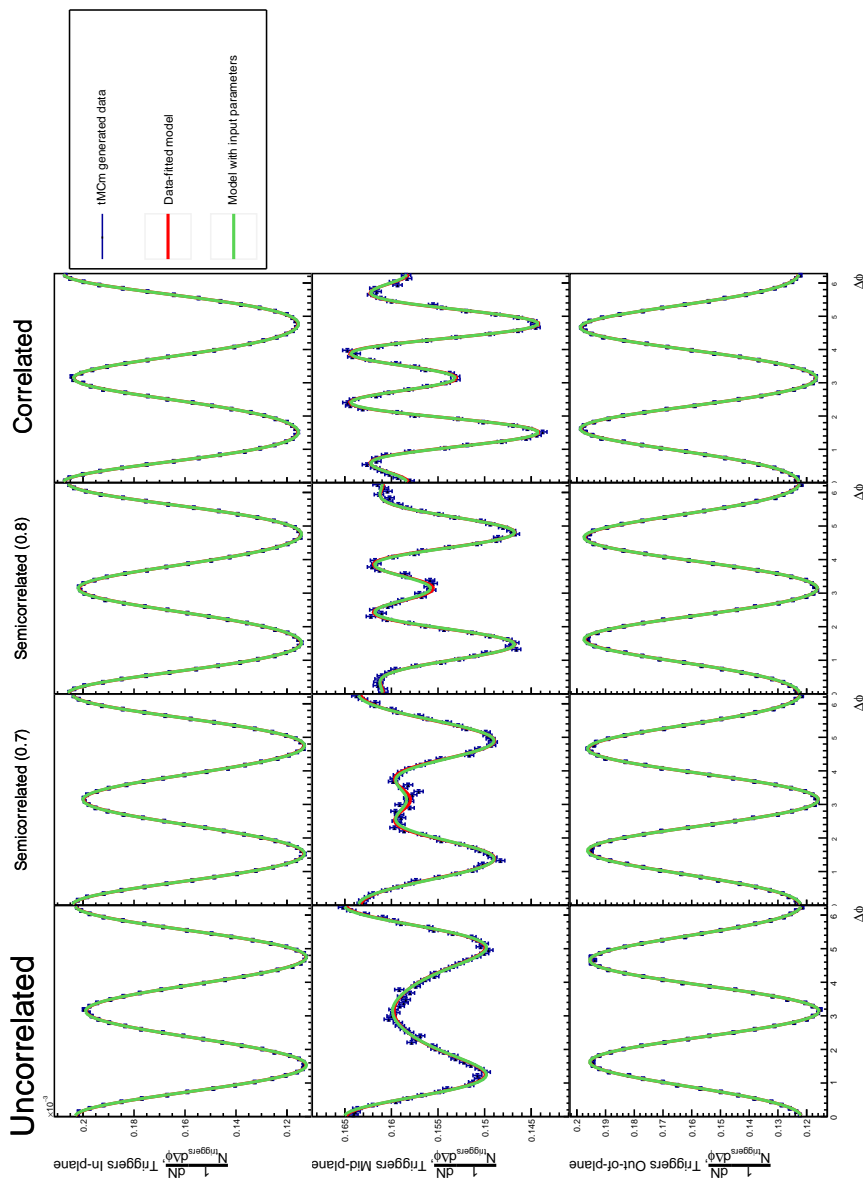


Figure 2.2: The dihadron distributions as a function of $\Delta\phi$ as generated with the toy MC model for several values of the correlation parameter C_4 . From top to bottom (in the frame of the plots): in-plane, mid-plane and out-of-plane. From left to right: $C_4 = 0$, $C_4 = 0.7$ $C_4 = 0.8$ and $C_4 = 1$.

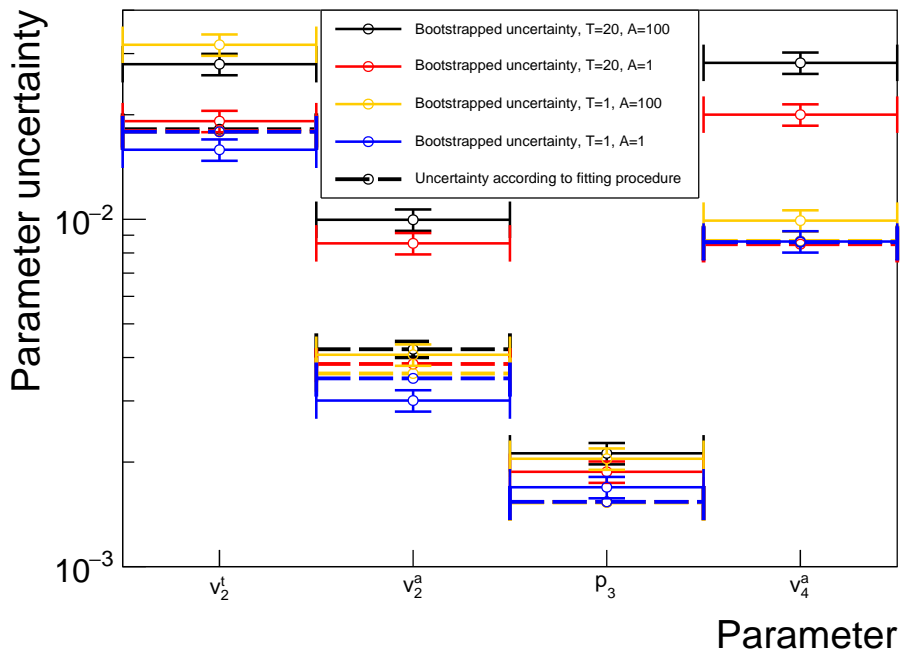


Figure 2.3: A comparison of the uncertainty on the fit parameters resulting from the fitting procedure with the uncertainties resulting from the bootstrap. The data points relating to the fit which seem to be missing, are hidden due to overlap.

These are not consistent with the uncertainties of the fit. This bias in the estimated uncertainties indicates the the generated pairs are not fully uncorrelated. This is probably due to the fact that the number of pairs is much larger than the number of generated particles. This also shows in the high χ^2 values. They either indicate the presence of correlations between the points, or that the statistical error on the $\Delta\phi$ distributions are underestimated. Several tests have been performed to check under which conditions this bias is present.

First the same procedure has been repeated with $T = 20$ and $A = 1$. To compensate for the decrease in the amount of statistics here, 100 iterations of 10,000 events have been run. The results of this calculation are shown by the red dashed line in Figure 2.3. Comparing the black and red dashed line shows that this indeed results in a difference between the fitting and bootstrap uncertainties does decrease. The explanation for this is that using multiple associated particles with each trigger particle leads to correlations between the points in a dihadron histogram. The angle of the trigger particles determines whether the pairs are added to the in- mid- or out-of-plane histogram. For each trigger particle $A = 100$ values are added to one histogram. So even though this trigger should count as only one unit of statistics with respect to determining the Poisson-like error of the relative level between the total contents of these three dihadron histograms, it counts as significantly more then that.

However, only taking $A = 1$, is not enough to find consistency between the uncertainties according to the fit and the variance of the repeated generation of toy MC data. Though it does result in consistent results for the v_2^t parameter, there are still significant differences in the associated particle flow parameters. Only when generating a single pair, i.e. $T = 1$, $A = 1$ per event, the pairs are fully uncorrelated and the two ways of estimating the uncertainties agree.

For the $T = 1$, $A = 100$ case the theoretical explanation provided above still holds: 1 simulation adds 100 pairs to one of the three plane bins. The errors on these pairs are correlated. For the $T = 20$, $A = 1$ case the reason is less intuitive but can argued on base of the symmetry of the situation.

It is noteworthy that taking $A = 1$ results in the correct error for v_2^t , where taking $T = 1$ results in correct error for v_2^a .

To judge whether any bias are present in the obtained fit parameters, Figure 2.4 shows the ratio between the reconstructed parameters and the tMCm input parameters. It is clear that with all values are consistent with the value 1. Furthermore there seems to be no systematic ordering in the different cases with multiple selected particles per event. This study shows no indications of a bias larger then 0.01 in v_2^a and 0.05 in p_3 and v_4^a in the fitted results at a correlation parameter $C_4 = 0.8$. Note also that the uncertainties are larger when multiple pairs are generated per event given the same total number of particles.

We can reverse this question: given a fixed number of events, would it be more effective to use just one trigger-associate pair and compute the error in the usual way, or does using everything and using a bootstrap method for the error calculation

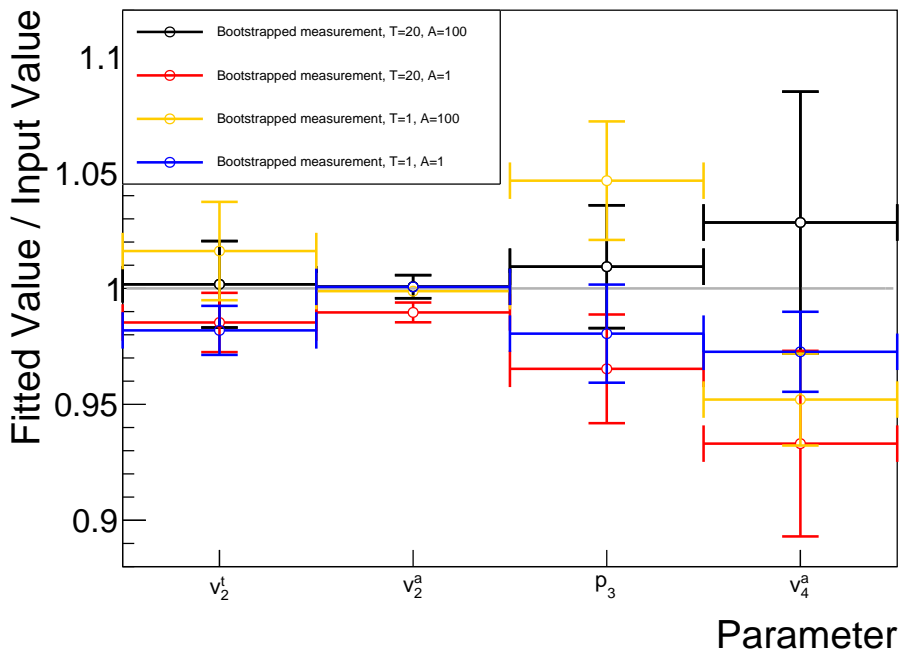


Figure 2.4: The relative deviation of the fitted parameters to the input parameters of the tMCm. The values are the average of the 100 runs of the tMCm, and the uncertainties are determined as their variance.

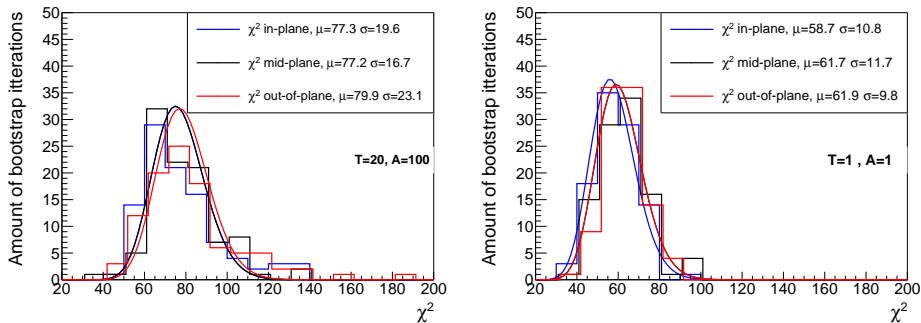


Figure 2.5: The distribution of χ^2 , with the contribution split into the three histograms that are fitted simultaneously. To the left the case with the correlated errors ($T = 20$, $A = 200$), and to the right the one without ($T = 1$, $A = 1$). The mid-plane and out-of-plane contributions have been displaced for the sake of readability. The smooth line shows the expected χ^2 -distribution given the μ per distribution. On the left side the black distribution is on top of the blue one. On the right side the red distribution is on top of the black one.

yield better results? Since in Figure 2.4 1 pair-per-event results are based on a factor 2000 more events than the default, this would have a factor $\sqrt{2000} \approx 45$ larger error. That would be clearly much larger then the bootstrap error on the 1 pair-per-event result. Therefor using the bootstrap method would be more accurate.

The last verification of the method looks at the distribution of the resulting χ^2 of the different dihadron histograms. Running the bootstrap yields a distribution for χ^2 of the resulting fits. It is also possible to compute the χ^2 contribution of the three underlying histograms with different trigger-event plane orientation. The χ^2 distributions in Figure 2.5 show that there are no significant differences between the three distributions in the right case where the errors are uncorrelated. In the left case where the errors are correlated, the out-of-plane distribution has a slightly longer high tail. However, in this case the spread of the results is significantly larger than the $\sqrt{2k}$ of the $\chi^2(k)$ -distribution. Therefor these upward outliers are also more likely to be a statistical fluctuation. At least for the $T, A = 1$ scenario on the right this mostly rules out the possibility that the model fits poorly in one plane, while compensating these deficiencies in another plane.

Translating these results for use in data, would suggest that it is prudent to select only one trigger and associated particle at random in each event. Alternatively it is possible to determine the errors on the values via a bootstrap procedure, though additional attention should be paid to internal friction in the fit between the different trigger-plane orientations. Performing the bootstrap would be the best use of the available data.

2.3 Conclusion

There are three conclusions that can be applied to the analysis of the data in the next chapter. First and foremost, the equations 1.38 through 1.49 are a successful parametrisation of the flow-background. The amount of correlation between the event planes changes the dihadron histograms significantly. However care should be taken with that the use of multiple triggers or associated particles per event causes correlation between the plots. These correlations do not cause a bias when determining the flow parameters, but they do lead to uncertainties on the results that are smaller according to the fitting procedure than they should be in reality. A bootstrap method is needed to obtain a reliable estimate of the statistical uncertainties for the size of the error.

The relevant code for reproducing the results in this chapter can be found at <https://github.com/DKeijdener/ToyMCbackgroundFitDihadron>.

Chapter 3

The experimental environment

This work is based on data gathered by the ALICE collaboration at the CERN accelerator complex near Geneva. This chapter presents information on the accelerators at CERN, the ALICE experiment and detector, the data reconstruction and the software involved in the process. Descriptions in this chapter are based on the state of the detector during run 1, in the period 2010–2013.

3.1 Large Hadron Collider

The Large Hadron Collider (LHC) is a circular particle accelerator and collider. With its circumference of 27 km it is the largest and most powerful accelerator in the world. It collides protons, ^{208}Pb -ions, or a combination of both. In collisions it can reach centre of mass energies of $\sqrt{s} = 13$ TeV in proton-proton collisions and $\sqrt{s} = 5.02$ TeV per nucleon pair in lead-lead collisions as of 2018.¹ The machine is inside a underground tunnel at a depth between 50 to 170 meters underground, partly in Switzerland, partly in France, near the city of Geneva.

Bunches of particles are prepared for injection into the LHC by a chain of accelerators. First comes a lineair accelerator that injects the bunches in the Proton Synchrotron (PS, 25 GeV for protons). Afterwards they are injected to the Super Proton Synchrotron (SPS, 450 GeV for protons), and finally into the LHC. Several bunches travel clockwise in one beam, while several other bunches travel the other direction in another beam. These beams are kept in the machine by superconducting dipole and quadrupole magnets. To get these magnets to a superconducting regime, the entire system has to be cooled to a temperature of 1.9 K by liquid helium. In order to prevent loss of the beam through collisions, within the beam pipes an ultra-high vacuum needs to be maintained, at a pressure around 10^{-9} Pa.

¹Proton-lead collisions will not be studied in this work.

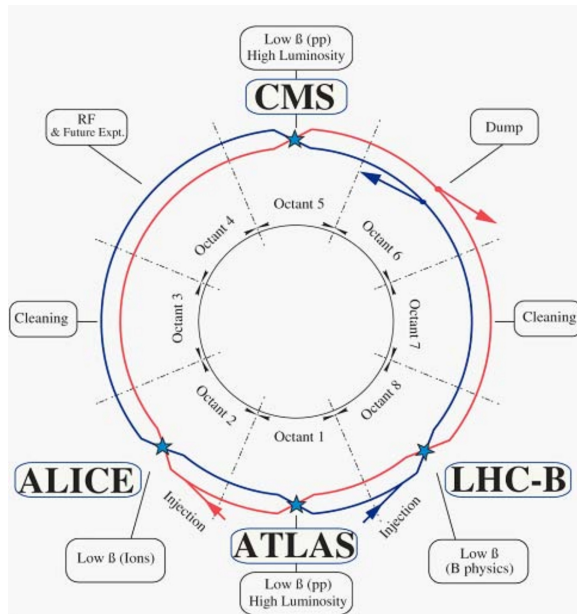


Figure 3.1: A schematic view of the LHC and the location of the experiments.

Source: [50]

After the filling of the LHC the beams are accelerated from 450 GeV to 7 TeV via the radio-frequency cavities. The electric field in these cavities switches with a frequency of 400 MHz, in order to give the bunches a boost in momentum. When at maximum energy, a set of specialised magnets focuses and brings the beams into collision at one of the four interaction points as shown in Figure 3.1. At one of these interaction points the ALICE experiment is situated. In optimal conditions, the stable beams with interactions can last for several hours. When the intensity of the beams becomes too low, they are dumped into a specially designed beam dump. Then the process of filling the LHC begins anew.

3.2 ALICE detector

The ALICE (A Large Ion Colliding Experiment) detector is a general purpose detector specifically designed to study interactions with a high multiplicity. It is therefore very valuable to study the QGP created in heavy-ion collisions. The entire detector is about 16 by 16 by 26 meters, and weighs 10^7 kg, though that weight is mainly in the signature red magnet encasing most of the detector. The experiment uses a right-handed Cartesian coordinate system with the z-axis along the direction of beam axis in the experiment, and the x-axis in direction of the centre of the LHC ring. This specifies the definition of pseudo-rapidity η and the azimuthal angle ϕ (see Section 1.2). The detector is mostly symmetric in the $z = 0$ plane, aside from the

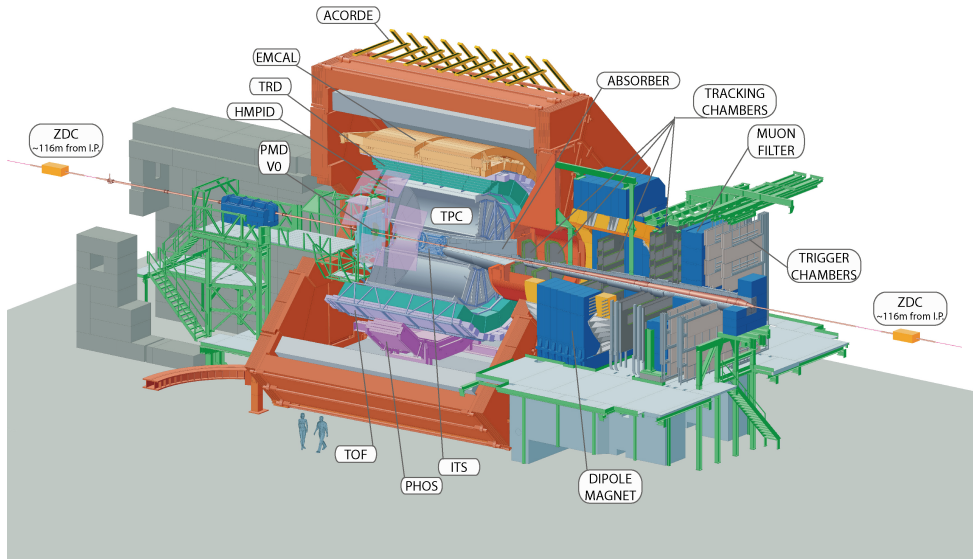


Figure 3.2: A schematic view of the ALICE detector.

Source: [50]

muon arms, and all of the detectors we will use in this study are rotation symmetric around the beam-axis.[5]

In Figure 3.2 a schematic view of the detector shows from the inside to the outside particles created in a collision will encounter the

- Inner Tracking System (ITS), a high-precision silicon detector which makes precision measurements of the position of origin of the particles and their momenta,
- the Time Projection Chamber (TPC), which can precisely measure the momentum of charged particles,
- a variety of different detectors with more specific usages which are not used in this work, such the ElectroMagnetic CALorimeter (EMCAL), which can measure neutral particles, the PHOton Spectrometer (PHOS), which is optimised for measuring photons, and the Time Of Flight detector (TOF), which is often used in determining particle types,
- the L3 solenoid magnet. This is the magnet that provides a magnetic field directed along the z -axis and dominates the physical appearance of the detector with its bright red color. The magnetic field enables us to determine the momentum of charged particles from the curvature of their tracks.

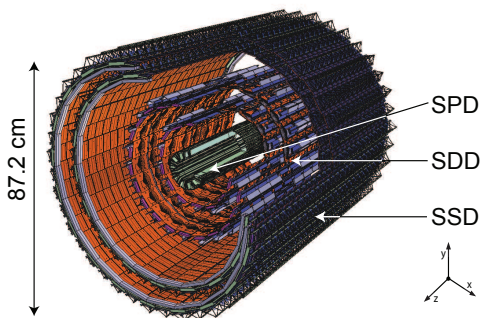


Figure 3.3: The ITS and its various components.

Source: [7]

Furthermore the V0 detector is located on both sides of the interaction point near the beam pipe. This detector can, amongst other things, help to determine the event plane of a collision. The dipole magnet near the detector is used to provide a magnetic field in the muon arms, and the rest of the detectors on that side are mainly used to detect muons.

For the purpose of this work, we will describe the ITS, the TPC and the V0 detector in more detail.

3.2.1 Inner Tracking System (ITS)

The Inner Tracking System (ITS) is an assembly of layers of silicon based detectors placed in concentric cylinders close around the beam pipe. Starting at the centre and working outwards there are two layers of the Silicon Pixel Detector (SPD), two layers of the Silicon Drift Detector (SDD), and two layers of the Silicon Strip Detector (SSD). These technologies are chosen so that the segmentation of each pair of layers is adapted to the local hit density, which decreases with increasing distance from the interaction point. The primary task of the ITS is to provide a high-resolution measurement of the pointing of tracks to the primary vertex, to enable the reconstruction of weak decays of heavy flavour mesons and baryons. It can reconstruct the primary vertex with a resolution of up to $40 \mu\text{m}$ (at higher multiplicity proton-proton events for the central vertex). It also has a low material budget as to not obstruct the view on the collision for the rest of the detector. For the mounting and cooling of the detectors it was also important to reduce the material budget as much as possible. This is why the entire structure is mounted on a carbon-fibre structure, and is cooled with water.

See Figure 3.3 for a schematic view of the detector. The outermost layer of the SSD, and the system as a whole, is 97.6 cm long and has a radius of 43.6 cm. All layers have a rapidity coverage of at least $|\eta| < 0.9$ and a full ϕ -coverage.

The SPD

The SPD consists of a grid of hybrid silicon pixels, 50 μm in the $r\phi$ -direction and 425 μm in the z -direction, and grouped in individual sensors. Each pixel is a reversed-biased diode: a diode with a voltage applied in the blocking direction. Charged particles passing through the detector generate charge that induces a small current in the diode. This results in a digital signal, which conveys information on the $r\phi$ and z -position of the particles. Two layers of this technology have been constructed at $r = 3.9$ cm and 7.6 cm from the centre of the beam pipe. The first layer of the SPD has an extended coverage ($|\eta| < 1.98$) with respect to the rest of the detector, so that also events with a slightly larger z position of the vertex can be detected properly. It can also be used in the low level triggering decisions of the detector: selecting events online depending on the number of hits in the SPD-layers. This uses the low latency of the technology to its advantage.[17] Combining the the information of several neighbouring cells decreases the resolution in the entire chip to 12 μm in $r\phi$ and 70 μm in z .

The SDD

At $r = 15.0$ and 23.9 cm the next two detection layers, the SDD, are located. The detection elements in this detector consist of neutron transmutation doped silicon: silicon that has been treated by a neutron beam in order to achieve a N-doping. The electrons that are produced by the high energy particles hitting the material flow to readout due to an electric drift field. From the time this takes one can determine the location of the impact in the flow direction. This comes with the benefit of additional resolution in that direction: on average 35 μm in $r\phi$ and 25 μm in z , the direction of the drift. Besides that it becomes possible to detect multiple particles within one cell, though these advantages come at the expense of speed.[40] Furthermore the readout is analogue, which means that energy loss measurements are possible. These measurements can be used to construct the momentum of low momentum particles.

The SSD

The outermost layers at $r = 38.0$ and 43.0 cm contain the SSD. These are silicon chips with p-doped strips on one side, and n-doped strips on the other side, both connected to the readout. When a particle crosses through the material, it will create electrons that will flow to the nearest n-strips, and holes that will flow to the nearest p-strips. The n and p-strips are not parallel, which enables the determination of the position up to 20 μm in $r\phi$ and 820 μm in z .[73, 6] Furthermore this system has analogue readout just like the SDD, and the deposited charge is dependent on the deposited energy of the passing particle.

Additional details on the ITS and its subsystems can be found in [6].

3.2.2 Time Projection Chamber (TPC)

The Time Projection Chamber (TPC) is a large gas drift detector that is the main all-purpose charged particle tracker of the ALICE experiment.

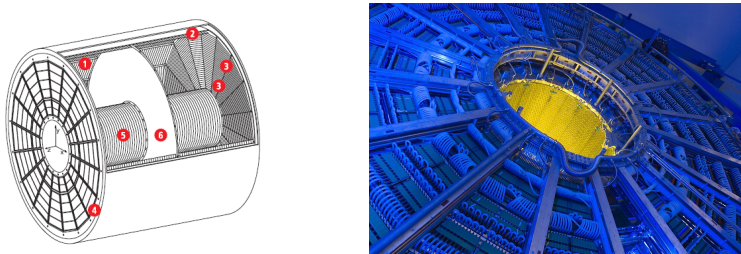


Figure 3.4: Left: A schematic of the TPC with (1) the outer field cage, (2) CO₂ gas envelope, (3) readout chambers, (4) endplate, (5) the inner field cage and (6) the central high voltage electrode. Right: A photograph of the end cap in blue, and the inner cylinder in yellow light.

Source: left [38], right [39]

As Figure 3.4 shows, the detector has the shape of a cylindrical shell, with an inner radius of about 85 cm and an outer radius of 250 cm.[6, 5] With a length of 5 meter in the z -direction it covers the eta range between ± 0.9 . It can span a larger η -range if a smaller track length is sufficient for the track quality needed in the study, but in this work we will limit ourselves to the full length tracks with $|\eta| < 0.9$. In the middle there is an electrode, which provides the drift field, and the read out is located in the endcaps with a $\Delta V = 100$ kV. The volume in between is filled with a mixture of neon (86%), carbon dioxide (9%), and nitrogen (5%).² When charged particles ionise the gas, the resulting electrons will follow the electric drift field along the z -direction and cause a current when hitting the end plates.

The drift velocity in the gas mixture depends strongly on the density of the mixture. To achieve a constant density, the gas has to be kept at a constant temperature, with deviations no larger than $\Delta T = 0.1$ K. This is achieved with several heat screens and cooling systems. A laser system provides straight tracks through the gas for calibration purposes.

The readout is done with wire chambers, and split into 18 sectors on each side, with dead spots in between which result in lower efficiencies at fixed ϕ . A gating grid shields the readout chamber from the gas volume to prevent distortions due to build up space charge from electrons that drift back into the gas from the multiplication area. It is triggered by the L1 trigger, and only open a window of 6.5 μ s after a collision, in addition to the 90 μ s to read out the drift volume.

All these systems work together in order to provide tracks with a resolution between 1100 (inner radius) and 800 (outer radius) μ m in $r\phi$, and between 1250 and 1100 μ m in z . These differences occur due to differing wire configurations on the inner and the outer sectors respectively. The TPC also provides a measurement of energy loss of particles up to 5% resolution in a low-density situation and 6.2% accuracy in high-density PbPb-collisions. The dE/dx information is used to identify particles,

²At the time of the relevant measurements. The gas mixture changes over time.

though this study will not make use of these capabilities.

3.2.3 V0 detector

There are two sets of scintillator counters at both sides of the collision point that detect particles produced at low angles after the collision. The V0A is located at $z = 340$ centimetre ($2.8 < \eta < 5.1$) and the V0C at 90 centimetre ($-3.7 < \eta < -1.7$) in the opposite direction are together known as the V0 detector. Charged particles caught by one of the scintillating plates are again emitted as photons that are guided by optical fibre to photomultipliers. The signal in each sector of the detector is proportional to the multiplicity. The detector is shaped like an annulus around the beampipe, with 32 counters arranged in 4 rings and 8 sectors in ϕ for both the V0A and the V0C. The V0 detectors serve as a triggering instrument and to provide multiplicity information on collisions. In this work we will use the detector to determine the event plane orientation. Both aspect will be elaborated on in Section 3.3.1.

3.3 Event and track reconstruction

3.3.1 Event reconstruction

Events are reconstructed by recording all signals from the sub-detectors in a time frame around the firing of a certain trigger. In principle it is possible that this includes signals from other collisions that happened either simultaneously, or during other bunch crossings within the integration time of the detector. This phenomenon, and the ‘unwanted’ signals during a event, is known as pile-up. Pile-up events can often be filtered after reconstructing the tracks as we will discuss in Section 3.3.2 and reconstructing multiple primary vertices. The tracks coming from one of those vertices can then be discarded. For run 1 the pile-up is negligible.[9]

Triggers and centrality

In the ALICE experiment, collisions during the 2011 lead-lead run happen up to a frequency of four kHz, and this number is even higher in later data periods. While larger interaction rates allow to detect rare processes, there are limits to the readout rate, e.g. from space charge effects in the TPC (see Section 3.2.2) and the bandwidth that is available for shipping data to permanent storage, which mean that not all collisions can be recorded. There is also a limit on the amount of data that can be added to long term storage every year. The practice of triggering, only recording the more rare and/or interesting events based on some trigger, is often used in particle physics experiments to remedy this problem.

Simply triggering on the presence of a collision is called a minimum bias trigger. It is also possible to trigger on more rare events, if the total amount of events that were inspected by the trigger is also registered for the purpose of normalisation. The factor of the number of triggered events by the number of total events becomes a correction factor on most computations. For the data sample used in this analysis, events were

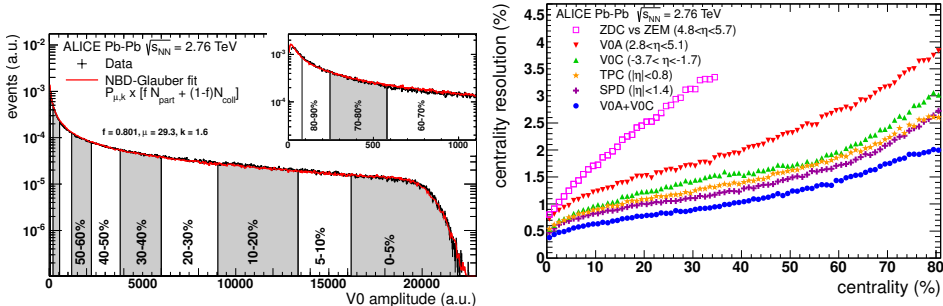


Figure 3.5: Left: The amount of events the V0 measures with a certain amplitude. It is fitted with an NBD-Glauber model, and divided in 10 equal centrality classes. Right: The resolution of the centrality determination of several detectors.

Source: [9], both

selected to be within the centrality range 20-50% based on the multiplicity in the V0. The left side of Figure 3.5 shows that a NBD-Glauber model as discussed in Section 1.2.3 can be fitted to the distribution of the strength of the V0 signal over many events. The event sample is divided into centrality classes based on the integral under the curve. In this case it has been divided in equal bins of 10%, with the most central collisions split into two 5% bins. When using both V0 detectors to determine the centrality, the centrality can be determined with a resolution of about 1% up to 50% centrality as can be seen in the right panel Figure 3.5.

Event plane determination

When determining the event plane and other quantities based on the same finite number of tracks, some unintended correlations between the observable and the event plane can be introduced. In order to avoid artificial correlations between the event plane and the particles we want to measure, the event plane is determined with data that is not coming from the TPC and ITS. Therefore the V0 is used for the event plane reconstruction, using the method described in Section 1.3.1. The event plane resolution for the V0A and V0C is shown in Figure 3.6. It has been determined by comparing the event planes determined by the V0A, V0C and the TPC for the same event. The figure also shows correlation coefficients between the event planes.

3.3.2 Track reconstruction

Charged tracks are reconstructed using the combined information of the TPC and ITS, using a Kalman filter. A Kalman filter is an algorithm that performs a track fit by subsequently adding hit information from each tracking layer.[25] It extends the fit from the (parametrised) track it has found up till then to the next layer based, finding the most probable hit in that layer. It then updates the parameters at that point using the location of the fit in the next layer. It also introduces some stochastic

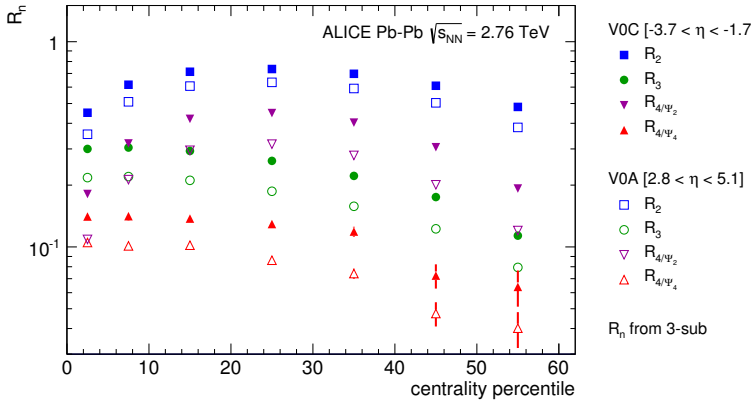


Figure 3.6: Event-plane resolution Ψ_n for $n = 2, 3$, and 4 , calculated with a three-detector subevent technique separately for the V0A and V0C detectors. In this thesis R_{4/Ψ_2} from the plot is commonly called R_4 .

Source: [9]

variable that can account for small stochastic deviations in either the position of the track, occurring for instance due to measurement errors, and deviations in the momentum of the track, occurring for instance due to scatterings in the material.

The Kalman filter needs a good initial state to work with in order to produce the aforementioned fit. This is done by a seed finding algorithm.[24] Since the particle density at the outer edge of the TPC is a couple of thousand times lower than in the inner layer of the TPC, it is beneficial to start there. First the analogue signal of the TPC is clustered in ϕ and z bins. Then the outermost few pad-rows of the readout of the detector are studied. All clusters on the outermost pad-row are paired with the clusters on a pad-row that is 20 rows closer to the interaction point. These clusters also have to be within reasonable distance (in η - ϕ space) from each other. A helix is drawn for each of these combinations, that also intersects with the interaction vertex. Here an approximation of the interaction vertex is used that has been constructed using only the ITS. After suitable seeds have been determined, this restriction is dropped. Then the Kalman filter will course correct to an even more accurate determination of the primary vertex. The algorithm then looks for clusters along the trajectory, and if a large enough clusters can be found alongside this track, then this combination is saved as a seed. Otherwise the algorithm will study the next combination. These seeds are the initial state for the Kalman filter.

The Kalman filter is then run in parallel. This means that all the tracks are propagated simultaneously to the next layer, before the clusters on that layer are disentangled and assigned to the most probable track. It is possible that a track will end up without a new cluster in that layer, in that case it proceeds on its current track. When the track reconstruction in the TPC is completed, the track is evaluated. If it does not contain enough clusters it is rejected. The successful tracks will then go

into the process of ITS-TPC track matching.

Mismatching could of tracks between the ITS and the TPC could occur due to the considerable dead zone between the two detectors and the high track density in the ITS. Therefore all the layers of the ITS are considered simultaneously when linking them to the TPC tracks. This can be done with a primary vertex constraint and without this constraint.

When the TPC-ITS matching is finished, the Kalman filter is run once more, but this time in the outward direction. During this run it only considers the clusters associated with this track. It uses this reverse procedure to smoothen out the tracks by removing outliers. Then a last inward tracking pass is performed. Here the track parameters are adjusted based on the previous pass, without the earlier restriction to a primary vertex. This allows for the reconstruction of possible secondary vertices. This last inward refit on the entire ITS will be relevant later on in Section 4.2.2. The tracks are then stored in a different data format to be used by the analysers at greater convenience. The entire process has a considerable amount of variables which are still left to be determined by the analyser, based on the priority of the analysis. This work uses a set of tracks which are internally known as ‘hybrid tracks’, which will be discussed more in depth in Section 4.2.2.

Using the tracks constructed from the ITS and TPC combined, the interaction vertex can determined with a resolution in the order of $10\mu\text{m}$.[9] Since the distance between primary interaction vertices in pile-up situations can typically be measured in millimetres to centimetres, this is small enough to determine which tracks belong to this event.

3.4 Software

The analysis of these large datasets requires specific soft- and hardware. This analysis was performed using the AliROOT software package.[37] This is an ALICE specific package that has been built on top of the ROOT software toolkit,[33] which is written in the C++ programming language. Where ROOT helps with the basic analysis, computations and plotting of results, AliROOT contains a lot of detector specific data and functions to directly address tracks in an object oriented manner.

Processing the large datasets requires a distributed parallel computing network. The LHC computing GRID infrastructure[65] provides scientists the opportunity to distribute their computations across 170 computing centres in 42 countries. For ALICE a user friendly shell AliEn (ALICE Environment Grid Framework)[51] has been developed. This allows the code to be sent to the computing centres and processed there locally on small subsamples of the data, with the aggregate data being collected and merged afterwards. This method of working does require attention on the part of the analyser, as it requires code that can be processed in parallel without knowledge of the rest of the data. This becomes relevant with event mixing in Section 4.3.2.

In order to correct for the detector efficiency, simulations of events and their interaction

with the detector have to be run. For this analysis both simulations of proton-proton collisions and of lead-lead collisions were used. For the former, Pythia[72] has been used, while HIJING (Heavy-Ion Jet Interaction Generator) simulations[80] have been used for the heavy ion collisions. These simulated events are then processed by GEANT[30] in order to simulate their interactions with the ALICE detector in realistic conditions. The simulated detector signals are stored and are then treated in the same way by the reconstruction software as the collision data. The resulting tracks and vertices are stored in a format similar to the other data from the experiment. In this way analysers have a dataset with both the ‘Monte-Carlo truth’ and the ‘measured’ results, necessary to compute efficiency matrices.

Chapter 4

The analysis

4.1 Analysis concept

As discussed in Section 1.4.1, the amount of quenching a jet undergoes is expected to be dependent on the distance a parton travels through the medium. A non-central heavy ion collision is not azimuthally symmetric as discussed in Section 1.3. Jets leaving the collision in-plane have on average shorter in medium path length than jets leaving the collision out-of-plane. The impact of the path length on energy loss can be studied by comparing the in-plane, mid-plane or out-of-plane jets, using the definitions demonstrated in Figure 1.11. The yield associated with a trigger can be measured using a azimuthal distribution of dihadron correlations as a function of the angle of the trigger with the event plane. To measures differences over this angle, the flow background in dihadron histograms is subtracted with help of the model described in Section 1.5.4 with lessons learned from Section 2.3. The jet yield of both near- and away-side jets that can be compared for trigger particles with different orientations with respect to the event plane. The advantage of this observable is that the ratio between the in-plane and out-of-plane jet yield is not susceptible to the selection bias that is present when determining the near-side jet in di-jet imbalance studies as discussed in Section 1.4.3.

To enable comparison to previously reported results, the results are also compared to pp collisions. In Chapter 5 the analysis is repeated in a Monte Carlo simulator in order to check whether current theoretical predictions match the current results.

4.2 Data selection

For this analysis a 2011 PbPb-collisions at an energy of $\sqrt{s_{NN}} = 2.76$ TeV was used. In the pp-comparison data the $\sqrt{s} = 2.76$ TeV data of 2011 was used. For the di-hadron correlation measurement it is important that on average the particle distribution in ϕ and η is uniform. Any runs from the period that did not have a

uniform ϕ and η distribution due to detector effects have been filtered from the data.

4.2.1 Cuts on events

The events used in this analysis were selected online by a minimum bias trigger and a semi-central trigger which selected events between 20% and 50% centrality based on the signal in the V0 (see Section 3.3.1). All events outside this mid-central range have been cut. The lower boundary has been placed in order to provide collisions with a sizable asymmetry. This increases the in medium path length difference between in and out of plane jets. The upper boundary has been placed in order to find events with large enough temperature and density to have a non-unitary I_{AA} . At higher centralities there is a higher variance on the multiplicity in the TPC at a given centrality bin as measured by the V0. To further clean up the events that deviate strongly from the average TPC multiplicity have therefore been removed. Events with a centrality between 40% and 50% are only accepted if a minimum of 1160 tracks are accepted for the dihadron analysis. With these selections, even the selections in the TPC, the centrality distribution of the events is uniform for the V0 in this domain.

In the pp-data all minimum bias events were used.

Furthermore all events with a position of the primary vertex further than 7 cm of the centre of the barrel are discarded in both the PbPb and pp analysis. This cut reduces variations in the pseudo-rapidity acceptance from event to event.

4.2.2 Hybrid tracks

It is important for this analysis that the track distribution is as uniform in the azimuthal direction as possible. Therefore it was chosen to follow the hybrid track selection from [75]. It is optimised to ensure a uniform acceptance of reconstructed tracks in η and ϕ . This is particularly important since for parts of the 2011 PbPb run some ladders of the SPD had to be turned off due to a problem with the flow of cooling water. Since the goal of this analysis is to compare the PbPb events and the pp events, the same track cuts were used in both. Only charged particles are included in the analysis, which means all statements henceforth will be about charged jets.

To achieve a uniform acceptance in ϕ a set of high quality tracks is supplemented with tracks of a slightly lower quality to fill the gaps to form a set of hybrid tracks. Table 4.1 shows a list of the hybrid track selection cuts. $N_{\text{clusters,TPC}}^{\text{iter 1}}$ is the number of clusters associated with the track on the first tracking pass, and a cut prevents the inclusion of fake tracks. The χ^2 in $\chi^2/N_{\text{clusters,TPC}}^{\text{iter 1}}$ is the χ^2 of the fit through the TPC, and when the ratio is too large, it is likely that this track was not constructed properly. The ITS and TPC refit have been described in Section 3.3.2, and whether or not these procedures succeeded functions as quality assurances on which tracks can be selected. The $d_{0,xy/z}$ are the distance of closest approach to the primary vertex in respectively the xy -plane or the z direction, and a cut removes most of the products from weak decays. The cut on fraction of shared clusters is to filter tracks that contain a lot of ambiguity. If a particle decays halfway through the detector, the daughter particles can suddenly change momenta and may or may not be charged,

		Global Standard
1	$ \eta $	< 0.9
2	Reject kinks	true
3	TPC refit	true
4	Fraction shared clusters	< 0.4
5	χ^2_{ITS}	< 36
6	$\chi^2_{\text{Global-TPCconstrained}}$	< 36
7	$d_{0,xy}$	< 2.4
8	$d_{0,z}$	< 3.1
9	$\chi^2/N_{\text{clusters,TPC}}^{\text{iter 1}}$	< 4
10	$N_{\text{clusters,TPC}}^{\text{iter 1}}$ for $p_T < 20 \text{ GeV}/c$ $N_{\text{clusters,TPC}}^{\text{iter 1}}$ for $p_T > 20 \text{ GeV}/c$	$> 70 + 1.5p_T$ > 100
11	ITS refit	true
12	SPD hit	at least 1

Table 4.1: A list for the hybrid track cuts. For explanation of the symbols: see text. Constraints 11 and 12 are only used for the ‘good global’ tracks, and are dropped for the ‘complementary’ tracks.

Source: [75]

and as such, detectable. This could happen, for instance with the decay of a kaon or pion to a muon-neutrino pair. If just one of the daughters is neutral, this might read as a track with a kink in the middle. The reject kink criteria makes sure that daughter tracks are discarded, keeping the mother if that tracks has a long enough path through the TPC.

It would be ideal to only use global tracks that are both measured in the SPD, and have a good fit in the full ITS. In this case, 79% of the tracks, the angle and momentum measurement of that particular particle are as accurate as possible. When the no hits in the SPD were found (cut 12 from Table 4.1), most likely due to the missing SPD ladders, concessions have to be made. In that case, 15% of the tracks, tracks were used where particles have a good fit in the remaining layers of the ITS, but the tracks were constrained to the primary vertex in order to improve the p_T resolution. The track is of even worse quality if the SPD layers were missing, and the ITS-refit of the Kalman model failed (cut 11 from Table 4.1). These tracks were needed to fill the last 6% of the tracks. Figure 4.1 shows the azimuthal distributions of the three types contained in the hybrid tracks. The figure clearly shows that requiring a hit in the ITS leads to large inefficiencies in some ranges of azimuth and that the use of tracks without SPD hits is needed to achieve high efficiency in those areas.

4.2.3 Cuts on track pairs

There are also cuts placed on track pairs in addition to the cuts on single tracks. If a track pair is cut, this only refers to that particular pair for the azimuthal di-hadron

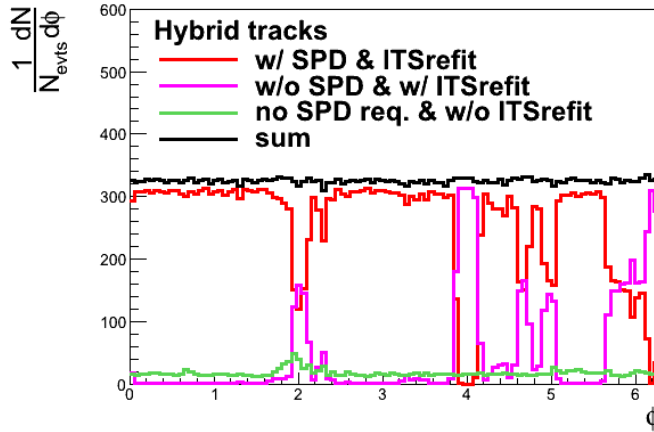


Figure 4.1: The distribution for the hybrid tracks. Together they are flat in ϕ . The high quality tracks (red) represent 79% of the total tracks. 15% is of middle quality (purple) and 6% is of lower quality (green).

Source: [53]

correlation distribution. The individual tracks can still be paired with other tracks in the event.

- In the dihadron histograms used for analysis, a further cut is applied at $|\Delta\eta| < 1.3$ before performing the analysis. Due to detector acceptance the statistics, and therefor the statistical accuracy, at these values drops rapidly.
- When two particles have an angular difference of less then 0.02 upon entering the TPC, the pair is cut from the dihadron histogram and when computing the efficiency correction we will discuss in Section 4.3.2. This is done because these track can be the result of track splitting: one track that is falsely reconstructed as two particles with similar momenta. This effect could result in an additional peak near $(0, 0)$ in the dihadron histogram, and cannot be compensated for by any of the two efficiency corrections we will discuss. It can also help with correcting for track merging: when two tracks follow the same path are constructed as one.
- The products of the weak decays $\Lambda^0 \rightarrow p^+ + \pi^-$ and $K_S^0 \rightarrow \pi^+ + \pi^-$ are filtered. For each pair with the right charge-signatures the invariant mass is checked against that of a K_S^0 and Λ particle. If they are within 5 keV from the expected mass, the pair is cut from the dihadron histogram. This analysis is performed on charged jets, and the measured decay products are charged. So in theory these particles could be taken into account as possible part of a jet under the sum of their 4-momenta. But since the decaying particles are neutral, they are by definition not part of a charged jet, and therefor their products are removed

from the analysis as well.

4.3 Efficiency corrections

4.3.1 Efficiency corrections from Monte-Carlo simulations

In order to correct for detector efficiencies a prepared Monte-Carlo simulation is used to generate efficiencies. These Monte-Carlo simulations have been specifically generated to simulate the detector response with generated events. For the correction of the PbPb-data an HIJING event generator at $\sqrt{s_{NN}} = 2.76$ TeV with mid-central events (30%-40%) was used, and for the correction of the pp-data a 2.76 TeV Pythia event generator was used. These models are then passed through a virtual ALICE detector with the help of the GEANT software. This simulates how many of the tracks generated in the MC would be detected in the experimental conditions. This results can then be used to estimate the tracking efficiency:

$$\epsilon(\phi, \eta, p_T, N) \equiv \frac{\mathcal{N}_{\text{reconstructed}}(\phi, \eta, p_T, N)}{\mathcal{N}_{\text{generated}}(\phi, \eta, p_T, N)}, \quad (4.1)$$

with \mathcal{N} the amount of reconstructed or generated particles in bins of the angle, pseudorapidity, transverse momentum, and in PbPb also in N , the multiplicity of its corresponding event. Later on the number of detected particles in the experimental analysis is divided by this efficiency factor.

It is important to stress that the simulation software is only used to generate a more-or-less realistic simulated collision wherein the GEANT package and a detailed description of the detector geometry can be used to compute the correction. It might seem that this practice of correcting experimental results with theoretical simulations is a form of very involved circular reasoning. After all, the experimental results are in turn used to create, or at the least fine-tune, those very models. This creates a feedback loop that could theoretically enforce initially small assumptions in the first generation of event simulation software in later versions. However, it should be considered that even if event generating software produces significantly different events, the efficiency derived from these events is relatively insensitive to the details of the event generation. For example it turns out that in ALICE the differences between the low density Pythia events and central PbPb events is only a couple of percent. The simulation model is merely used to provide the backdrop for the correction, not the correction itself.

One way to reduce the dependence on an event generator would be to use the structure of real events as input for the detector simulation. This would involve feeding reconstructed events (without efficiencies) through the detector simulation and using them as a proxy for a real event to construct what would be reconstructed. This can then be used to compute efficiencies. Possibly some shifting and rotation of the events might help with exploring the detector boundaries, though other properties like the ability of the detector to distinguish two close particles, are more challenging to simulate correctly. The quality of the efficiency might decrease in this process,

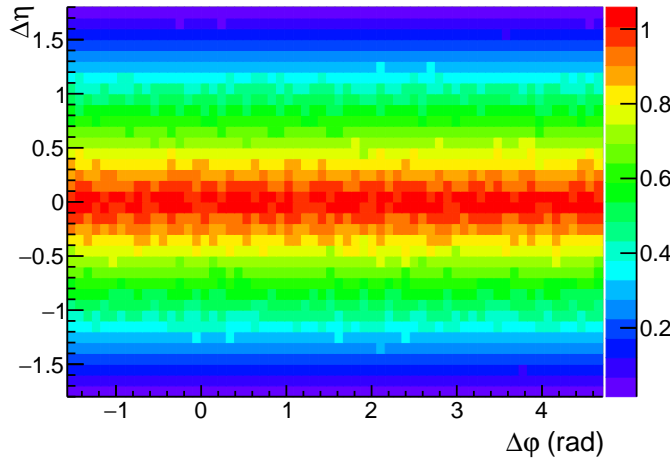


Figure 4.2: An example of a dihadron histogram that is created with the triggers in different events that the associates. It has been normalised such that the four bins around $(0, 0)$ average to 1.

but it would not contain a feedback loop. How feasible this plan is in practice can probably only be determined with a closer dedicated study.

4.3.2 Dihadron efficiency from mixed events

The efficiency correction discussed in Section 4.3.1 corrects for effects of the detector on single particles in a certain area of the detector. Given a certain particle combination, other efficiency effects can be expected, though. A good example is the TPC, which consists of 18 sectors with dead spots in between, as is described in Section 3.2.2. Even after correcting the single efficiency spectra, a fraction of the particle combinations with a relative angle of $\Delta\phi = \frac{2\pi}{18}$ will not be registered. This will lead to a decreased yield at that relative angle. In order to compensate for this, it is customary in dihadron studies to construct mixed events to sample the pair-acceptance. The results are then corrected by dividing by the normalised mixed-event distribution. For this procedure triggers from one event are combined with associates from another event. This way correlations can be found in the efficiency of the detector, which is constant in both events, without the correlations that are present within an event.

The event mixing is performed in bins of $p_{T,t}$, $p_{T,a}$, and the z -position of the primary vertex. The mixed events can also be divided in centrality bins; however, studies have shown that the centrality dependence of the correction is small. Figure 4.2 shows an example of a mixed event dihadron distribution for the ALICE detector. Every bin is used to correct the corresponding dihadron distributions. As is visible in the example, the main effect is the finite acceptance in η . This does have the unfortunate consequence that the corrected dihadron histogram get large uncertainties on their central value at large $|\Delta\eta|$.

The entire $\Delta\eta\Delta\phi$ -histogram is scaled so that the mixed events are normalised to 1 at the four bins around the point $(\Delta\phi, \Delta\eta) = (0, 0)$. Ideally it should be normalised this way for infinitesimal small bins in $\Delta\eta$. The correction factor used to compensate for that fact is

$$1 - \frac{1}{2 \cdot \eta_{\max}} \cdot \frac{\Delta\eta_{\text{bin width}}}{2}, \quad (4.2)$$

with η_{\max} the cut-off value of η in single particle spectrum.

In order to boost the statistics, the code was run twice over all particles. Once to save all triggers, and the second time to combine them with all associates. If the event mixing is done in one run over the data set, the trigger from ‘later’ events, cannot be combined with ‘earlier’ associates. And even far more significant is the fact that the code is run in parallel on the GRID as discussed in Section 3.4 on several batches of the data which are distributed over several computing nodes. The triggers on one node cannot be combined with associates from another. None of this causes any bias, but it does reduce the statistics significantly.

4.4 Jet yield determination in pp

All dihadron pairs are counted in bins in $\Delta\phi$ and $\Delta\eta$. Then the following steps are undertaken:

- The background is estimated by looking at the large $\Delta\eta$ region next to the near-side peak. This is done by averaging the yield in the rectangles where $0.8 < |\Delta\eta| < 1.3$ and $|\Delta\phi| < \frac{\pi}{2}$.
- The circular area N with $(\Delta\phi)^2 + (\Delta\eta)^2 < 1.0$ is integrated.
- The area A with $|\Delta\phi - \pi| < 12\frac{\pi}{32}$ and $|\Delta\eta| < 1.0$ is integrated.
- The average background is subtracted from N and A relative to their area to find the near and away-side yield respectively.

During the process the errors are propagated under assumption that they are uncorrelated. In the context of low statistics at high transverse momentum the quality of this approximation lessens due to non-linear effects. The resulting jet yields are reported in Section 6.1.

More complex approaches have been considered and/or tested but have been ultimately rejected. Statistics were too low to consider a chi-squared approach since empty bins are not taken into account properly in such an approach. These deviations can lead to a bias of the result instead of a lower quality on the error. Furthermore a log-likelihood fit would be a far more complex procedure since each bin in $\Delta\phi$, $\Delta\eta$, $p_{T,a}$, $p_{T,t}$ and the z-vertex should get its own weighting factor due to the mixed event and efficiency corrections. Therefore the contents of each bin are sums of scaled Poissonian distributions. In the low statistics regime the estimations of the weighting factors are subject to statistical fluctuations as well.

Some examples of the azimuthal angle difference distributions with the estimated background are shown in Figure 4.3 for some examples of this fit, or Figure A.1 in

the appendix for all results. To properly interpret the graphs, a short excursion into the different methods for projecting the distributions on delta-phi is necessary, as discussed in the next Subsection 4.4.1.

4.4.1 Weighted average projection

There is a triangular shape in the $\Delta\eta$ dimension of the mixed-event histogram due to the η -acceptance in the detector. When correcting the two-dimensional dihadron histograms with the mixed events this leads to large multiplication factors at high $\Delta\eta$. This is shown in the $\Delta\eta$ -projection in Figure 4.4. If statistics in those bins was rather low to begin with, this might lead to fluctuations with large error bars. Conceptually this uncertainty in those points properly reflects the lack of knowledge of the contents of that bin. However projecting the two-dimensional histograms on $\Delta\phi$ can lead to erratic behaviour that is dominated by just a fraction of the data, in extreme cases even a single bin. In that case it does not represent the bulk of the data, which is around $\Delta\eta = 0$.

To overcome this problem it is possible to project the data weighted with the error bar of the points. This can be justified by considering all bins in $\Delta\eta$ as different measurements of a value for with a specific $\Delta\phi$. This only holds true if the value is expected to be independent of $\Delta\eta$. So if i is the bin number in $\Delta\eta$ and j loops over the bins in $\Delta\phi$, N_{ij} is the pair yield in one of those bins, and σ_{ij} is the error on that value. Then the average value of all bins with index j is

$$\hat{N}_j = \frac{1}{w_j} \sum_i \frac{N_{ij}}{\sigma_{ij}^2}, \quad (4.3)$$

where $w_j = \sum_i \frac{1}{\sigma_{ij}^2}$ is the sum of the weights. To obtain the total yield in a given dphi bin, the value is multiplied by the number of bins in data.

In this procedure, empty bins are problematic because the uncertainty cannot be determined in a model-independent way. It was decided to simply ignore empty bins when making the projections, i.e. they do not contribute to the mean. This biases the results in the figure in those cases. Note that this only affects the projections; the associated jet yields are calculated by summing the yields in the relevant area directly.

4.5 Jet yield determination in PbPb, with trigger selection

4.5.1 Fitting the background

In PbPb-collisionsthe higher multiplicities and azimuthal anisotropies create a background that is higher with respect to the jet yield and varies in $\Delta\phi$. To model the background we make use of equations 1.38 through 1.49. These equations do have a few parameters relating to the event plane resolution and correlations which still

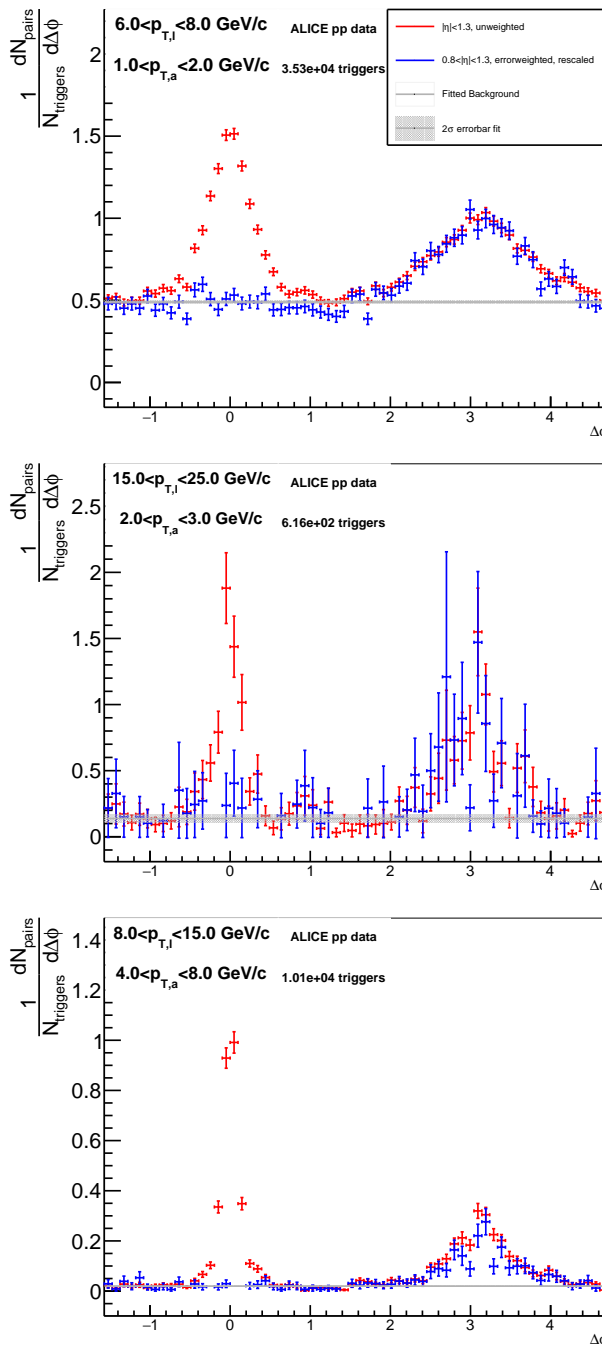


Figure 4.3: The $\Delta\phi$ -projections of the pp-data for several p_T -ranges. See Figure A.1 for the rest of the fits. The colours represent projections of the data over different η -ranges. In some cases there are no dihadron pairs with $0.8 < \Delta\eta < 1.3$, then the blue points are missing from the figure.

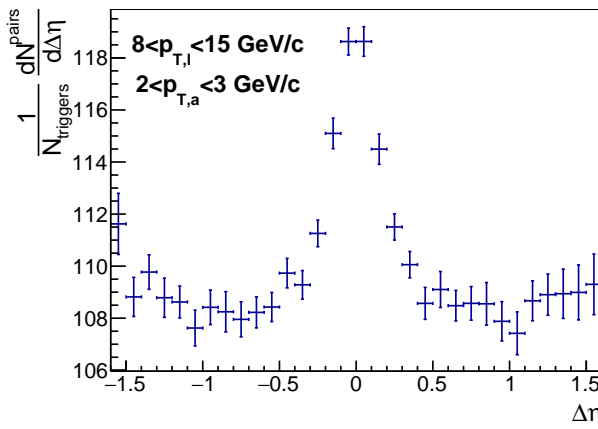


Figure 4.4: An example of the $\Delta\eta$ -projections of the PbPb-data for the $8 < p_{T,t} < 15$ GeV/c, $2 < p_{T,a} < 3$ GeV/c bin.

need to be determined. In the following, we will first explain the procedures that were used to obtain these parameters and then the values of these parameters will be studied. Afterwards the obtained parameters for different momentum combinations will be compared to check their consistency.

Fitting procedure

The background is fitted on the range outside the jet-area. There are two relevant regimes that are distinguished in the fitting procedure. If all bins in the fitting area contain at the very least one particle pair, the background is estimated with a χ^2 -fit. The background determination of the momentum-domain where the $\Delta\eta - \Delta\phi$ -histogram contains any empty bin is performed with a Fourier-like analysis which is explained in Section 4.6. After establishing the background level it is subtracted from the data and the jet area is numerically integrated. The near-side and away-side jet-area's are designated as follows. The centre of the bin at $(\Delta\eta, \Delta\phi)$ has to satisfy

$$\Delta\phi^2 + \Delta\eta^2 < 1.0 \quad \text{for the near-side area,} \quad (4.4)$$

$$|\Delta\phi - \pi| < 12 \frac{\pi}{32} \quad \text{and} \quad |\Delta\eta| < 1.0 \quad \text{for the away-side area.} \quad (4.5)$$

The away-side peak area is limited to $|\Delta\eta| < 1.0$ to prevent excessive outliers in the tails of the η -distribution from increasing the statistical error. However ‘outside the away-side peak area’ refers to all points lying outside the mentioned $\Delta\phi$ -range, since the away-side peak is still present, even in the large- $|\Delta\eta|$ range.

In the case that there is sufficient statistics, a simultaneous χ^2 -fit is performed with Minuit’s MIGRAD algorithm on the bins with trigger particle orientations with respect to the event plane (‘orientation bins’) of one particular $p_{T,t} - p_{T,a}$ -bin. Only the contribution of bins outside the near and away-side area to the χ^2 are counted.

Errors on the parameters are discarded since in Section 2.2.3 it was shown that these are not reliable in most cases, and they are recalculated using the bootstrapping procedure detailed in paragraph 2.2.3. In principle 6 variables are part of the fit: the overall background level B , the trigger particle flow v_2^t , the associated particle flow v_2^a , the $p_{3,\text{red}}$, v_4^t , and v_4^a . There is one exception to this procedure. When $S_{4,4} = 0$, the equations 1.44 through 1.46 are dependent only on the product $p_{4,\text{red}}$. Therefore in practice v_4^t is fixed during the fit.

After the background is determined, it can be subtracted and a simple numerical integration over the areas in equations 4.4-4.5 is performed. This results in the final reported yield for the near-side and the away-side peak. Only the values are stored, errors are computed via the bootstrapping method. We attempted to fit the entire model including the jet peaks. However in the end it was chosen not to do this, because the non-Gaussian tails of the jet peak resulted in fits that were less stable than was desirable, even during attempts with a generalised Gaussian.¹ Therefore this method, which does not rely on a peak shape model, was chosen.

When there are empty bins in the $|\Delta\eta| < 1.3$ domain, the χ^2 -fit would not yield accurate results. At the high leading and associate momentum domain in principle the overall background level B is negligible, as are all orders of the composite flow p_n . Then it would suffice to assume the background to be flat, and can be subtracted using the same procedure as in pp-collisions. Unfortunately there is a region at moderate large momentum where there is still a considerable flow contribution, yet there is not enough statistics to perform a χ^2 -fit. Because of the rescaling that happens due to the event mixing, implementing a logarithmic likelihood fit with non-Gaussian assumptions is rather involved. We have also explored the possibility to integrate the area $(|\eta|, |\phi|) \in [0.5, 1.0] \times [-\frac{\pi}{2}, \frac{\pi}{2}]$, where any p_2 contribution cancels automatically. The p_2 could then be reconstructed per plane by integrating the area around $\phi = \pm\frac{\pi}{2}$. It was, however, not possible to get a consistent picture of the background modulation between the planes, and the jet yield was very susceptible to changes in the area of integration. Therefore this method was abandoned. Similarly a method that tried to estimate a p_3 based on a few data points was abandoned. Instead a Fourier-like method as described in Section 4.6 was used.

4.5.2 Determining the interaction between event planes

This still leaves the question what values should be used for the R and S parameters mentioned. Of the 5 relevant parameters only R_2 has any previous measurement. In principle it should be possible to measure the other 4 parameters in an independent analysis. However it will turn out that the exact value is not that relevant to the results.

The value of R_2 for the V0A and the V0C at 20% to 50% centrality can be read out in Figure 3.6. Since we use the event plane that is reconstructed with both the V0A and V0C, the combined event plane resolution is slightly higher. This results in an R_2 of 0.75 in this centrality range. [10] Based on Figure 3.6, variations of the resolution

¹I.e. a Gaussian with a free power in the exponent; this power is equal to 2 for a regular Gaussian.

within a range of 0.05 around the central value will be studied. Idem the R_4 can be read out to vary between 0.3 and 0.5. The values of $R_4 = 0.4$ and a $R_8 = 0.07$ were determined with the toy MC simulation of Chapter 2.2.1 as they were consistent with an R_2 value of 0.75. An uncertainty of ± 0.05 in R_2 suggests that R_4 would have a uncertainty range of $0.35 - 0.5$ and R_8 a uncertainty range of $0.05 - 0.12$.

The remaining unknown parameter is $S_{4,4}$, which characterises the correlation between the orientations of the second and fourth order symmetry plane. This is a physical parameter, for which we have only limited experimental information. To explore the sensitivity of the fit to this parameter, we perform a fit for various values of the $S_{4,4}$. Equation 2.2 assumes a Gaussian distribution between Ψ_2 and Ψ_4 . This assumption is chosen to place restrictions on the values $S_{8,4}$ can take. It might not be completely true, but hopefully gives an acceptable approximation for $S_{8,4}$ as function of $S_{4,4}$. From the assumption follows that $S_{8,4} = (S_{4,4})^{\frac{8^2}{4^2}}$.

The histograms drawn in Table 4.5 are the average of 50 iterations of $\Delta\phi$ -projections (Section 4.4.1) with the bootstrapped error bar. In red the average of the weighted projections is taken, and in blue the average of the regular projections is taken. The transparent grey lines are the 50 resulting fits of individual bootstrap iterations. Two items of note should be considered with these plots. Firstly the fit is purely there to describe the background, and therefore might/should not follow the data points around the jet peaks. Secondly due to the fact that it is the weighted average over the η -domain, the near side peak does not represent its true size. Inspecting the figures, we note the following points:

1. The in-plane and out of plane fits do not change visibly with varying $S_{4,4}$. All differences are strictly contained to the mid-plane bin. This can be explained by comparing the scales on the y-axis. The in- and out-of-plane have a significantly larger difference between the highest and lowest points on the graph. This means that a χ^2 -type fit will ‘prioritise’ the steep curves of these fits since a larger gain in the loss-function can be achieved, and as such the v_n -coefficients are more susceptible to the shape of the in- and out-of-plane then the mid-plane data.
2. The uncorrelated model when ($S_{4,4} = 0$) does not match the data very well. It does not capture the characteristic ‘cat ears’: the double peak around $\Delta\phi = \pi \pm \frac{\pi}{4}$. It could either be some very exotic bimodal form for the away-side jet peak, or a negative $p_{4,\text{mid}}$ contribution within the current background model. Since the former is very unlikely from a physical standpoint, the latter is probably the case. Equation 1.45 shows that $p_{4,\text{mid}}$ can be negative, but when $S_{4,4} = 0$ this is impossible.
3. Between $S_{4,4} = 0$ and 0.1 there is a transition where there are some iterations of the bootstrap that result in a fit with a negative composite 4-flow, and some iterations where the model did not consider that viable. On careful study one can see that for $S_{4,4} = 0.1/3^2$ the peaks caused by a negative p_4 in the fit are already shrinking, and do not properly follow the data.
4. Finally at $S_{4,4} = 0.1$ and above the model is remarkably invariant to the specific

value of $S_{4,4}$. At a glance it is impossible to tell the difference between these scenarios. This means that the choice of the $S_{4,4}$ parameter can be compensated for with the other parameters in the model.

5. There is some tension visible in the plots, even at the higher $S_{4,4}$. This is apparent especially in the mid-plane around the minima around $\pm\frac{\pi}{2}$ and in the near-side where the weighted projection of the background is significantly lower than the results of the fit. We will discuss this at a later point in Section 4.9.2.

To elaborate on point 2 and 3 above, according to Equation 1.45, a negative $p_{4,\text{mid}}$ can be reached when

$$v_4^t < \frac{\alpha R_4 S_{4,4}}{1 + \frac{\alpha}{2} R_8 S_{8,4}} \approx \alpha R_4 S_{4,4}, \quad (4.6)$$

where all terms on the right hand side are positive. The last approximation is valid because $\frac{\alpha}{2} R_8 \approx 0.05 \ll 1$ and $S_{8,4} \leq 1$. Therefor if the $S_{4,4}$ is sufficiently large a negative $p_{4,\text{mid}}$ can be constructed. Figure 4.6 shows that above this threshold $S_{4,4}$ the underlying v_4^t and v_4^a parameters can change almost an order of magnitude, but this results in relatively small changes in the resulting p_4 -values. Furthermore it is an interesting detail that the difference between $p_{4,\text{in}}$ and $p_{4,\text{out}}$ is only dependent on the terms containing $S_{4,4}$ and v_2^t , aside from the term in the denominator.

The parameter $p_{3,\text{red}}$ is independent of $S_{4,4}$ by definition of Equation 1.50. Figure 4.7 confirms there is no significant difference between the fits with two different values of $S_{4,4}$. When dividing through the number of triggers, in the form of $\beta^{\text{in/mid/out}}$, a small $v_{2/4}^t$ dependence is introduced. This can explain the small downward trend that $p_{3,\text{red}}$ in Figure 4.7.

The situation in Figure 4.8, where the dependence of the second order flow coefficients on $S_{4,4}$ is shown, is different. Changing $S_{4,4}$ leads to significant differences in v_2^a . When translating this to the p_2 values, the differences vanish in all cases but the mid-plane case. Based on these results, we decided to treat $S_{4,4}$ as an additional source of uncertainty, rather than determining the exact value of $S_{4,4}$.

The question of how much this influences the jet yields is crucial to whether this approach is valid. Figure 4.9 shows that for this particular bin the changes in the yield due to changing $S_{4,4}$ are clearly insignificant with respect to the statistical uncertainties. Within this momentum range and with this amount of data, there is no further need to determine $S_{4,4}$ more precisely. Later on in Section 4.8 we will discuss the remarkable differences between jet yields when the trigger changes orientation bin. The important conclusion here is that $S_{4,4}$ has to be large enough to explain the negative p_4 in the mid-plane according to Equation 4.6. In addition there is no reason to assume that $S_{4,4}$ is dependent on the transverse momentum, since the event plane is independent of the momentum of the particles. This means that $S_{4,4}$ has to be significantly larger than 0 for the entire $p_{T,a}$ and $p_{T,t}$ domain.

In conclusion we can state that the ‘cat ears’, the double peak in the away-side structure, prove the need for a non-zero correlation between Ψ_2 and Ψ_4 , because a negative p_4 can not be reached in any other way. However, when $S_{4,4}$ is above a certain threshold (about 0.15), the exact value is not that important. The model

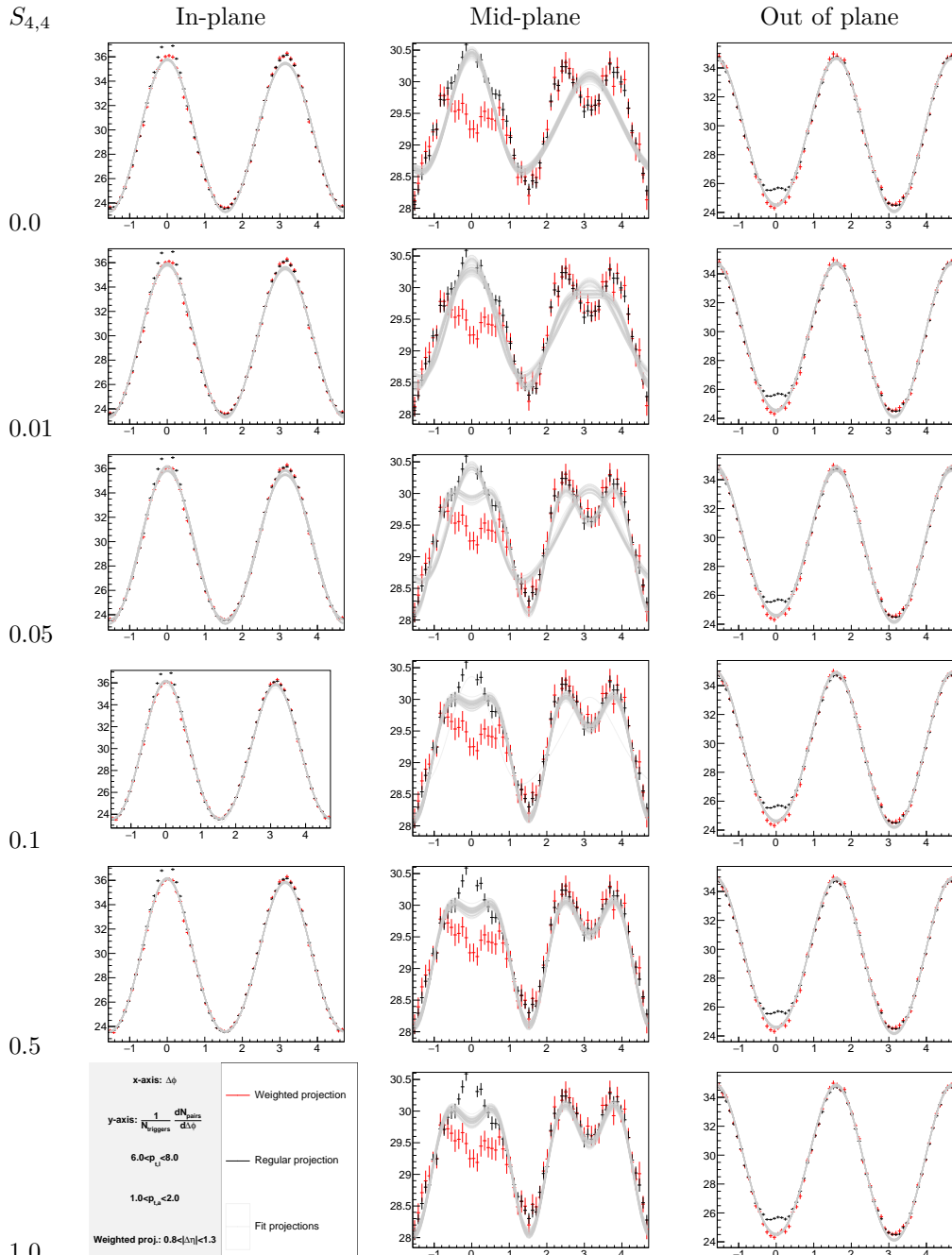


Figure 4.5: The $\Delta\phi$ -projections are the average and variation of the 50 bootstrap iterations for the $6 < p_{T,\text{t}} < 8$ and $1 < p_{T,\text{t}} < 2$ bin in the PbPb ALICE data. The red points represent the weighted average projection of the background area, and the blue points the regular projection of the entire range. The transparent grey lines are the 50 individual results of the fits. This is performed for several values of $S_{4,4}$ and shown for all orientation bins. The covered panel in the bottom left is visually indistinguishable from the one above.

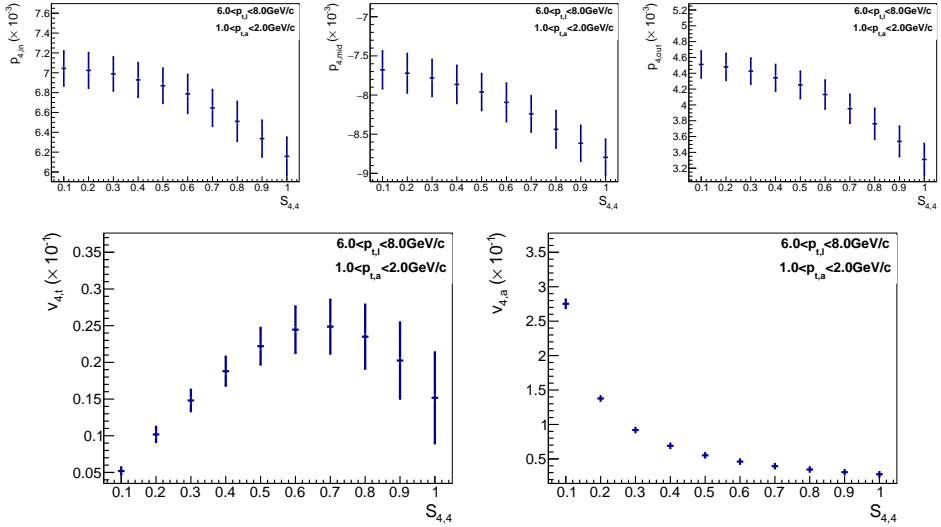


Figure 4.6: Top panels: the resulting composite flow p_4 depending on the $S_{4,4}$ parameter used in the model. Bottom panels: the underlying trigger and associate flow parameters found depending on the $S_{4,4}$ parameter used in the model.

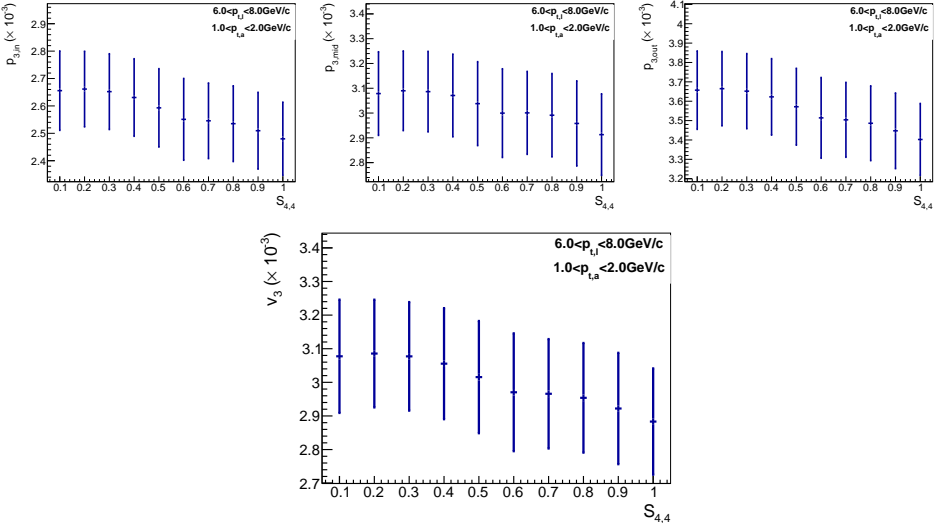


Figure 4.7: Top panels: the resulting composite flow amplitude p_3 as function of the $S_{4,4}$ parameter used in the model. Note the difference in the scale of the y-axis. Bottom panel: the dependence of the product of the underlying trigger and associate flow parameter on the $S_{4,4}$ parameter used in the model.

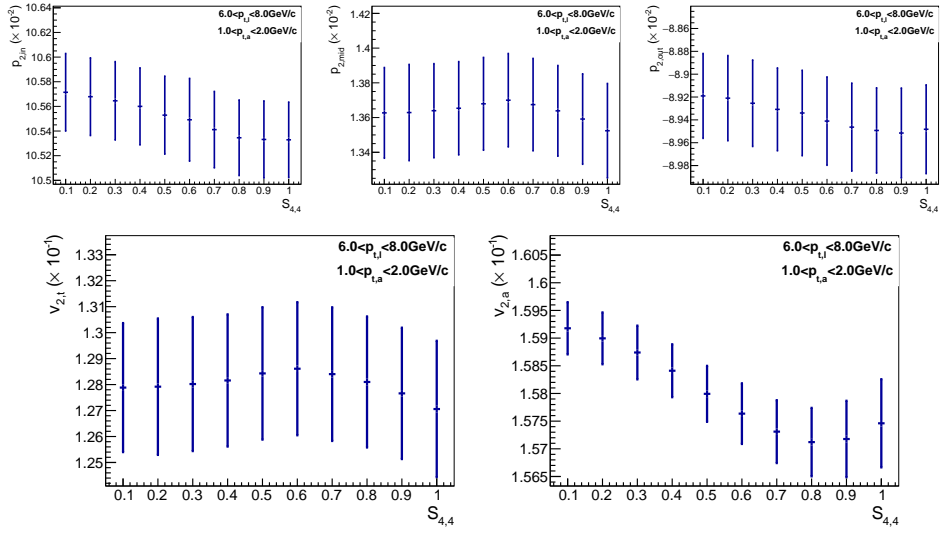


Figure 4.8: Top panels: the resulting composite flow p_2 depending on the $S_{4,4}$ parameter used in the model. Bottom panels: the underlying trigger and associate flow parameters found depending on the $S_{4,4}$ parameter used in the model.

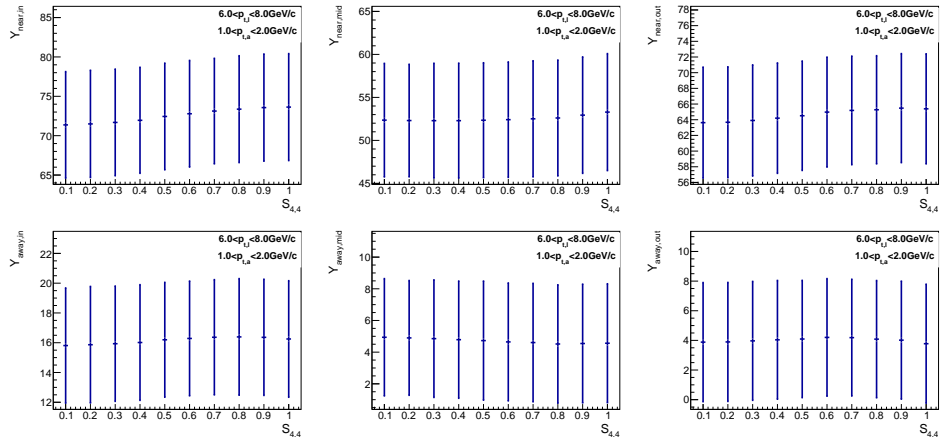


Figure 4.9: The resulting charged jet yields depending on the $S_{4,4}$ parameter used in the model. Above the near-side yields, below the away-side yields. Note that different scales have been used on the y-axis. From left to right: in/mid/out-of-plane.

will be able to absorb all further changes in $S_{4,4}$ by adjusting the flow amplitudes. Reasonably sized changes in R_4 and R_8 can be absorbed as well. It compensates so a consistent value of the jet yield is produced. The values of $p_{T,t}$ and $p_{T,a}$ are more sensitive to the value of $S_{4,4}$, and this also affects the consistency between the p_n values for leading and associated particles as will be discussed in Section 4.5.3. But because the values of the flow parameters are not the main concern of this study, it is far more important to note that the variations in the resulting jet yields are well within their statistical uncertainty. Figure 4.9 shows that the uncertainty due to changes in $S_{4,4}$ can therefore be described as a relative systematic uncertainty of a couple percent or less. The size of this uncertainty is small compared to the other sources.

4.5.3 Determining parameter consistency as function of p_T

There is an interesting way to independently confirm the validity of the model. In principle all v_n^t should be independent of $p_{T,a}$, and conversely all v_n^a should be independent of $p_{T,t}$. The results of the former test are visualised in Figure 4.10. The plot takes into account several values of the $S_{4,4}$ parameter. The results of the reverse test can be found in Figure 4.11. In principle one should expect this to result in a flat line within uncertainties.

For low values of $S_{4,4}$ there is a clear difference in the flow-parameters in most cases. For higher values most of the flow parameters are compatible within uncertainty. Exception to the rule is the v_2^t . It is notable that this is also the parameter that has to do most of the work in equations 1.38-1.49 to get the ratios between the flows in the in/mid/out-plane right. There is not nearly enough precision in these measurements to use them to estimate a reasonable value for $S_{4,4}$, and in principle the $S_{8,4}$ should be varied independently as well instead of using Equation 2.2 as a assumption to link the two.

4.5.4 Determining charged jet yield

Given the fit of the background the charged jet yield is determined through a process similar to the procedure in pp (see Section 4.4). In each orientation bin the following procedure is performed:

- The background is subtracted from the two-dimensional dihadron distribution.
- The pair yield in the near-side circular area N with $(\Delta\phi)^2 + (\Delta\eta)^2 < 1.0$ is integrated.
- The pair yield in the away-side area A with $|\Delta\phi - \pi| < 12\frac{\pi}{32}$ and $|\Delta\eta| < 1.0$ is integrated.
- This procedure is repeated 50 times in total for the different bootstrap samplings of the data. The spread on the determined parameters is used as an estimation of the uncertainty of the results.
- If further quantities that depend on the found parameters are computed, they

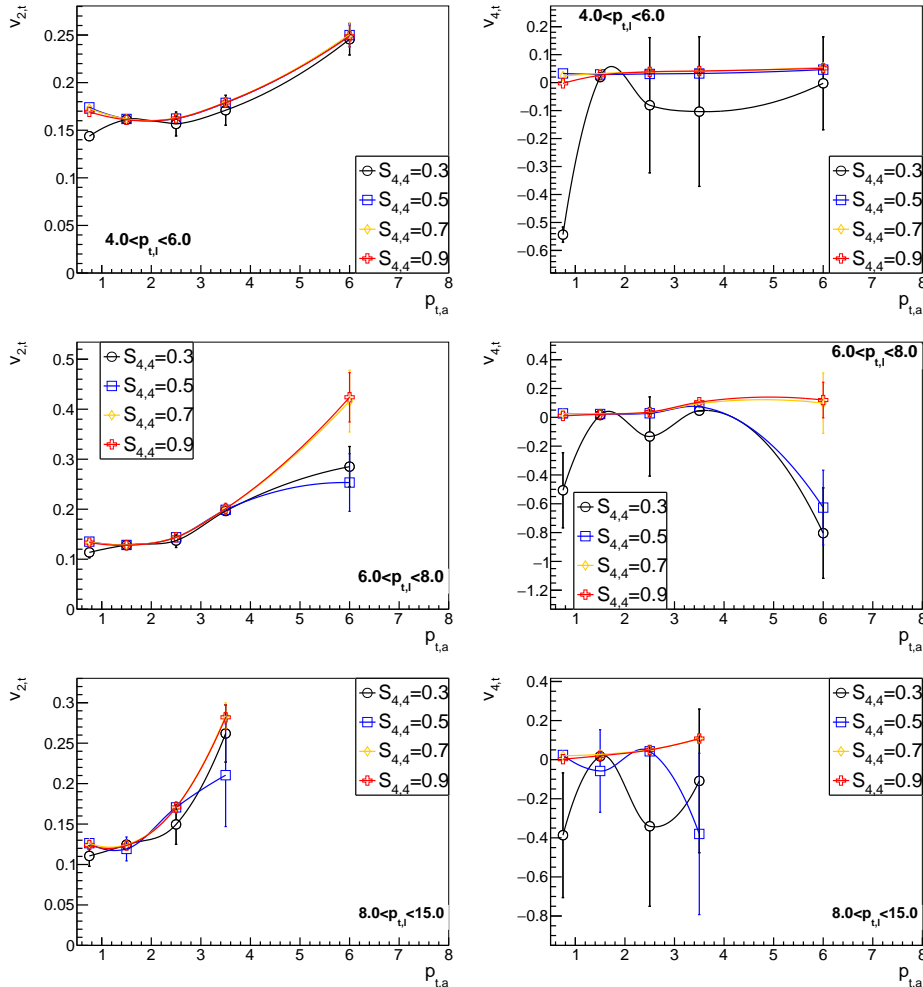


Figure 4.10: The trigger flows as a function of the $p_{T,a}$ for several values of the $S_{4,4}$. In principle one should expect this to result in a flat line within uncertainties. Missing bins are due to the fact that another method is used to establish the background.

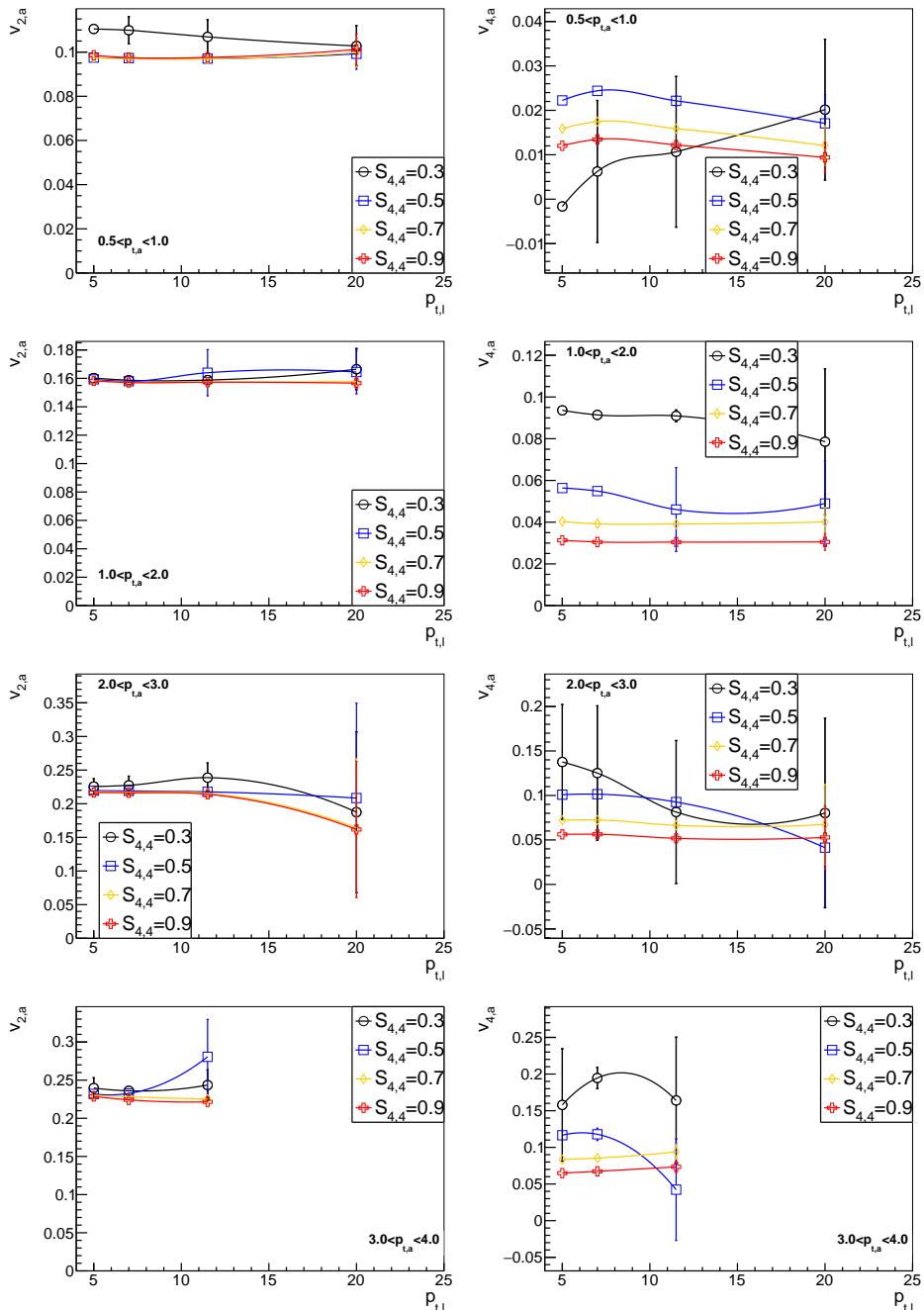


Figure 4.11: The associated particle flow coefficients as a function of the $p_{T,t}$ for several values of $S_{4,4}$. Missing bins are due to insufficient data in the correlation histogram, and therefore it was not possible to perform the χ^2 -fit.

are computed per bootstrap iteration, to determine the uncertainty including possible correlations with other parameters.

Figure 4.12 shows the charged jet yields that are calculated this way. These results are used to create the results in Section 6.2.1. The yield in the $4 < p_{T,a} < 8$ bin is typically higher than in the $3 < p_{T,a} < 4$ bin because the yield is integrated over a larger $p_{T,a}$ –domain. On the away-side there are clearly bins in which the fit does not produce a stable, or sometimes even negative, result. This is especially clear in the $2 < p_{T,a} < 4$ domain. On the near-side it is harder to judge the reliability of the results, but we will look at a comparison between different methods in Section 6.1.

4.6 Jet yield determination with low statistics

When both the leading and associated particle have large transverse momentum, we are entering a low statistics regime, where one or more of the bins in the fitting ranges of a set of dihadron histograms are empty. In this range a χ^2 –fit is no longer appropriate for two reasons. One of the reasons is that the difference between the estimate of the uncertainty estimate from the measured events and the uncertainty of the expected events starts to increase. Besides that a *chi*²–fit assumes normality of the probability distribution it is fitted to. This is already a strained assumption when there are fewer than about 10 counts in a bin, because the scaled Poissonian nature of the underlying distribution starts to become noticeable. Furthermore the empty bins in particular are not taken into account when performing the fit, because no error is attributed to these empty bins. This results in a significantly higher estimate of the background than would be correct. When all bins are filled, it is assumed that not too many of the bins have low (below 10 counts) statistics. This assumption is more plausible because the amount of underlying counts in the bins decreases linearly with increasing $\Delta\eta$.

In this low statistics regime, a numerical integration of the background for each individual orientation bin was attempted. For the pp–collisions this suffices, as seen in Section 4.4. However it turned out that assuming that p_2 and p_3 are equal to zero would significantly influence the jet yields in a certain domain of $p_{T,t}$ and $p_{T,a}$. Therefore the following procedure was attempted to determine the flow coefficients in the low-statistics regime.

The background determination is performed independently for in/mid/out-of-plane triggers. We use the following form

$$B(1 + p_2 \cos(2\Delta\phi) + p_3 \cos(3\Delta\phi)) \quad (4.7)$$

for the background. The p_4 coefficient is assumed to be 0. Only p_2 and p_3 components are ‘fitted’, and no underlying $v_n^{t/a}$ coefficients are determined.

Then a Fourier transform over the interval $[-\frac{\pi}{2}, \frac{\pi}{2}]$ is performed for order 0, 2 and 4. These harmonics have been chosen because they produce an inverse system of equations that does not have high numbers that have to be subtracted from each other to lead to a relatively small result. In other words: these harmonics are suitable

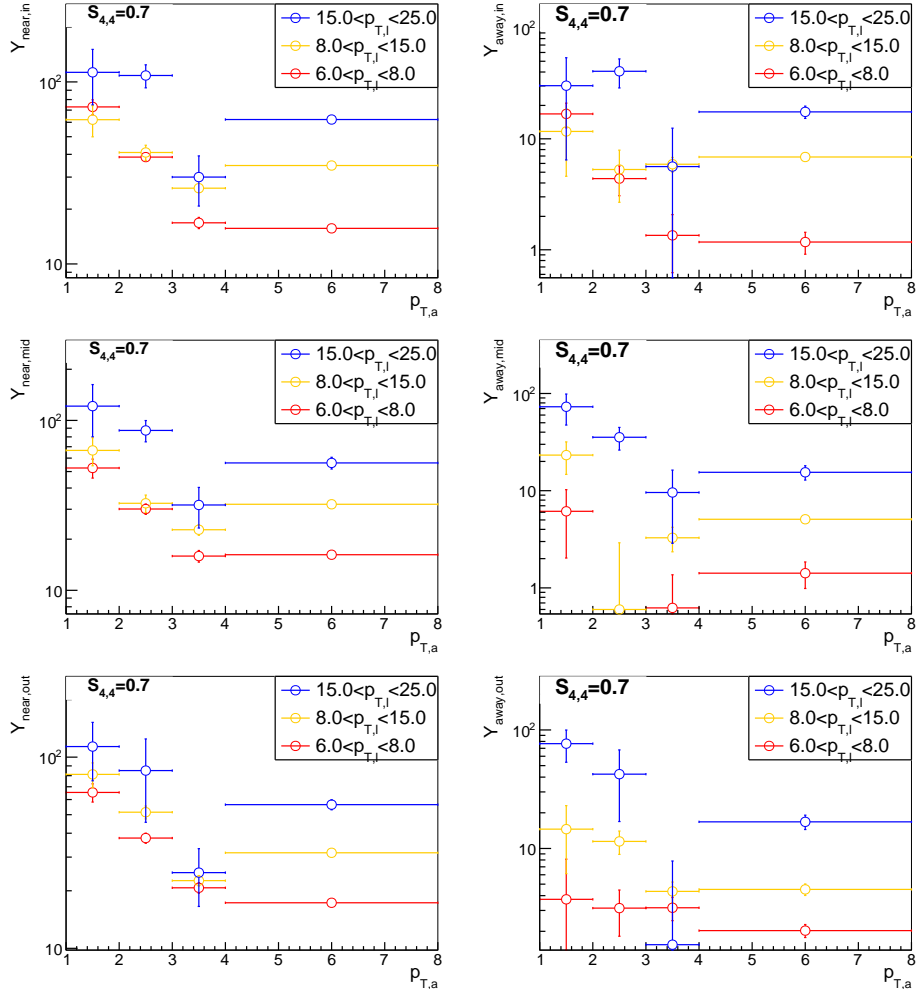


Figure 4.12: The charged jet yields from the PbPb–fits with selected triggers, from top to bottom for the in/mid/out-of-plane. When the lower value of the error bar is lower than 0, it is cut off in these log–plots. With $8 < p_{T,t} < 15$ GeV/c at $p_{T,a} > 4$ GeV/c or $15 < p_{T,t} < 25$ GeV/c at $p_{T,a} > 3$ GeV/c a Fourier analysis is used.

for determining the relevant parameters. However the rapid oscillations in $\cos(4\Delta\phi)$ are harder to fit with a histogram with a finite bin-width in $\Delta\phi$. This could introduce a bias in the results. Performing the Fourier transform results in the following set of equations:

$$\begin{pmatrix} f_0 \\ f_2 \\ f_4 \end{pmatrix} = \begin{bmatrix} \pi & 0 & -2/3 \\ 0 & \pi/2 & 6/5 \\ 0 & 0 & 6/7 \end{bmatrix} \begin{pmatrix} B \\ Bp_2 \\ Bp_3 \end{pmatrix}, \quad (4.8)$$

with f_n the n 'th order Fourier transform. This system can be inverted to find the following set of equations

$$B = \frac{9f_0 + 7f_4}{9\pi} \quad (4.9)$$

$$p_2 = \frac{10f_2 - 14f_4}{5\pi B} \quad (4.10)$$

$$p_3 = \frac{7f_4}{6B} \quad (4.11)$$

No effort is spent to proper propagation of the errors, since these are computed in the bootstrap procedure. A more rudimentary approach was attempted first by integrating only a small number of bins in the range, and reverse that to find a cosine that would hit those points. Unfortunately this turned out to be too unstable, due to the fluctuations within those small areas.

Given this background model, the regular procedure for determining the yield from Section 4.5.4 is used.

4.7 Jet yield determination in PbPb, without trigger selection

In order to compare the jet yield with a baseline measurement, a jet yield measurement without selection on the orientation of the trigger particle has been performed as well. First we will discuss the method the background is determined. After that the method of the jet yield measurement is discussed.

4.7.1 Determining background

For the analysis without trigger selection the same background model has been used as for the low statistics regime which has been described in Section 4.6.² Figure 4.13 shows some examples of the background fit, and a full overview can be found in the appendix, Figure A.2. Even though the near side background is rather well described with this model, the away side background shows that the p_3 coefficient as found by the fit seems to be too large in some of the bins. This effect could be due

²This is not the best choice to subtract the background, though the assumption that $p_4 = 0$ is less problematic in the analysis without trigger selection than in the same momentum ranges in the study with selected triggers. The main reason to not introduce yet another background model here for the high statistics domain has to do with time constraints.

to the assumption that $p_4 = 0$. Lower $p_{T,t}$ have been studied, yet unfortunately the contribution of p_4 is too significant there to perform a high quality determination of the background, as can be seen in Figure 4.14. Attempts with computing higher order Fourier-components have not been fruitful even in the high statistics domain. The results are not precise enough due to the fact that the Fourier components are computed on a binned histogram, and the generalisation of Equation 4.8 becomes unstable under inversion.

Figure 4.15 shows the effective flow parameters $p_{2/3}$ as a function of $p_{T,a}$. The results are quite stable for lower $p_{T,t}$, but for high $p_{T,t}$ the uncertainty becomes large. It is important to remember that the effect of this uncertainty on the jet yield is damped by the overall background level. And therefore the near-side jet yield can still be determined with reasonable uncertainties.

4.7.2 Determining charged jet yield

The same procedure that is performed on any of the orientation bins explained in Section 4.5.4, is also performed to determine the jet yield in the case without a trigger selected on orientation. Figure 4.16 shows the jet yields. These are used to create the further results in Section 6.1.

4.8 Quality of the background fit

As first observed in Figure 4.5 there is a certain tension within the background fit. We start with a discussion on that tension. Afterwards a pp-jet is inserted in the PbPb background in order to visually inspect how large the difference between the signal and background might be around the away-side. Then we conclude with a consistency check between the simultaneous background fit and the Fourier analysis.

4.9 Systematic uncertainties

There are several sources of systematic uncertainty. We can divide them into three groups.

1. The method for subtracting the background
2. The tracking efficiency and cuts
3. The event selections

Here a discussion will be held on the uncertainty due to the latter two points. The first point will be discussed qualitatively in Section 4.9.2, and quantitatively in sections 6.1.2 and 6.2.2.

4.9.1 Uncertainty due to event and track cuts

To get an idea of the typical size of systematic error associated with event level cuts, we can look at Section 3.3.1. From there it can be concluded that the resolution of

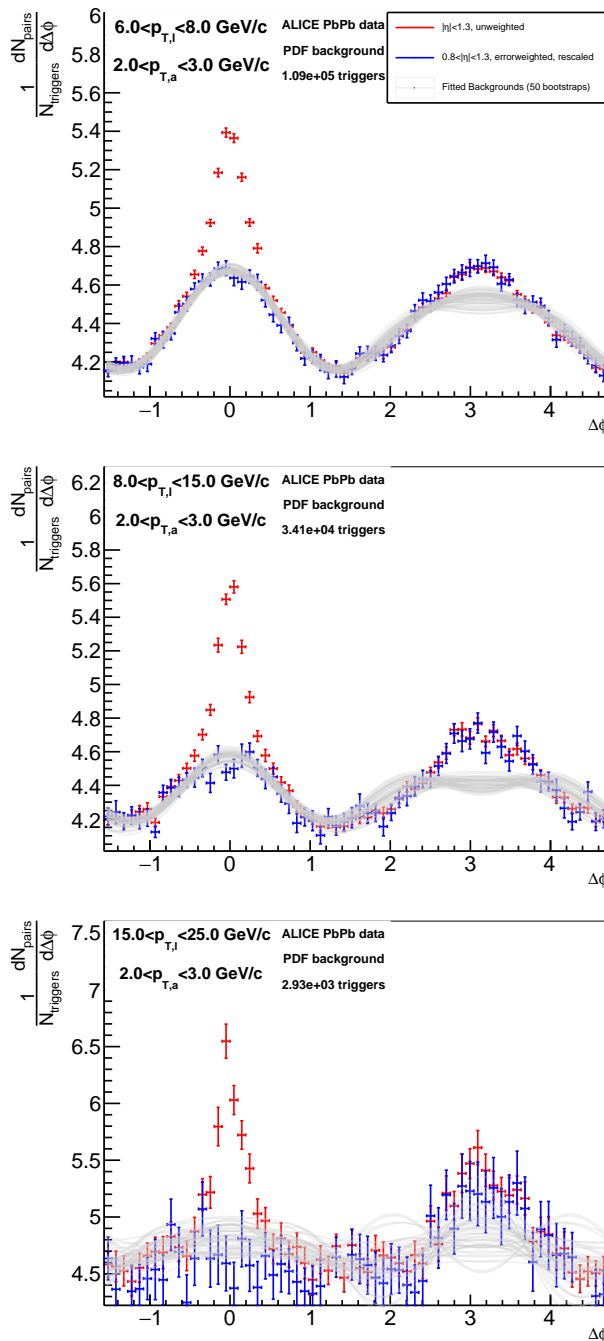


Figure 4.13: The $\Delta\phi$ -projections of the PbPb-data for several p_T -ranges. See Figure A.2 for the rest of the fits. The colours represent projections of the data over different η -ranges. The light grey lines indicated a fit of the background in 50 different bootstrap samplings to illustrate the uncertainty of the background estimate.

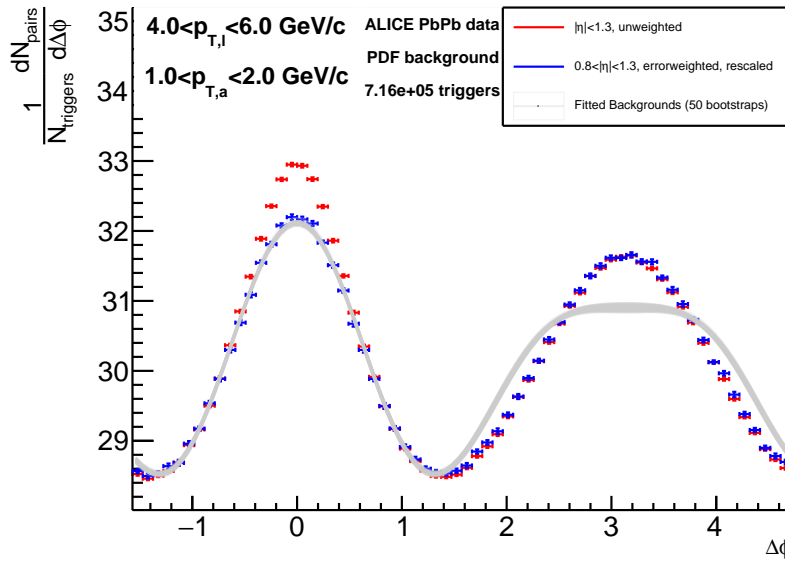


Figure 4.14: The $\Delta\phi$ –projections of the PbPb–data in the lower $4 < p_{T,t} < 6$ GeV/c range, where the away-side shape is not well described.

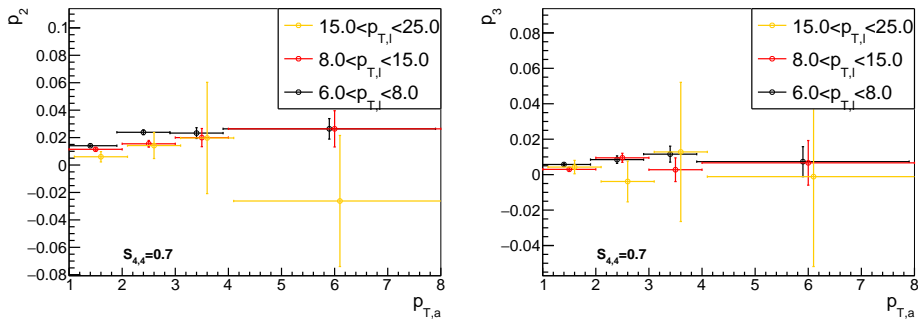


Figure 4.15: The effective flow components from the fits on the PbPb–data without trigger selection. For both p_2 and p_4 the $6 < p_{T,t} < 8$ GeV/c result is hidden below/on top of the near identical $8 < p_{T,t} < 15$ GeV/c result for the $4 < p_{T,a} < 8$ GeV/c bin. With $8 < p_{T,t} < 15$ GeV/c at $p_{T,a} > 4$ GeV/c or $15 < p_{T,t} < 25$ GeV/c at $p_{T,a} > 3$ GeV/c a Fourier analysis is used. Orange and black plots slightly displaced for visibility.

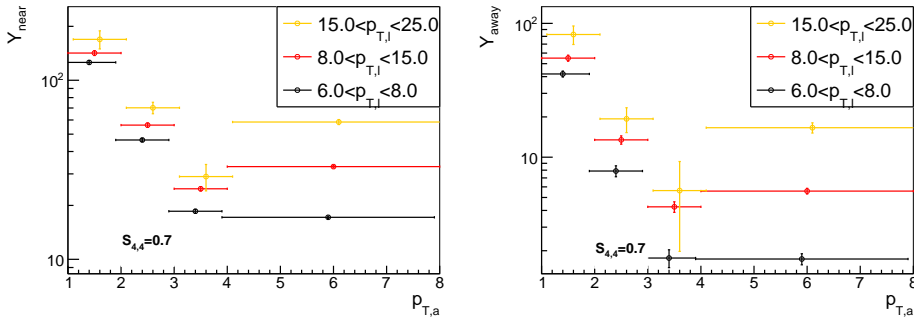


Figure 4.16: The charged jet yields for the near side (left) and away side (right) peak from the fits of the PbPb-data without trigger selection. With $8 < p_{T,t} < 15$ GeV/c at $p_{T,a} > 4$ GeV/c or $15 < p_{T,t} < 25$ GeV/c at $p_{T,a} > 3$ GeV/c a Fourier analysis is used. Orange and black plots slightly displaced for visibility.

centrality determination of the events by the V0 is about 1% at most. Since the I_{AA} changes by less than one unit over the full centrality range the expected uncertainty in I_{AA} is less than 1%.

In [75] the total uncertainty on the tracking efficiency for the track selection used in this work was estimated to be around 4%.

A complete study of the systematic uncertainties on the near side yield using the LDE-method has been performed in [48] for the I_{AA} , and therefor it was chosen to not repeat that here. In that study a total systematic uncertainty of about 7% was found on the near-side I_{AA} .

4.9.2 Tension within the background fit

Figure 4.5 revealed that there is some tension within the background fit. Especially in the mid-plane the background around the near-side, the fit overshoots the background, as if the $p_{2,mid}$ is too high. Note that the in- and out-of-plane histograms have an amplitude that is around 6 times larger than the mid-plane histograms in the case of Figure 4.5. Therefor the difference between the fit and the data will on average will be larger in these orientation bins. The pull these bins will exert on a χ^2 -fit is considerably larger since the relative errors are similar. This means that the mid-plane p_2 is largely determined by the measured flow in the in- and out-of-plane orientation bin.

Figure 4.17 illustrates the p_T -dependence of these differences between the fit and the data. Here the fits from Figure 4.5 (on the left) are compared to a higher $p_{T,a}$ -bin (on the right). It shows that this problem decreases, but does not fully vanish at higher $p_{T,a}$. In addition, the signal/background ratio increases rapidly, which means that the influence of this difference on the jet yield decreases as well. At higher p_T it is also better visible that the tension in the background around the near-side peaks is also present in the in- and the out-of-plane histograms: the fitted background (grey lines)

are too high for both the in-plane and the out-of-plane bin results with respect to the large delta η background (blue data points). Apparently the background fit can not match the amplitude of the second-harmonic flow signal in-plane and out-of-plane simultaneously, and the final result is a compromise.

4.9.3 Inserting pp-jets into PbPb-collisions

The pp peak is added to several fitted backgrounds in PbPb-collisions. This is done in several p_T -ranges to illustrate whether a jet peak with the order of magnitude of the pp-peak can be detected above the background.

In figure 4.18 several examples are given, where the PbPb-background with pp-jets (blue points) is compared with the PbPb-data (red points) and the fits of the PbPb-background (transparent grey lines). Several conclusions are:

- The near-side peak is often clearly distinguishable from the background, with an I_{AA} of about 1. This holds true for the in-plane bin as well, where the shape of the jet peak is hard to distinguish visually from the shape of the background.
- It is important to keep in mind that the pp-peak is added to the result of a model, and therefore could very well be too high. The mid-plane results with $6 < p_{T,t} < 8$ GeV/c and $2 < p_{T,a} < 3$ GeV/c and $3 < p_{T,a} < 4$ GeV/c seem to give a clear example of this: at the away-side, the background is roughly equal to the PbPb-data, though the pp-peak is clearly larger. This should not be the case unless the $I_{AA} \approx 0$, which does not seem to be the case in the in-plane bin and the out-of-plane bin. This also shows that distinguishing the away-side peak from flow background in these p_T -bins is very difficult.
- In the top left panel, the PbPb background without trigger selection, has red PbPb-data points around the away-side peak that are higher than the blue background plus inserted pp-signal. This would mean that $I_{AA} > 1$ for the away-side and/or that the away-side peak is narrower in PbPb-collisions than pp-collisions. This has not been seen in other measurements and is also not expected on general ground: interactions with the QGP are expected to lead to a broader peak. It is therefore likely that the background estimate is incorrect in this bin.
- In the meanwhile for those bins the in- and out-of-plane bins show that the away side peaks are very small with respect to the large flow contributions. On the higher end with the $8 < p_{T,t} < 15$ GeV/c and $3 < p_{T,a} < 4$ GeV/c bin, the uncertainty on the background determination via the Fourier-analysis is very large, leading a fairly high variance in the resulting I_{AA} .
- At the higher $p_{T,a}$ -bins there is not enough data to establish a p_3 . There are some significant outliers between the fits in the bottom row of Figure 4.18, that indicate the value is the result of overfitting in some unfortunate bootstraps. The choice was made to still include a p_3 contribution in these cases to give a reasonable estimate of the error on the background determination, since there

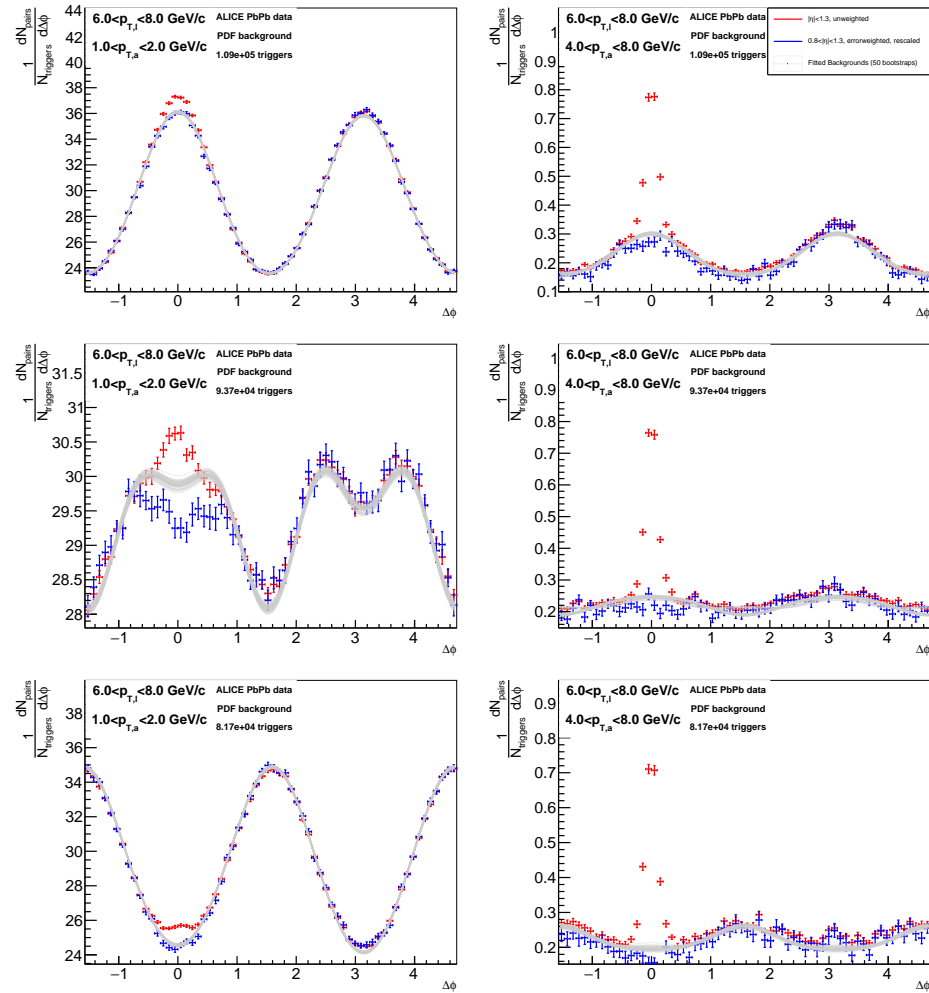


Figure 4.17: The $\Delta\phi$ -projections for the $1 < p_{T,a} < 2$ GeV/c bin (left) that was previously shown in Figure 4.5 and the $6 < p_{T,t} < 8$ GeV/c and $4 < p_{T,a} < 8$ GeV/c bin (right). In both cases $S_{4,4}$ is 0.7. From top to bottom the dihadron correlations with in-, mid- and out-of-plane triggers.

is still a significant p_3 as one can see in the bottom right and bottom center panels of Figure 4.18.

4.9.4 Quantifying difference between fit methods

It is possible to use the results from the simultaneous ‘plane dependent fit’ (PDF method) to find a background for the data without trigger selection as a consistency check. It can also be used an alternative method for when the Fourier method does not suffice. And this might be the more prudent approach since this Fourier method was specifically designed for the high p_T domain where the background was not as dominant, and p_4 was negligible. Equation 1.13 indicates what the proper p_n is based on the resulting variables $v_n^{t/a}$ of the PDF method. This was calculated and afterwards compared to the p_n found in the study without trigger selection. The difference between these two gives an indication of the differences between the methods.

In Figure 4.19 the differences in the resulting flow are shown. For p_2 seems to be overestimated by the model on average, specifically in the $3 < p_{T,a} < 4$ GeV/c bin. It is clear that p_3 is identical within uncertainties in both methods, while the PDF method finds a positive p_4 when the $p_{T,a}$ starts to increase.

In Section 7.3 we will discuss possible origins of these differences.

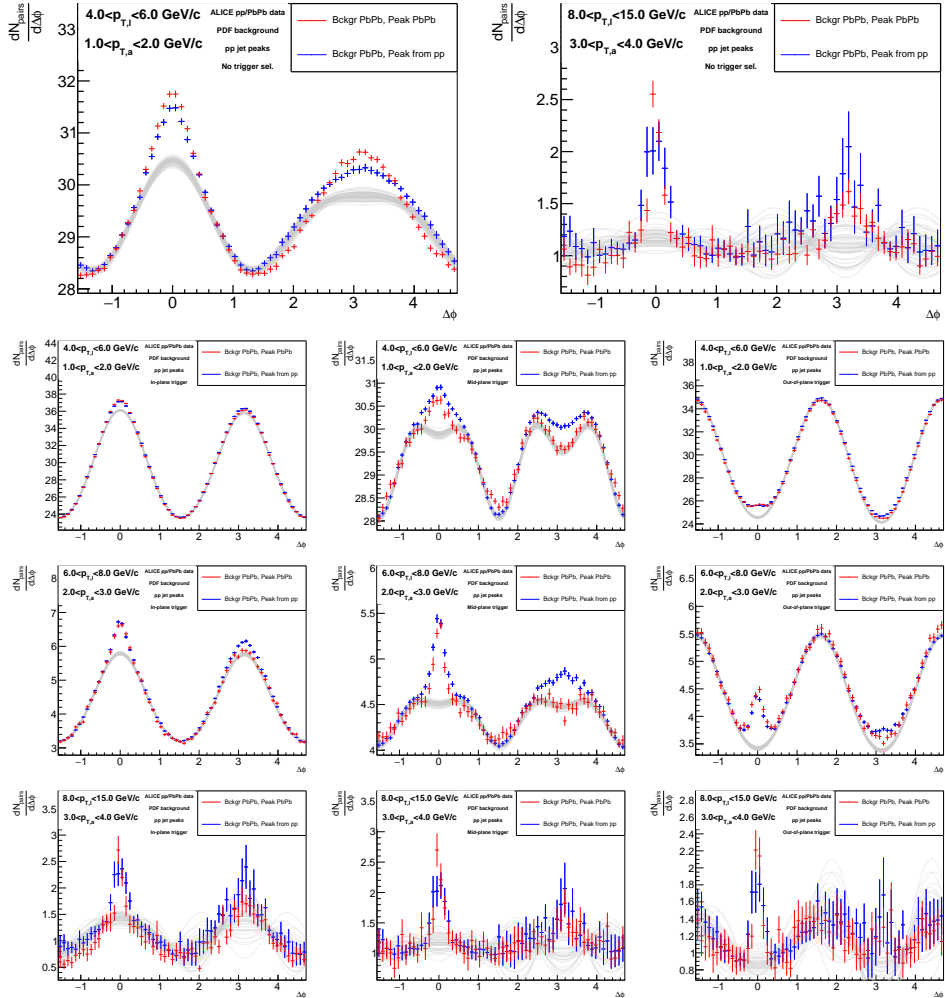


Figure 4.18: The ALICE PbPb data (red points) with the best fits of the 50 bootstrap iterations (grey lines) and that background with the added pp signal (after subtracting its background) for a selection of p_T -bins and plane-bins. This gives an indication of the order of magnitude of the expected signal with respect to the PbPb background. The bottom row has been performed with the Fourier analysis.

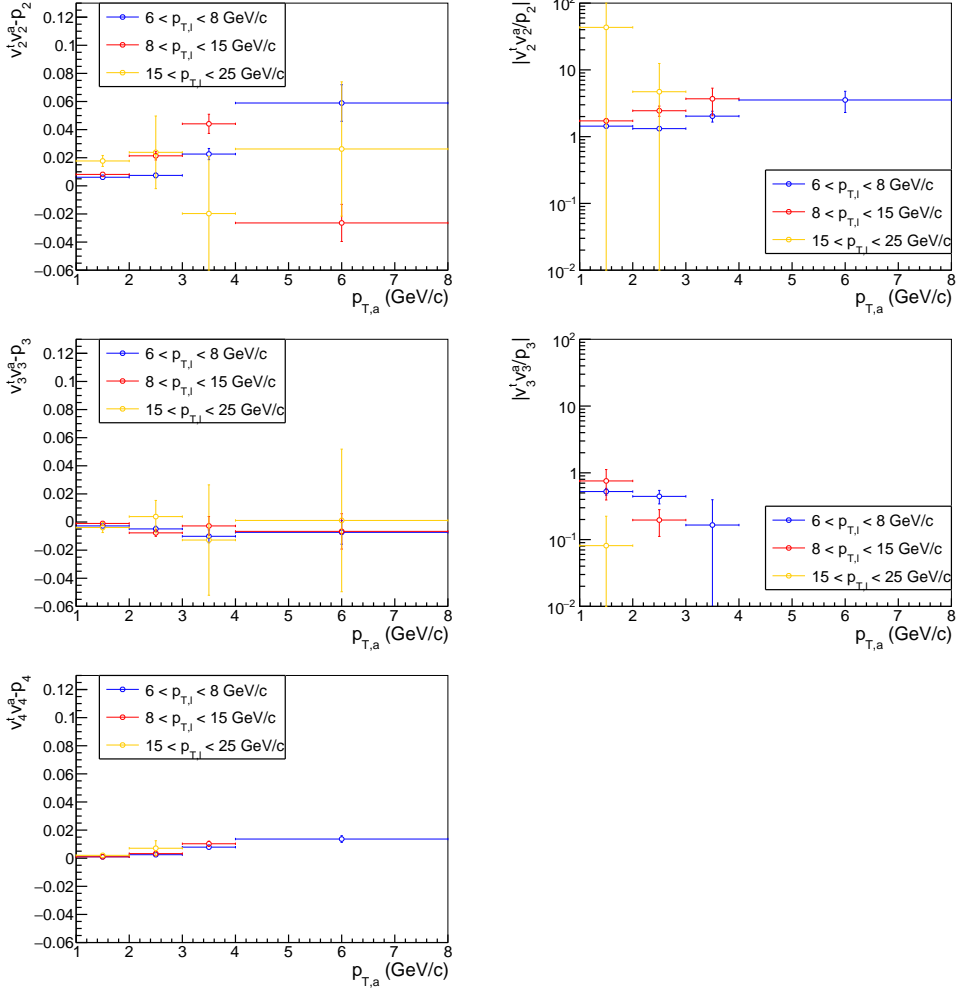


Figure 4.19: The differences (left) and ratios (right) in p_n as a function of $p_{T,t}$ and $p_{T,a}$ between the simultaneous background fit (PDF method) and the Fourier analysis of the data without selection on the trigger. Missing data points in p_4 are due to the fact that there was no χ^2 -fit possible in the trigger selected study. Note that p_4 is assumed to be 0 by the Fourier model, so a ratio could not be calculated. Missing points in the upper two rows are bins where the PDF method could not be applied.

Chapter 5

Analysis on Monte Carlo simulations

Additional Monte Carlo simulations have been performed in order to check whether the test the method of analysis and find an prediction from current theory for the observed quantities. If a measurable difference is present, this analysis can also help with determining what volume of experimental data is necessary to measure a difference in the jet peak between plane-bins. AMPT events were generated, and the output was analysed with the same methods as those used for the data, or the closed analogue thereof.

5.1 Generator

A Multiphase Transport (AMPT) model was used for this study to generate 4 million events. The model simulates collisions using different model approaches for different phases of the evolution of the colliding system and includes mechanisms that generate flow as well as jet quenching, which is both needed for this analysis.

The AMPT model is a Monte Carlo generator that simulates heavy-ion collisions.[56] It uses the heavy ion jet interaction generator (HIJING) model [79] to generate initial conditions, including soft string excitations¹ and minijet partons with a realistic angular and momentum distribution. In the mode used for this work (AMPT with string melting), both the exited strings and the minijets are consecutively run through Zhang's Parton Cascade (ZPC)[82], which simulates the parton transport in the QGP phase until the partons freeze out. At freeze-out quark coalescence is simulated by

¹These strings refer to the Lund string model, that model hadronization using QCD strings between two quarks that have a linear potential based on the distance between them. If the potential energy stored in the string is large enough, it can be used to create new quarks and the hadron fragments into two new ones.

taking the nearest partons and combining them into hadrons.² In the final step the rescattering of the produced hadrons in the dense hadronic environment is simulated with A Relativistic Transport (ART) model.[55]

Unlike before in Section 4.3.1, when the AMPT particles were used for efficiency calculations, the output of the AMPT model is used directly to perform the analysis on.

5.2 Similarities and differences with data

For this analysis, the code that reads events and fills the pair histograms was rewritten to directly process generator-level information, following the analysis on data as closely as possible. However the code for fitting the dihadron events is nearly identical. The following choices that can be qualified as differences have been made in this process:

- No single particle efficiency corrections

Since there is no detector, not even a virtual one, in this analysis, a single particle efficiency correction is not needed.

- Centrality determination

As a rough estimate, the impact parameter of the collision was set to the range of $6.67 - 10.55$ fm at the time. In order to do a centrality estimation in the AMPT results, some extra steps would have been necessary. These limits have been chosen on the basis of a calibration of the generated impact parameters, as can be seen in Figure 5.1. One can expect differences in the I_{AA} and the fraction $\frac{I_{AA,in}}{I_{AA,out}}$ when the centrality changes. One of the reasons is that the path length of the jet in the QGP in the away side is dependent on centrality, especially around the away-side jet. But it is unlikely that the results in this chapter would change significantly depending on this rough approximation. And cutting on the multiplicity would mean generating an abundance of events, and throwing a considerable part away. Since AMPT is quite resource-intensive, this was not a viable option.

- The accuracy of the event plane reconstruction was tracked

In the events generated by AMPT, the event plane orientation is known and therefore it is possible to know the exact values of the event plane resolution and similar quantities like R_4 and $S_{4,4}$. The differences in the angle between the reaction plane and the reconstructed event plane were tracked during event generation, and afterwards these model parameters were computed. More details on this will be discussed in Section 5.3.

The following aspects stayed ‘identical’ between both analyses, or are at least as identical as can be:

²In the other mode of the AMPT model, without string melting, only the minijets pass through ZPC. The excited strings are taken directly together with the partons resulting from the ZPC into Lund string fragmentation.[20] The reason for choosing the string fragmentation version of AMPT is that it properly describes the elliptic flow at mid rapidity.[56]

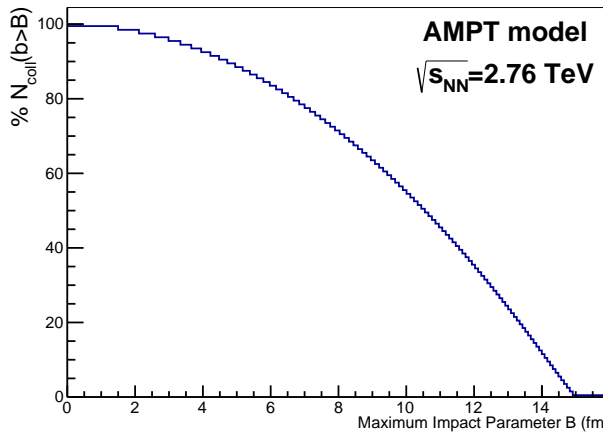


Figure 5.1: A normalised cumulative distribution of the impact parameter. Given a impact parameter on the x-axis, the y-axis yields the percentage of events that has a higher impact parameter. Results courtesy of David Dobrigkeit Chinellato.

- Event mixing

The main reason to perform event mixing in the data is to correct for non-uniform acceptance in the detector. Since in the AMPT-simulations no detector is present, at first the analysis has been tried without event mixing. Instead the triangle structure in the $\Delta\eta$ -direction, caused by the finite η -acceptance, was divided out analytically. However, it turned out that the background was not constant over $\Delta\eta$. This has a negative effect on the precision of the background fit, and therefor event mixing has been reintroduced.

- Only charged particles

The detectors of the ALICE experiment which were used in this analysis, can only detect charged particles. As such in the AMPT-simulations only the charged particles were selected for this analysis.

- Only physical primaries are accepted

Only tracks that are marked as physical primary in the AMPT-events are accepted. These tracks are those not resulting of weak decays from strange or light hadrons with a decay length of less than 1 cm.

5.3 Event plane resolution in AMPT

In the AMPT simulations, a reaction plane is available. In Figure 5.2 a distribution of the difference between the reconstructed event plane angle and the reaction plane angle is shown. Over this distribution the average of the event plane resolution-like parameter over all 4 million events can be computed to be

- $R_2 = \langle \cos 2(\Psi_2^{\text{EP}} - \Psi_2^{\text{SP}}) \rangle = 0.73715 \pm 0.00003$,
- $R_4 = \langle \cos 4(\Psi_2^{\text{EP}} - \Psi_2^{\text{SP}}) \rangle = 0.40620 \pm 0.00004$ and
- $R_8 = \langle \cos 8(\Psi_2^{\text{EP}} - \Psi_2^{\text{SP}}) \rangle = 0.07357 \pm 0.00005$.

The values for R_4 and R_8 are comparable to the results estimated based on the relation between R_2 and R_8 or R_8 in the toy Monte Carlo of Chapter 2.2.1. Subsequently these values are comparable to the ones used for the fit of the data in Section 4.5.2.

In Section 1.5.4 it is argued that no correlation is expected between the even and odd harmonic symmetry plane angles. To test whether this was the case in the Monte-Carlo, also the distribution of the $\Delta\Psi_3$ has been plotted. As expected the left side of 5.3 shows a uniform distribution, i.e. no correlation between the third and second order symmetry plane angles Ψ_3 and Ψ_2 . This results in a average $S_{3,3}$ value of $(11 \pm 5) \cdot 10^{-5}$.

Equivalently the distribution of $\Delta\Psi_4$ can be studied. The right side of Figure 5.3 shows the angle between the fourth-order symmetry plane as determined from the final state particles and the event plane $\Delta\Psi_4 = \Psi_4^{\text{RP}} - \Psi_2^{\text{SP}}$. The corresponding factors are $S_{4,4} = 0.13957 \pm 0.00005$ and $S_{8,4} = 0.02022 \pm 0.00005$. This means that these values are remarkably different than the optimal values the analysis in data as discussed in Section 4.5.2 suggests. Such a low value of $S_{4,4}$ resulted in data that there are cases in the bootstrap where a different minimum would be selected. In the ALICE data Figure 4.10 suggests that a higher $S_{4,4}$ of about 0.7 might result in a better fit, since the resulting flow coefficients are more consistent between bins. On the other hand there are two important remarks: firstly these parameters are not necessarily modelled correctly in HIJING/AMPT. Secondly the analysis on data also showed that results were remarkably robust under the change of $S_{4,4}$: as long as is was ‘large enough’, the resulting fits with different $S_{4,4}$ look more or less identical.

5.4 Differences in the fitting procedure

The same approach as for real data is used, with some minor adaptations for the case of generator-level data. The only differences is that the fit is performed with two different values of $S_{4,4}$. On the one hand $S_{4,4} = 0.7$ is used to compare with the values used in the analysis of the experiment. On the other hand $S_{4,4} = 0.1$ is used since this is close to the value found for the AMPT events in the previous section. For the final results the $S_{4,4} = 0.7$ has been chosen, since the $S_{4,4} = 0.1$ sometimes leads to a poor quality of the fit. In these cases the results revert to a non-negative p_4 even though the flat top around the the away-side peak flow suggests that there should be a negative p_4 . An example of this is shown in Figure 5.4.

5.5 Examples of the fit at low p_T

As was already visible in Figure 5.4, there is still the same tension in the fit around the near-side region on which the fit is performed; in the near-side range $\Delta\phi \in [-1, 1]$,

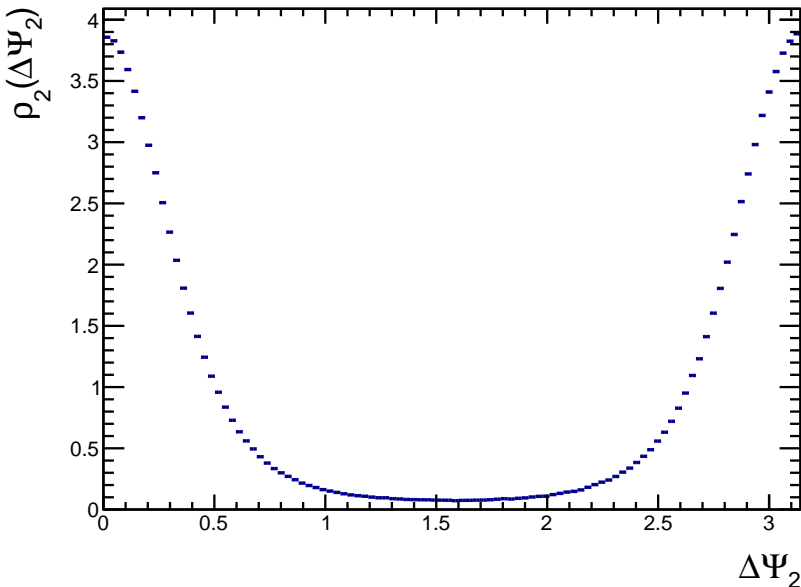


Figure 5.2: Distribution of the difference between the event plane and the reaction plane angle. Uncertainties are smaller than the marker size.

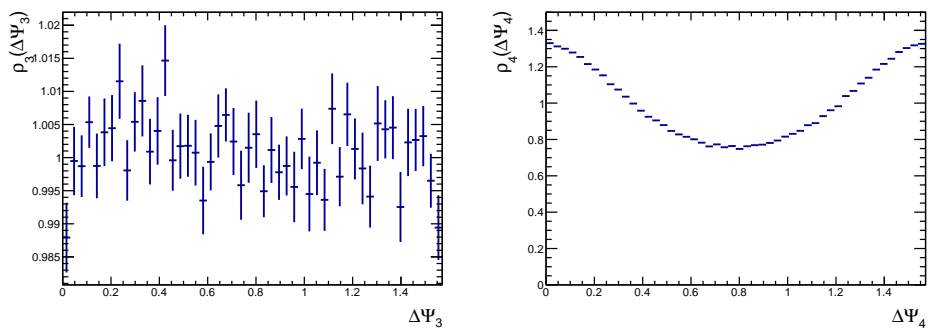


Figure 5.3: Distribution of the difference between the second harmonic event plane and the third (left panel) and fourth (right panel) harmonic event plane angle. For $\Delta\Psi_4$ the uncertainties are smaller than the corresponding markers.

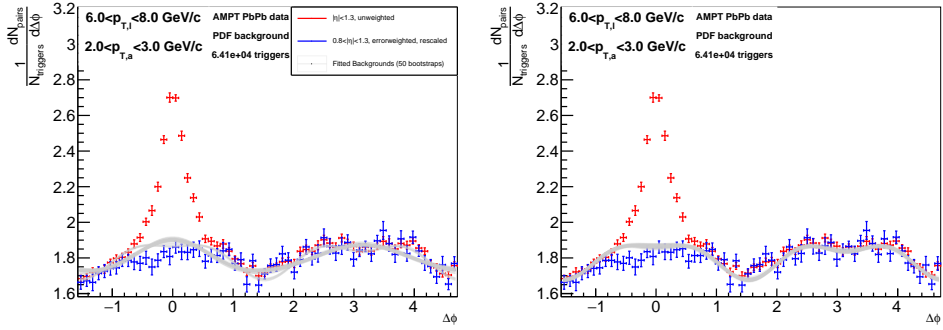


Figure 5.4: A $\Delta\phi$ –projections from the PbPb–events from the AMPT event generator for the $6 < p_{T,t} < 8$ GeV/c and $2 < p_{T,a} < 3$ GeV/c bin, when fitted with the PDF and a $S_{4,4}$ parameter of 0.1 (left) and 0.7 (right).

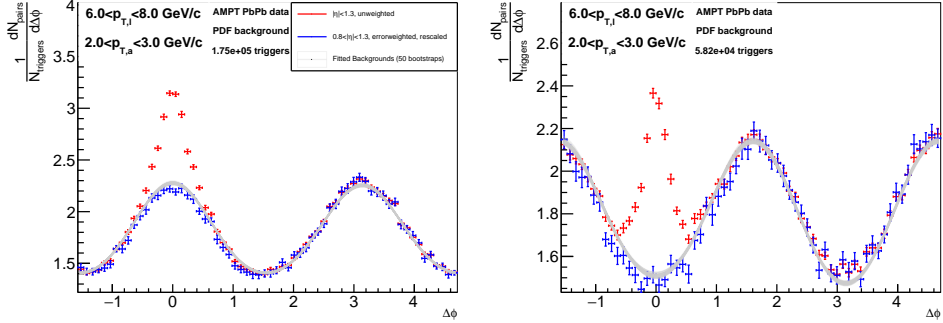


Figure 5.5: A $\Delta\phi$ –projections from the PbPb–events from the AMPT event generator for the $6 < p_{T,t} < 8$ GeV/c and $2 < p_{T,a} < 3$ GeV/c bin with in-plane triggers (left) and the out-of-plane triggers (right), when fitted with the PDF and a $S_{4,4} = 0.7$.

the fit seems to overestimate the background in a similar way to the ALICE data. This effect is seen for both the $S_{4,4} = 0.7$ case, as for the case of the $S_{4,4} = 0.1$ fits that resulted in a negative p_4 .

The tension is present in both the in-plane and the out-of-plane results, as can be seen in Figure 5.5. It is also visible in other p_T -ranges, which can be seen in the rest of the fits in the figures A.6 through A.9 in the appendix. The figure suggests that a better fit would be achieved if $p_{2,mid}$ and $p_{2,in}$ are slightly smaller, while $|p_{2,out}|$ is slightly larger. However, this cannot be accommodated by the model, since three p_2 values are determined from 2 underlying parameters, v_2^a and v_2^t , the composite values are therefore not fully independent.

This tension is not visible in the sum of the three trigger orientations, as shown in Figure 5.6, which is notable since it is the individual data sets that have been fitted.

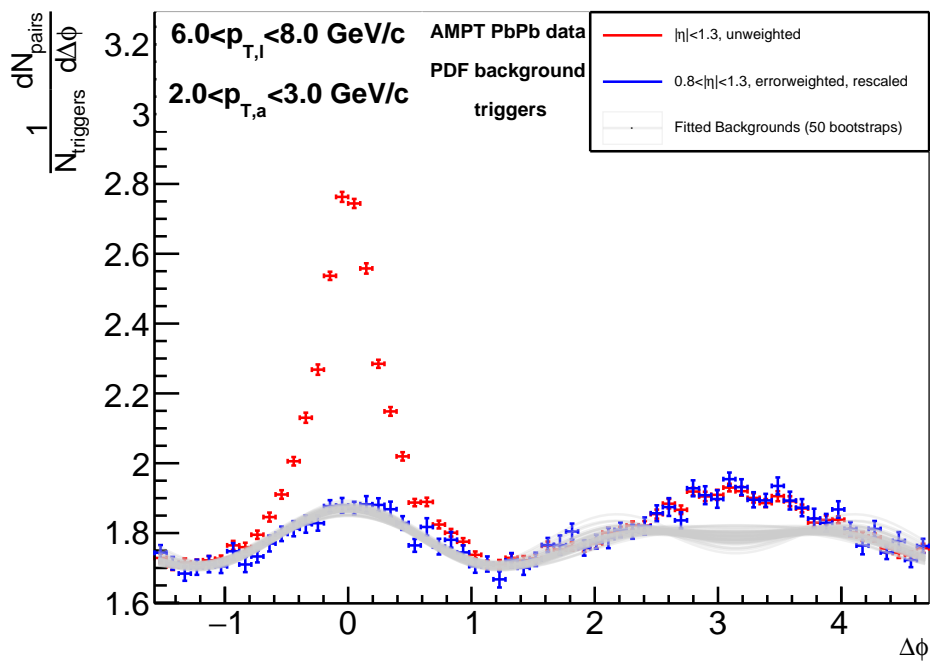


Figure 5.6: A $\Delta\phi$ -projection from the PbPb-MC-data for the $6 < p_{T,t} < 8$ GeV/c and $2 < p_{T,a} < 3$ GeV/c bin, when fitted with the PDF and a $S_{4,4} = 0.7$.

Chapter 6

Results

The main results of the studies will be presented in this chapter. It starts with a discussion of the background models for the I_{AA} . Then the results for a set newly proposed observables I_{plane} follow, together with a comparison of the different methods.

6.1 Associated yield ratio

6.1.1 Results

In Figure 6.1 a comparison is shown between the three methods used to compute the associated yield ratio I_{AA} : the ratio of per-trigger associated yields in PbPb and pp events as a function of associated particle p_T , without selection on trigger particle orientation with respect to the event plane. Statistical uncertainties have been determined by calculating the ratio per bootstrap sample and calculating the spread of the results. Systematic uncertainties will be discussed later. The orange points in Figure 6.1 show the results when the Fourier analysis as proposed in Section 4.6 is used to determine and subtract the background. The red points in Figure 6.1 show the results with a background derived from the simultaneous plane dependent trigger fit (PDF-background) as proposed in Section 4.9.4. The blue points in Figure 6.1 show the baseline comparison (only for the near side) where the background is measured at large $\Delta\eta$ ((LDE-)background). Note that the pp-denominator is common between all three results. The error bars in the PbPb-data are derived from 50 bootstraps of the data. On pp they are computed by assuming that the entries in the histogram are statistically independent, i.e. that the statistical uncertainty on the content of each bin is the square root of the number of entries.

While assembling the results, it was noticed that the $15 < p_{T,\text{t}} < 25$ GeV/c and $3 < p_{T,\text{a}} < 4$ GeV/c bin in the LDE analysis showed a large downward fluctuation. Figure 6.1 and subsequent figures using the LDE background analysis use a different integration area for that particular p_T -range in the LDE analysis. The area used

in the other p_T -ranges turned out to result in a significant downward outlier. The left side of Figure 6.3 is used to investigate this outlier. It shows the distribution of the yields determined with the bootstrap samples for the three different yield determination methods. It becomes apparent that the distribution of the near-side yield is bimodal. This is due to an outlier in the high η range that increases the measurement of the background in about half of the bootstrap samples. Figure 6.4 shows a projection on $\Delta\eta$, that shows the jet peak is contained within the $|\Delta\eta| < 0.3$ domain. If the integration range of the near-side peak is contained within this area as well, the second mode of the jet peak vanishes as the right hand of Figure 6.3 shows. Therefore the integration area for *this particular bin* has been reduced to $(\Delta\phi, \Delta\eta) \in [-\frac{0.96}{\pi}, \frac{0.96}{\pi}] \times [-0.3, 0.3]$. This new integration area is the one that was used in Figure 6.1 and 6.2. Now the result is more in line with the surrounding points.

Figure 6.2 shows that for the most stable background subtraction (LDE-method) there is no significant pattern in the $p_{T,t}$ -dependence of the I_{AA} . Additional figures with the other background methods can be found in Appendix B.

6.1.2 Comparing background subtraction methods

Unfortunately the method of background subtraction has a sizeable effect on the result. The direct comparison of the near-side I_{AA} in Figure 6.1 shows a difference ranging from 20% for the $4 < p_{T,t} < 6$ GeV/c bin (top left panel) up to 50% for the $1 < p_{T,a} < 2$ GeV/c bin (leftmost data point) with the LDE method used as a central value. The away-side difference is larger, and has the added difficulty that the most reliable LDE method is not available. On the away side only the highest two $p_{T,a}$ bins with $p_{T,t} > 8$ GeV/c have a systematic uncertainty below 20%. The large difference between the results for different methods signals that there is a significant systematic uncertainty in the determination of the away-side yields. This is consistent with the questions allready raised in section 4.9.2 and 4.9.3.

One of the known systematic uncertainties is related to our limited knowledge of the correlations between the fourth harmonic event plane orientation and the reaction plane orientation. Figure 4.9 shows that the variations in $S_{4,4}$ for the PDF-background results can account for differences of less than 5% uncertainty in the associated yield. Varying the integration range for the away side peak (N.B. for the PDF method this also changes the area on which the background is determined) in Figure 6.5 results in a 5% to 10% change in the I_{AA} , except for the low $p_{T,a}$ range, where the Fourier approach yields results that are more strongly dependent on the integration range.

This leaves the near-side I_{AA} with a $4 < p_{T,a} < 8$ GeV/c, and the away-side I_{AA} with a $4 < p_{T,a} < 8$ GeV/c and $p_{T,t} > 8$ GeV/c as a domain where the the systematic uncertainties are reasonably small.

6.1.3 Conclusion

The LDE-results are in most cases within the range between the Fourier and PDF results. The LDE-analysis is the most data-driven approach with the least risk of

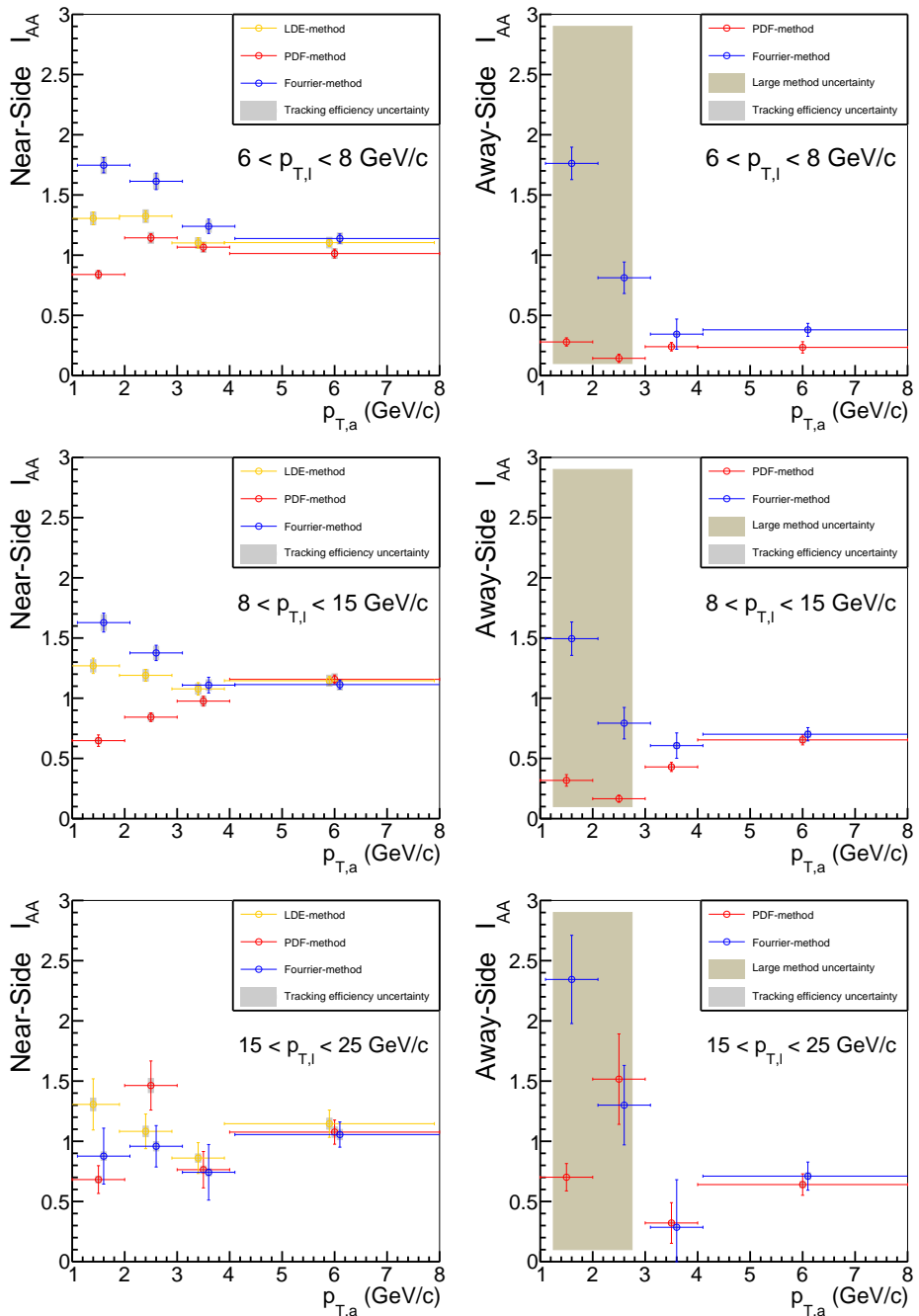


Figure 6.1: Associated yield ratios I_{AA} on the near (left panels) and away (right panels) side as a function of $p_{T,a}$ for different $p_{T,t}$ selections (one per row). Results are shown for three different background subtraction methods. For the PDF method with $8 < p_{T,t} < 15$ GeV/c at $p_{T,a} > 4$ GeV/c or $15 < p_{T,t} < 25$ GeV/c at $p_{T,a} > 3$ GeV/c a flat background is subtracted instead.

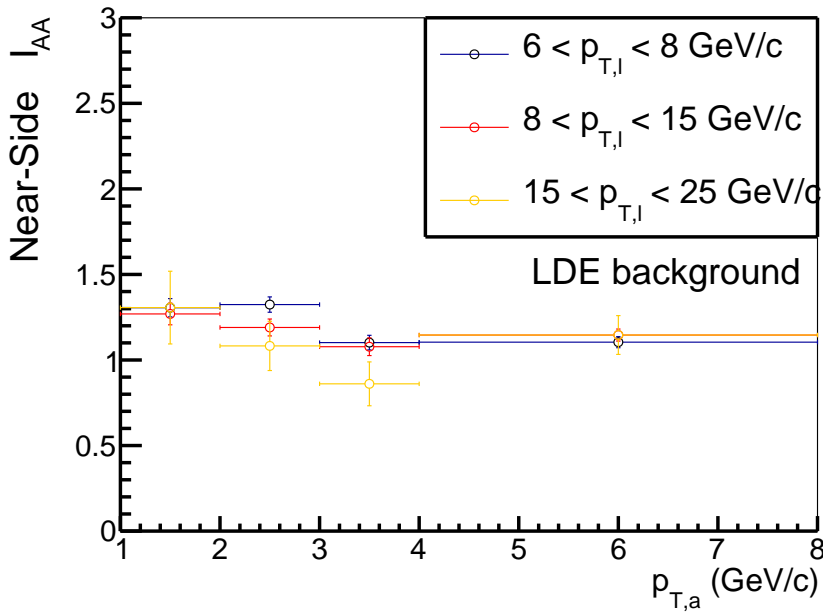


Figure 6.2: The I_{AA} for the near-side charged jet in the analysis without trigger selected. Background determined by large $\Delta\eta$ subtraction. The $15 < p_{T,t} < 25$ GeV/c and $3 < p_{T,a} < 4$ GeV/c has a different integration range then the other data points.

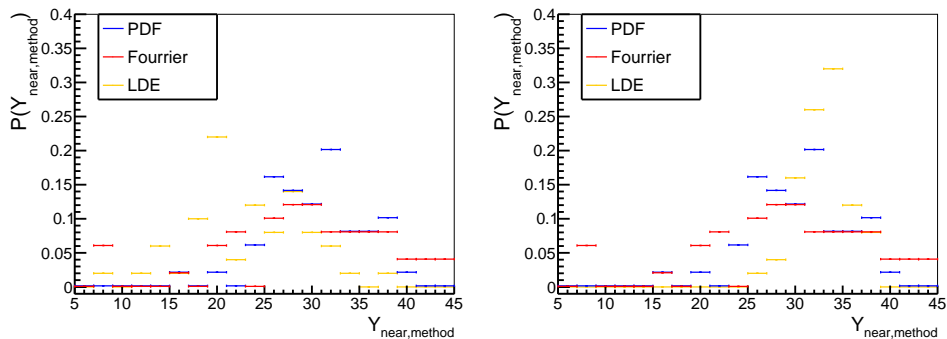


Figure 6.3: The distributions of the bootstrapped near-side associated particle yield according to different methods for the bin $15 < p_{T,t} < 25$ GeV/c and $3 < p_{T,a} < 4$ GeV/c. On the left the integration range $|\Delta\eta| < 0.8$ was used in the LDE-method, and on the right $|\Delta\eta| < 0.3$ was used.

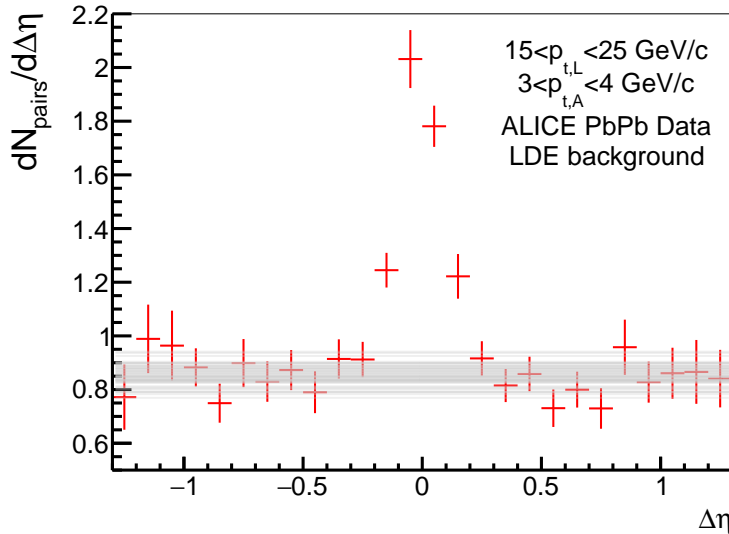


Figure 6.4: A $\Delta\eta$ -projection of the bin $15 < p_{T,t} < 25 \text{ GeV}/c$ and $3 < p_{T,a} < 4 \text{ GeV}/c$.

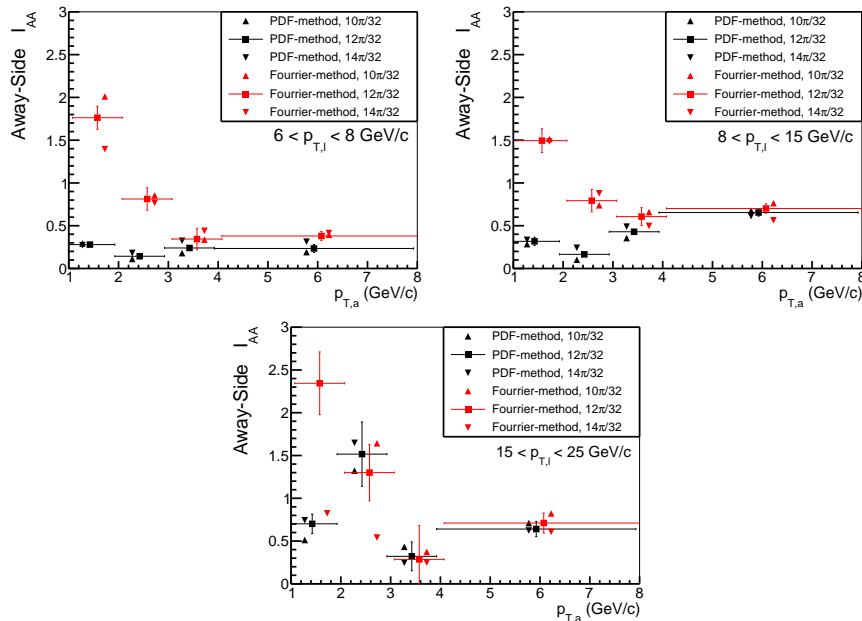


Figure 6.5: The away-side associated yield suppression ratio I_{AA} as a function of $p_{T,a}$ for several $p_{T,t}$. The integration range of away side peak has been altered by 18% to study the difference on the I_{AA} , as indicated by the triangular markers.

introducing unwanted biases. In most cases the Fourier analysis underestimates the background, while the PDF analysis overestimates it. At a $p_{T,a}$ below 3 GeV/c these differences are significant with respect to the statistical error, and therefore can be considered significant biases.

The I_{AA} for the near-side with the LDE-measurement, the baseline method, is slightly larger than 1. This trend is similar to the measurements at low z for the fragmentation functions as discussed in Section 1.4.3. That the PDF-measurement does not follow this trend indicated by multiple other experiments and a more reliable method in this experiment, is likely a sign that the PDF-fit does not fully describe the background in low p_T -ranges below 3 GeV/c.

These differences can not be explained with the uncertainties on the resolution parameters R and the correlations between the symmetry plane orientations given by the S values as Figure 4.9 shows. Nor can they be explained by varying the away-side opening angle as can be seen in Figure 6.5. We currently do not have a clear understanding of the origins of these uncertainties. Suggestions for further studies will be discussed in Section 7.3.

In the highest $p_{T,a}$ -bins, the background contribution is smaller and the results from the different methods converge to similar values. This makes these results the most reliable of this study.

The results for the away-side jet I_{AA} vary even more between methods as is shown in Figure 6.1. On the away-side, only the results for the largest two $p_{T,a}$ -bins are reliable.

6.2 Jet orientation yield ratio

6.2.1 Results

In order to study the difference between the associated yields in different orientation bins, it would be nice to be able to compare them between p_T -bins on a consistent scale. One way to do so, is by dividing through a pp reference. Yet a more direct comparison of the yields would be the jet orientation yield ratio, I_{plane} , which is defined as

$$I_{\text{plane}} = \frac{Y_{\text{plane}}}{Y}, \quad (6.1)$$

with Y_{plane} the associated charged particle yield in a certain orientation with respect to the event plane, and Y the overall jet yield in PbPb-collisions. In this analysis there are three of these quantities: I_{in} , I_{mid} and I_{out} . This quantity can be defined for both the near-side and the away-side peak. Since the trigger-weighted sum of the associated yields in three orientation bins should arrive at the dihadron histogram without trigger selection, the following identity should hold:

$$\sum_{\text{plane}} Y_{\text{near,plane}} \cdot N_{\text{plane}}^t = N^t \cdot Y_{\text{near}}, \quad (6.2)$$

where Y represents a jet yield and N^t the number of triggers over all events. This equation holds true for the away side yield as well. A corollary of this is that the weighted average of the three I_{plane} values is equal to 1 by construction. Determining the total associated particle yield Y independently and testing whether the result obeys this averaging to 1 helps to test whether the method delivers consistent results.

The results for I_{plane} as a function of both $p_{T,t}$ and $p_{T,a}$ using the baseline LDE-method of determining the yields can be found in Figure 6.6. Here both the yields with and without triggers selected on plane orientation have been determined with this method for both the 2011 ALICE data, and the generated AMPT data. It is very apparent that the three orientation bins average out to a value which is consistent to 1. It is also immediately apparent that the no significant dependence of I_{plane} on the orientation of the trigger particle with respect to the event plane is visible. There is no clear path-length dependence in the associated yield. In fact the ordering of the in- mid- and out-of-plane results changes from bin to bin, suggesting the differences are mostly due to statistical fluctuations.

As discussed in Section 1.4.3, the trigger particle selection may also result in a significant bias of the near side jet yield, both in terms of the production point (surface bias) and in terms of selecting jets with a large- z leading fragment (fragmentation bias). Both effects are expected to reduce the dependence of the near-side yields on the trigger particle orientation. A stronger impact of path length dependence is expected for the away-side yield. Figure 6.7 shows the same near-side I_{plane} values for different $p_{T,t}$ and $p_{T,a}$ selections, only this time with the numerator established by the PDF method, and the denominator derived from the yield in the plots without trigger selection with the background subtracted by the trigger and associate flow following from the PDF method. Figure 6.8 shows the same for the away-side results. Here 6.2 holds by construction. This method comes with a larger uncertainty on the results for the near-side, and they leave those conclusions unchanged. For the away-side results would not be possible with the LDE-method. Still the large uncertainties make it impossible to tell anything conclusive, especially in the experimental data.

In the cases where the trigger is plane restricted, the higher order Fourier components (and especially the p_4) become more pronounced. This makes the use of the Fourier analysis on half of the domain less reliable since it is more susceptible for higher order flow coefficients. Therefor this method has not been used in establishing the I_{plane} .

6.2.2 Comparing background subtraction methods

The identical approach was performed as for the for the I_{AA} in Section 6.1.2. Comparing Figure 6.6 and 6.7 shows that the differences between the two background subtraction methods result in a change for the near side associated yield in a range from 10% to 50%. The dependence on the integration range does nearly vanish to a sub 1% level. This is not unexpected, since the results from the analysis with selected trigger and the one without selected trigger are highly correlated, because the same underlying pair distributions are used, even when a different background subtraction technique is used.

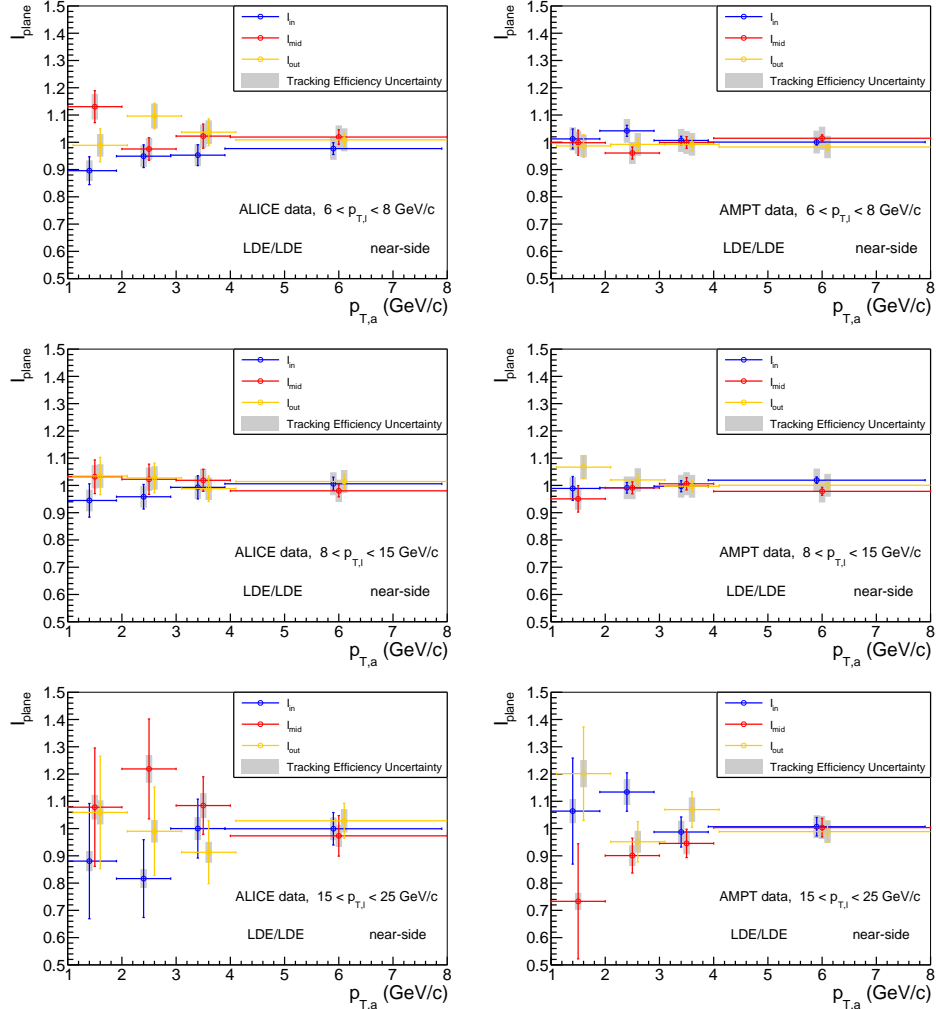


Figure 6.6: Comparison of jet orientation yield ratio I_{plane} in data when the background is subtracted using the background measured at large $\Delta\eta$ for the near-side peak for the LDE-method. The $p_{T,\text{t}}$ is increasing from top to bottom. The left contain ALICE data and the right contains the results from the AMPT event generator with a different scale on the y-axis.

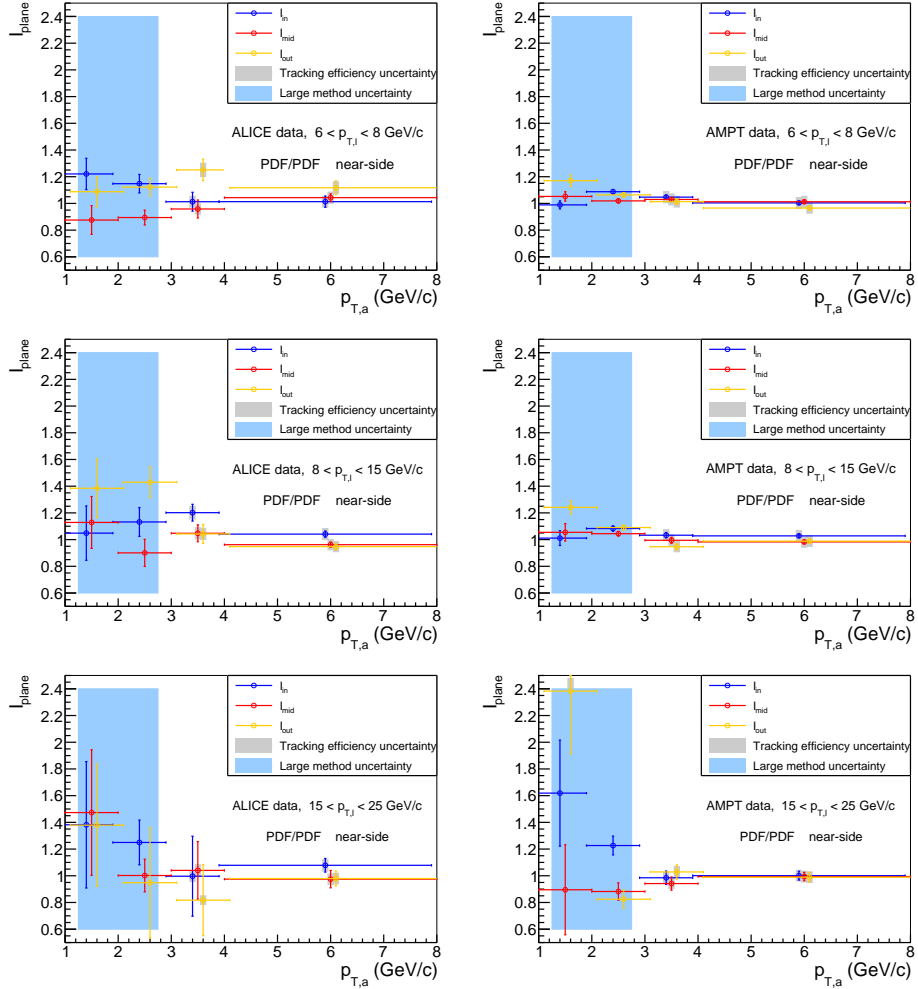


Figure 6.7: A comparison between the I_{plane} in data from the experiment for the near-side charged jet for ALICE data (left) and events from an AMPT event generator (right). All yields have been determined with the PDF method. The $p_{T,t}$ is increasing from top to bottom. For the numerator and denominator with $8 < p_{T,t} < 15 \text{ GeV/c}$ at $p_{T,a} > 4 \text{ GeV/c}$ or $15 < p_{T,t} < 25 \text{ GeV/c}$ at $p_{T,a} > 3 \text{ GeV/c}$ a Fourier analysis is used.

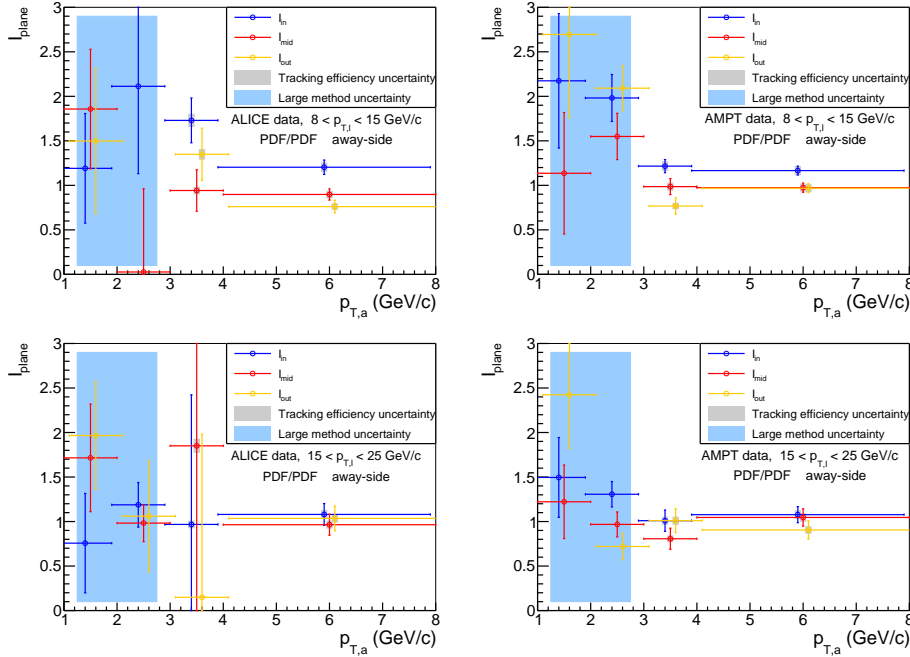


Figure 6.8: A comparison between the I_{plane} for the away-side charged jet for ALICE data (left) and for events generated by an AMPT event generator (right). All yields have been determined with the PDF method. The $p_{T,t}$ is increasing from top to bottom. For the numerator and denominator with $6 < p_{T,t} < 8$ GeV/c at $p_{T,a} > 4$ GeV/c or $8 < p_{T,t} < 15$ GeV/c at $p_{T,a} > 3$ GeV/c or $15 < p_{T,t} < 25$ GeV/c at $p_{T,a} > 2$ GeV/c a Fourier analysis is used. The statistical uncertainty on the $6 < p_{T,t} < 8$ GeV/c bin was considered to large to show the results.

Based on this comparison, we conclude that for I_{plane} , the same p_T ranges are reliable as for the I_{AA} , i.e. for the near-side I_{plane} with a $4 < p_{T,a} < 8$ GeV/c, and the away-side I_{plane} with a $4 < p_{T,a} < 8$ GeV/c and $p_{T,t} > 8$ GeV/c.

6.2.3 Conclusion

The jet orientation yield ratios I_{plane} provide a measure of the modification of associated yields that depends only on measurements in PbPb-collisions. This strongly reduces the impact of the systematic uncertainty on the tracking efficiency as well as differences in the background subtraction between pp and PbPb data which would be present when studying three trigger-selected versions of the I_{AA} .

The results from the LDE analysis in Figure 6.6 do not show significant differences between the different I_{plane} , neither in experimental data, nor in the AMPT Monte Carlo sample. The order between the three quantities varies without any pattern, and no significant dependence of the associated yield on the orientation of the trigger particle observed. The same is seen in the AMPT event generator, which suggests that the expected dependence on the trigger orientation due to path length differences is masked by other effects, such as the surface bias and the fragmentation bias. Since the uncertainties in the generated AMPT sample are similar to or smaller than those in the measurement, we conclude that the expected effect in AMPT is too small to measure with the current data sample. It would also be interesting to repeat this measurement in other event generators.

Something that might have explained the tension between the data and the PDF-fit, is that the variations of parameters such as the flow components over the width of the p_T -bins influences the end result. This is possible in particular if several quantities are correlated amongst each other. In order to rule out this possibility, the analysis has been performed with significantly larger bins once in $p_{T,a}$ and once in $p_{T,t}$. The new $4 < p_{T,t} < 25$ GeV/c bins (plural, for all $p_{T,a}$ bins) were then compared to the statistically dominant $4 < p_{T,t} < 6$ GeV/c bins of corresponding $p_{T,a}$. And similarly the $1 < p_{T,a} < 8$ GeV/c bins were compared to the $1 < p_{T,a} < 2$ GeV/c bins. Though there of course were differences in the height of the peak with respect to the background, the shape of the background and its corresponding fit were largely identical. The tension in the quality of the background fit, such as the high background around $\Delta\phi = 0$ and $\Delta\phi = \pm\frac{\pi}{2}$, did not worsen in this case. Therefor it is likely that using smaller p_T -bins will not solve the problems in the quality of the fit in for instance figure 4.5.

Chapter 7

Conclusion and outlook

Before turning to suggestions for future research, we will briefly summarise the main findings.

7.1 Summarised conclusions

For the associated yield ratio we found the following results. The results using large $\Delta\eta$ -subtraction are mostly in between the results using a background established with a Fourier analysis or with the extension of the simultaneous fit of the bins with a differently orientated trigger. The differences between these methods are significant with respect to the statistical error. These differences can not be explained by looking at the variation due to the R/S -parameters or a varying away-side opening angle. The highest $p_{T,a}$ -bin does converge towards consistent results. Due to significant differences in the away-side I_{AA} between methods it is hard to recommend trusting these results for any other range than the highest two $p_{T,a}$ -bins.

For the jet orientation yield ratio I_{plane} , the fraction of the associated yield of a trigger selected on its orientation to the event plane divided through the associated yield of all trigger particles, we concluded the following. Neither the experimental data nor the Monte Carlo sample show a path length effect in jets depending on their angle to the reaction plane. I_{plane} is a quantity which is quite robust to detector effects and analysis choices.

7.2 Prospects with larger data samples

The statistical precision of the near-side associated yield measurement, is current around 10 to up to a couple of percent, while it is much lower for the away-side yield. Collecting and analysing larger data samples has a clear potential to improve the precision. In the high p_T -domain, when $p_{T,a} > 4 \text{ GeV}/c$ or $p_{T,t} > 15 \text{ GeV}/c$, the signal to background ratio is high. Here the analysis is not limited by our

understanding of the shape of the background, and additional statistics would have additional value. However, since the amount of energy lost is not expected to depend strongly on the momentum of the propagating parton, the relative changes of the associated yield are expected to be smaller at larger momentum. This suggests that I_{AA} would move toward 1 for large enough values of $p_{T,a}$, and significantly more precision might be necessary to measure the difference between jet orientation yield ratios.

At lower $p_{T,a}$, additional statistics can help with the measurement of the near-side I_{AA} and I_{plane} with the LDE-method. For the away-side, where the path length differences are expected to be more pronounced, a better understanding of the background is required. In the 2011 ALICE PbPb data, there is already enough precision to study this.

7.3 Possible explanations of the differences between background models

7.3.1 Fourier-analysis

The Fourier-analysis proposed in section 4.6 was limited in the number of harmonics that could be added due to issues with stability of the results. However upon closer study it became clear that the Fourier-analysis up to the third harmonic includes a systematic bias dependent on the fourth harmonic. This bias can be seen in the differences between its results and those of the LDE-method on the near-side peak at low p_T in Figure 6.1, from which we can conclude that the background at $(\Delta\eta, \Delta\phi) = (0, 0)$ is underestimated by the Fourier-analysis.

The Fourier-analysis only includes flow components up to the 3rd harmonic, and because the analysis can only be performed on the half-circle the orthogonality of the components breaks down. This means that higher harmonic flow coefficient in the mix into the measured value of the lower harmonics. If Equation 4.7 is extended with one additional harmonic, it can be shown that

$$p_3 = \frac{7}{6B} f_4 - \frac{7\pi}{12} p_4. \quad (7.1)$$

For the bin with $6 < p_{T,t} < 8$ GeV/c and $1 < p_{T,a} < 2$ GeV/c used in figures 4.6 through 4.8 this would result in a correction of approximately $0.014|-0.014|0.008$ on 0.003 for in|mid|out-of-plane respectively. This shows that this approach is not suitable at low p_T , in particular in the analysis with selected trigger, where the fraction $\frac{p_4}{p_3}$ is higher than in the case without a selected trigger.

One direction that should be explored to maintain sensitivity when using a Fourier transform with higher harmonics is the use of an unbinned Fourier transform. This decreases the fluctuations due to binning effects, and opens up the possibility to perform this analysis to a higher order, including f_6 , and by extension a p_4 .

7.3.2 Simultaneous fit method

The tensions visible in Figure 4.5 between the background and the fit with the PDF-method might be due to the long tails of the jet peak disturbing the measurement of the background.¹ On a visual inspection in the pp–events from Figure A.1 this seems not to be the case: the away-side peak never falls inside $|\Delta\phi| < \frac{\pi}{2}$, and the fit has been tested up to this range. However in PbPb the jet peak might broaden due to the quenching, and therefor this test might not be enough. On the near-side, a Fourier analysis seems to perfectly cover the area $|\Delta\phi| < \frac{\pi}{2}$ in the large $\Delta\eta$ –range, so it seems likely that there are no non-harmonic elements there. For the away-side peak it is difficult to establish the width of the peak in many p_T –bins. However the effective flow does not depend strongly on the excluded area of the fit, and the excluded area has been chosen quite large to begin with. It seems that in the Monte-Carlo simulations the entire away-side peak is ‘absorbed’ into the background. This could indicate that an extensive broadening of the peak might indeed a structural problem. If this were the case, it would unfortunately mean that it is very hard or even impossible to solve.

7.3.3 Background model extensions

The difference between the fits resulting from the PDF-model and the background are especially clear in the low momentum range. The most likely causes have been studied: variations in several background parameters, like the S and R parameters, and variations in the area assumed to have no jet signal. This might be an indication that the model used in the fit does not have that the model does not take into account all effects that determine the background distribution. Possible extensions can be sought in several directions. The easiest suggestion would be to incorporate higher flow harmonics. Fitting with the 5th or higher harmonics might seem excessive, but it is important to realise that the p_2 component is suppressed when the trigger is in the mid-plane orientation, so higher harmonics are more prominent. Incorporating higher harmonics comes in two variations: it is possible to take into account the effect of higher flow harmonics v_m ($m > 4$) on the p_n ($n \leq 4$) that have already been studied, as well as incorporating additional higher harmonic terms p_n ($n > 4$) in the background model. Both can influence the established p_n in this work, even though one would expect the correlation between the higher harmonic event planes and Ψ_2 to decrease rapidly.²

In Section 1.5.4 it was assumed that only the second order event plane is correlated to other event planes. This underlies Equation 1.23, which reduces the number of correlation coefficients in the model compared to the more general formulation in [63]. It would be useful to explore these contribution more systematically, even if adding more free parameters to the model requires care. When more degrees of freedom are added to the fit, it will likely be necessary to also increase the number

¹During writing of this work no other research was found where a similar conclusions was discussed. However the effect could be worse in the present study due to the fact that relatively low p_T triggers were used here.

²[42] indicates for instance that the correlation between Ψ_6 and Ψ_2 is about 10 times smaller than the one between Ψ_4 and Ψ_2 .

of constraints, for example by increasing the number of bins for the orientation of the trigger particle. The STAR collaboration, for instance, has experience with dividing the azimuthal space into 6 areas, though in that work no p_3 was used and full correlation between event planes was assumed.[16] This has later been revisited in [15] with the 6 bins and triangular flow, but the underlying relations between the bins was not taken into account. Similarly in [46] only ‘the terms which are able to be reconstructed experimentally are included’. This notably leads to slightly different included quantities in Equation (3.14) in reference [46], such as an R_6 term, but not a R_8 term.

Another source of background correlations would be jet-flow correlations. The background model used in this thesis only takes into account pairs of particles that both follow the same angular distribution, with the same underlying symmetry planes and flow coefficients. Conversely only pairs of hadrons that are both in a di-jet system should correlate in order to produce the jet signal. However, it could be that there are two types of triggers particles: those that correlate with the flow v_n^{flow} and those that correlate with a jet v_n^{jet} , especially at low $p_{T,t}$. If flow coefficient for the background and the jets are not equal to each other this might cause mixed terms. The challenge in compensating for this phenomenon is that the size of the jet-flow contribution to the background is dependent on a) the size of the jet signal, b) jet flow, and c) possible plane dependence on jet quenching. Problem a would constitute a minor technical problem. Problem b could be alleviated by using other measurements of this phenomenon. It might be possible to come up with a theoretical model that incorporates two types of associated particles: some that correlate directly with the jet/trigger direction, and others that are correlated to the event plane orientation. But problem c is precisely the objective of this study, and would therefore be really hard to incorporate correctly.

Another interesting extension of the work is to select trigger particles based on their angles with respect to higher order symmetry planes. The PHENIX experiment has performed a study with triggers separated based on their angle with the third order event plane, but without using a fit that takes into account the underlying correlations between the symmetry planes.[13] Even though the third harmonic modulation of I_{AA} is expected to be smaller than the second harmonic studied in the present work, this exploration does help the understanding of these interactions. Together with work like [42] it might give some insight whether the assumptions on correlations between event planes hold.

In [46] a similar analysis was performed for the 2015 ALICE run 2 and the 2011 run 1 data. One of the crucial differences was that first a jet finder was run, and only charged jets with a $20 < p_T < 40$ GeV/c were selected. In this case, the background is mainly due to jet-background correlations, and the v_2^t can be interpreted as a v_2^{jet} . This leads to a significantly higher signal to background ratio, which sidesteps several challenges in this analysis. In [46] it is for instance claimed that ‘ $v_3^a v_3^{\text{jet}}$ is approximately zero because v_3^{jet} does not correlate with the second event plane’. This approximation might suffice at high signal to background ratio, but Figure 4.15 shows clearly that $p_3 > 0$ in the low momentum regime that we are interested in.

Studying correlations between high-energy direct photons and hadrons may offer similar advantages, since photons from hard scattering have a nuclear modification factor of approximately 1. [34, 57, 71] This indicates that they are likely not subject to flow. This would have simplifying consequences for the background model, since only some event-plane resolution related terms will remain. Due to the limited coverage of the electromagnetic calorimeter (EMCal) in the ALICE detector, we would not have enough statistics to do such an analysis.

In the long term it would be interesting to strive for a simultaneous fit of all p_T -bins where the underlying $v_n(p_{T,a}/p_{T,t})$ parameters would be forced to be consistent. This would make maximal use of the available data to determine the background as precisely as possible.

Another way to reduce the impact of the background is to select on a higher $p_{T,t}$. This does require larger data samples, increases the signal to background ratio. As mentioned, the analysis in [46] also profits from the increased signal strength with larger $p_{T,t}$.

7.4 Path length dependence

In this work no discernible difference between the associated yield was found depending on the angle to the event plane at higher associated particle momentum ($p_{T,a} > 8$ GeV/c). This measurement with trigger selected on their angle to the reaction plane was introduced as an improvement/addition to jet asymmetry studies, which is difficult to directly interpret as a path length difference as we discussed in Section 1.4.3. With the di-jet asymmetry it is hard to tell which contribution due to the path length dependence, and which part may be due to other effects that quench one of the jets more strongly than the other. In [58] it is suggested that the mass of the initial parton might be the leading effect. This analysis is not susceptible to that particular problem, and even though unfortunately no significant effect was found, we will discuss effects that could influence the interpretation of the jet orientation yield ratio for the sake of completeness.

First of all it is important to keep in mind that not only the associated particles are subject to quenching, but the leading particle as well. This effect is closely related to the fragmentation bias discussed before.

Not all effects of collective motion in the QGP on the quenching process are fully understood. The differences in radial expansion could change the amount of jet quenching, but more research would be necessary to determine how this would influence the jet orientation yield ratio.

In order to incorporate the effect of these possible biases the analysis was repeated on AMPT. There was no discernible difference in AMPT as well. It would be interesting to explore whether the dependence of the associated yield on the trigger particle orientation is also small in parton energy loss models, like JEWEL. The absence of a clear effect also raises the question whether the difference between energy loss of partons propagating in directions along and perpendicular to the reaction plane is

small, or whether the effect is masked by one of the biases discussed above. Whether other observables, like γ -hadron correlation measurements, are more sensitive to the path length dependence of energy loss, can be studied with model calculations.

Appendix A

Fitting results

A.1 pp-collisions

Figure A.1 contains all side projections of the dihadron histograms with the fitted background, and Table A.1 contains the corresponding yields.

A.2 PbPb-collisions, without trigger selection

Figure A.2 contains all side projections of the dihadron histograms with the fitted background, and Table A.2 contains the corresponding yields.

A.3 PbPb-collisions, with selected trigger

Figure A.3 contains all side projections of the dihadron histograms with the fitted background with in-plane triggers and Table A.3 the corresponding yields. Figure A.4 has the same, but with mid-plane triggers and Table A.4 the corresponding yields. And Figure A.5 for out-of-plane triggers and Table A.5 the corresponding yields.

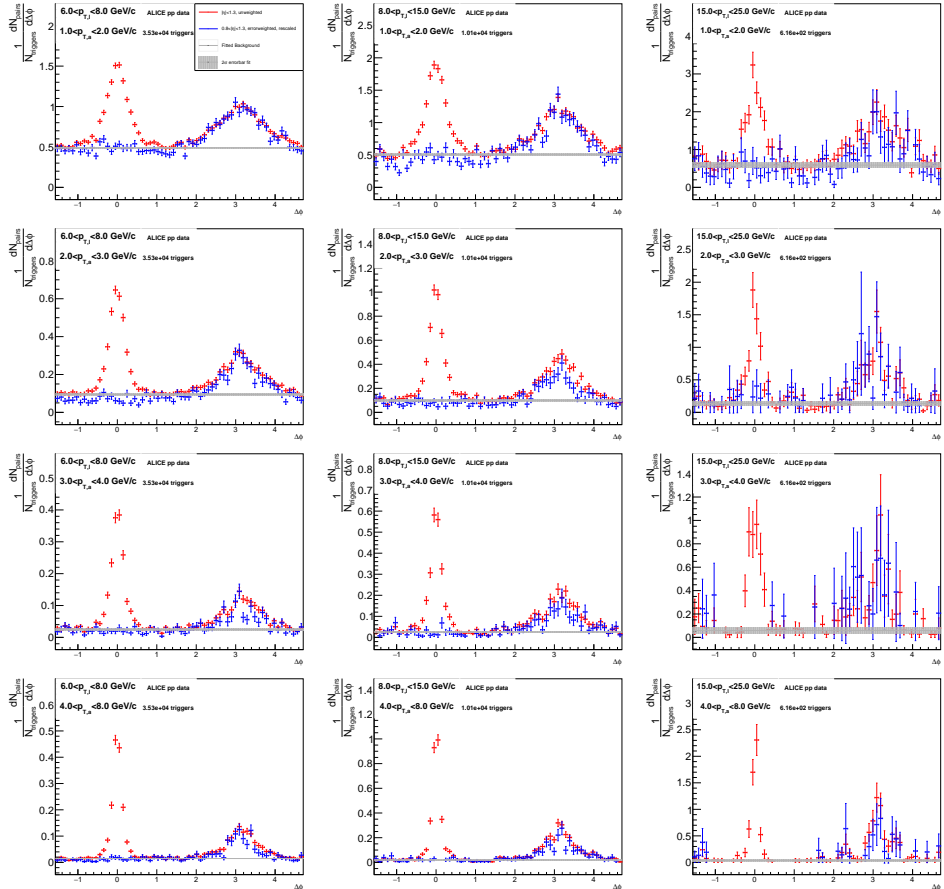


Figure A.1: The $\Delta\phi$ -projections of the pp-data for all p_T -ranges. From left to right: increasing $p_{T,t}$, from top to bottom: increasing $p_{T,a}$. The colors represent projections of the data over different η -ranges.

$p_{T,t}$	$p_{T,a}$	Y_{near}	$\sigma_{Y\text{near}}$	Y_{away}	$\sigma_{Y\text{away}}$
6.0 – 8.0	1.0 – 2.0	$7.14e + 01$	$1e + 00$	$2.47e + 01$	$6e - 01$
6.0 – 8.0	2.0 – 3.0	$2.94e + 01$	$6e - 01$	$9.06e + 00$	$3e - 01$
6.0 – 8.0	3.0 – 4.0	$1.56e + 01$	$4e - 01$	$4.04e + 00$	$2e - 01$
6.0 – 8.0	4.0 – 8.0	$1.53e + 01$	$3e - 01$	$4.13e + 00$	$2e - 01$
8.0 – 15.0	1.0 – 2.0	$9.12e + 01$	$2e + 00$	$3.39e + 01$	$1e + 00$
8.0 – 15.0	2.0 – 3.0	$4.28e + 01$	$1e + 00$	$1.47e + 01$	$5e - 01$
8.0 – 15.0	3.0 – 4.0	$2.22e + 01$	$7e - 01$	$7.41e + 00$	$3e - 01$
8.0 – 15.0	4.0 – 8.0	$2.88e + 01$	$8e - 01$	$8.78e + 00$	$4e - 01$
15.0 – 25.0	1.0 – 2.0	$1.21e + 02$	$9e + 00$	$5.51e + 01$	$5e + 00$
15.0 – 25.0	2.0 – 3.0	$5.98e + 01$	$6e + 00$	$2.24e + 01$	$3e + 00$
15.0 – 25.0	3.0 – 4.0	$3.98e + 01$	$5e + 00$	$1.94e + 01$	$3e + 00$
15.0 – 25.0	4.0 – 8.0	$5.36e + 01$	$5e + 00$	$2.53e + 01$	$3e + 00$

Table A.1: The yields in pp.

$p_{T,t}$	$p_{T,a}$	Y_{near}	$\sigma_{Y\text{near}}$	Y_{away}	$\sigma_{Y\text{away}}$
6.0 – 8.0	1.0 – 2.0	$1.26e + 02$	$3e + 00$	$4.28e + 01$	$2e + 00$
6.0 – 8.0	2.0 – 3.0	$4.64e + 01$	$9e - 01$	$8.15e + 00$	$7e - 01$
6.0 – 8.0	3.0 – 4.0	$1.86e + 01$	$4e - 01$	$1.91e + 00$	$3e - 01$
6.0 – 8.0	4.0 – 8.0	$1.72e + 01$	$3e - 01$	$1.75e + 00$	$1e - 01$
8.0 – 15.0	1.0 – 2.0	$1.42e + 02$	$4e + 00$	$5.53e + 01$	$3e + 00$
8.0 – 15.0	2.0 – 3.0	$5.62e + 01$	$2e + 00$	$1.36e + 01$	$9e - 01$
8.0 – 15.0	3.0 – 4.0	$2.48e + 01$	$7e - 01$	$4.40e + 00$	$4e - 01$
8.0 – 15.0	4.0 – 8.0	$3.29e + 01$	$5e - 01$	$5.58e + 00$	$3e - 01$
15.0 – 25.0	1.0 – 2.0	$1.69e + 02$	$2e + 01$	$8.46e + 01$	$1e + 01$
15.0 – 25.0	2.0 – 3.0	$7.02e + 01$	$5e + 00$	$2.01e + 01$	$4e + 00$
15.0 – 25.0	3.0 – 4.0	$2.90e + 01$	$5e + 00$	$5.95e + 00$	$3e + 00$
15.0 – 25.0	4.0 – 8.0	$5.84e + 01$	$2e + 00$	$1.66e + 01$	$1e + 00$

Table A.2: The yields in PbPb, plane-inclusive.

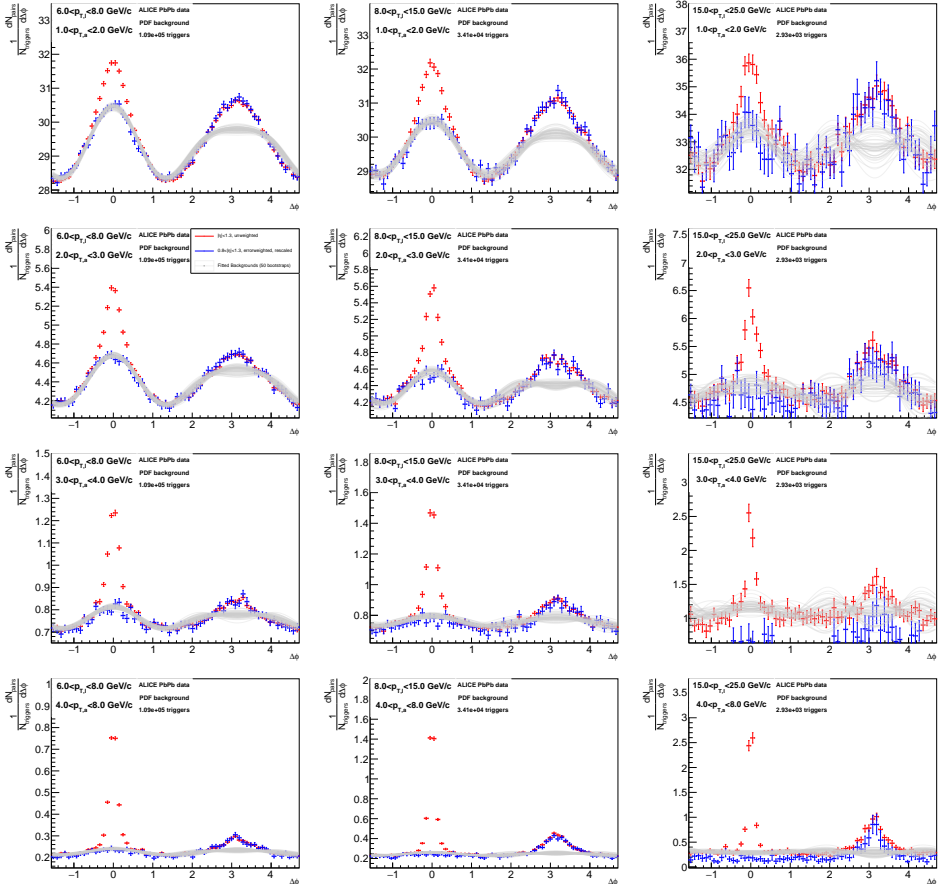


Figure A.2: The $\Delta\phi$ -projections of the PbPb-data for all p_T -ranges. From left to right: increasing $p_{T,t}$, from top to bottom: increasing $p_{T,a}$. The colors represent projections of the data over different η -ranges.

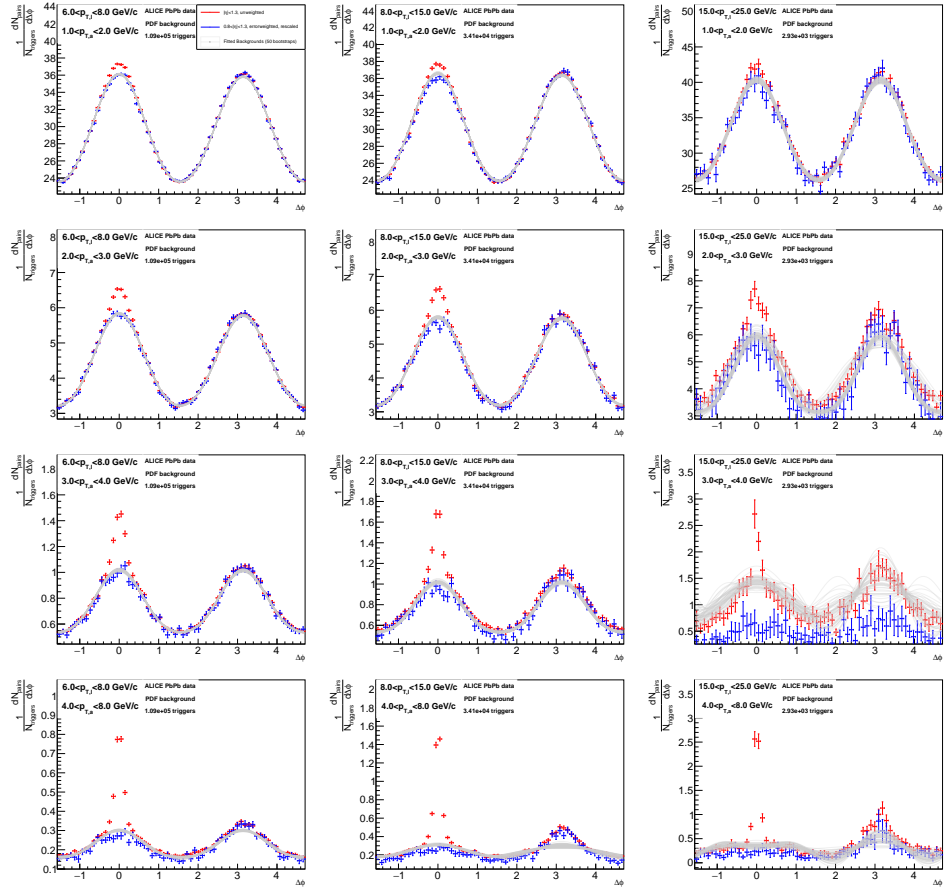


Figure A.3: The $\Delta\phi$ -projections of the in-plane PbPb-data for all p_T -ranges. From left to right: increasing $p_{T,t}$, from top to bottom: increasing $p_{T,a}$. The colors represent projections of the data over different η -ranges. All backgrounds are provided by the PDF method, except for the highest p_T -bins where statistics wasn't sufficient as has been indicated in plot.

$p_{T,t}$	$p_{T,a}$	Y_{near}	$\sigma_{Y\text{near}}$	Y_{away}	$\sigma_{Y\text{away}}$
6.0 – 8.0	1.0 – 2.0	$7.31e + 01$	$7e + 00$	$1.64e + 01$	$4e + 00$
6.0 – 8.0	2.0 – 3.0	$3.86e + 01$	$2e + 00$	$4.23e + 00$	$1e + 00$
6.0 – 8.0	3.0 – 4.0	$1.68e + 01$	$1e + 00$	$1.29e + 00$	$7e - 01$
6.0 – 8.0	4.0 – 8.0	$1.57e + 01$	$5e - 01$	$1.07e + 00$	$2e - 01$
8.0 – 15.0	1.0 – 2.0	$6.18e + 01$	$1e + 01$	$1.26e + 01$	$7e + 00$
8.0 – 15.0	2.0 – 3.0	$4.09e + 01$	$4e + 00$	$5.17e + 00$	$3e + 00$
8.0 – 15.0	3.0 – 4.0	$2.60e + 01$	$1e + 00$	$5.50e + 00$	$9e - 01$
8.0 – 15.0	4.0 – 8.0	$3.47e + 01$	$8e - 01$	$6.91e + 00$	$5e - 01$
15.0 – 25.0	1.0 – 2.0	$1.12e + 02$	$4e + 01$	$2.91e + 01$	$2e + 01$
15.0 – 25.0	2.0 – 3.0	$1.09e + 02$	$2e + 01$	$3.96e + 01$	$1e + 01$
15.0 – 25.0	3.0 – 4.0	$3.00e + 01$	$9e + 00$	$5.71e + 00$	$6e + 00$
15.0 – 25.0	4.0 – 8.0	$6.21e + 01$	$3e + 00$	$1.74e + 01$	$2e + 00$

Table A.3: The jet-yields in PbPb of jets with in-plane triggers.

$p_{T,t}$	$p_{T,a}$	Y_{near}	$\sigma_{Y\text{near}}$	Y_{away}	$\sigma_{Y\text{away}}$
6.0 – 8.0	1.0 – 2.0	$5.25e + 01$	$7e + 00$	$4.60e + 00$	$4e + 00$
6.0 – 8.0	2.0 – 3.0	$3.01e + 01$	$2e + 00$	$-7.23e - 01$	$1e + 00$
6.0 – 8.0	3.0 – 4.0	$1.59e + 01$	$1e + 00$	$4.39e - 01$	$7e - 01$
6.0 – 8.0	4.0 – 8.0	$1.62e + 01$	$8e - 01$	$1.24e + 00$	$4e - 01$
8.0 – 15.0	1.0 – 2.0	$6.67e + 01$	$1e + 01$	$2.01e + 01$	$8e + 00$
8.0 – 15.0	2.0 – 3.0	$3.25e + 01$	$4e + 00$	$5.73e - 02$	$2e + 00$
8.0 – 15.0	3.0 – 4.0	$2.27e + 01$	$2e + 00$	$3.01e + 00$	$8e - 01$
8.0 – 15.0	4.0 – 8.0	$3.21e + 01$	$8e - 01$	$5.15e + 00$	$4e - 01$
15.0 – 25.0	1.0 – 2.0	$1.20e + 02$	$4e + 01$	$6.59e + 01$	$2e + 01$
15.0 – 25.0	2.0 – 3.0	$8.74e + 01$	$1e + 01$	$3.31e + 01$	$9e + 00$
15.0 – 25.0	3.0 – 4.0	$3.18e + 01$	$9e + 00$	$9.77e + 00$	$6e + 00$
15.0 – 25.0	4.0 – 8.0	$5.62e + 01$	$4e + 00$	$1.56e + 01$	$2e + 00$

Table A.4: The jet-yields in PbPb of jets with mid-plane triggers.

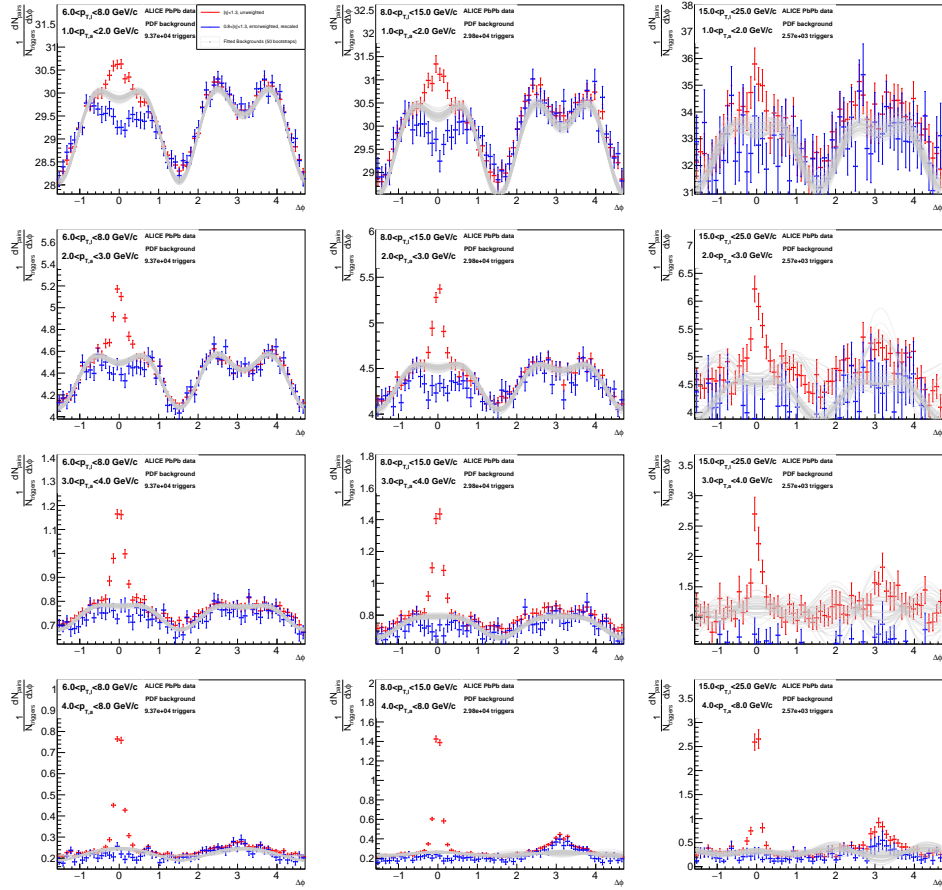


Figure A.4: The $\Delta\phi$ -projections of the mid-plane PbPb-data for all p_T -ranges. From left to right: increasing $p_{T,t}$, from top to bottom: increasing $p_{T,a}$. The colors represent projections of the data over different η -ranges. All backgrounds are provided by the PDF method, except for the highest p_T -bins where statistics wasn't sufficient as has been indicated in plot.

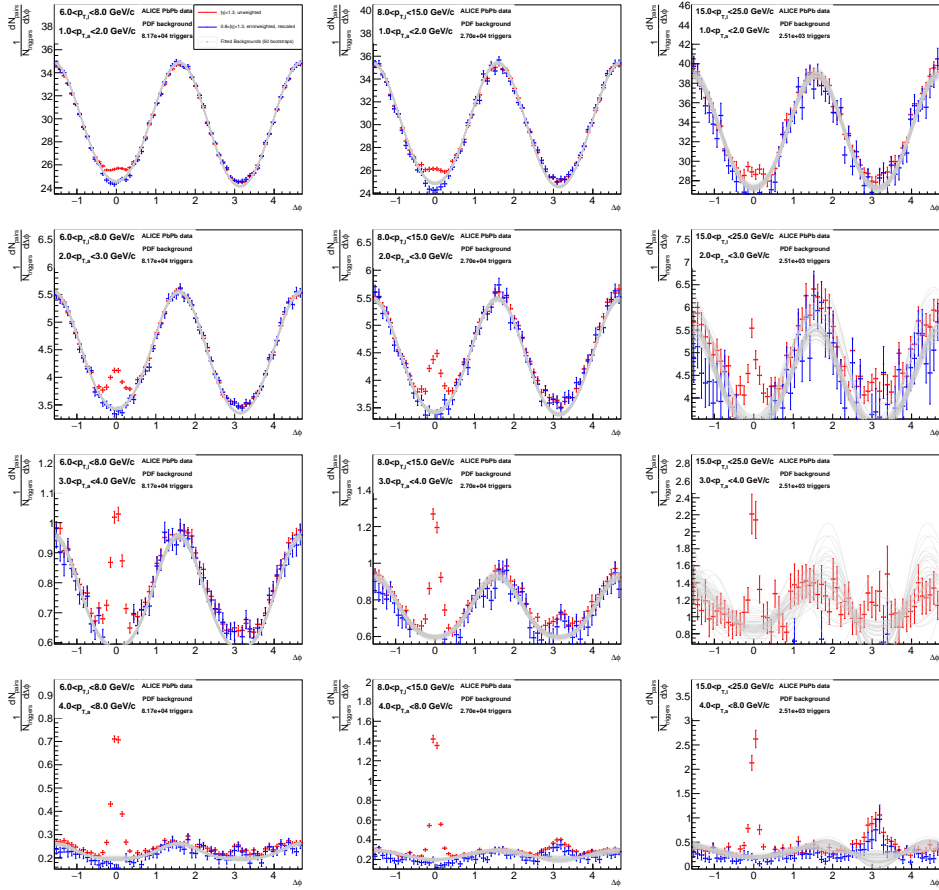


Figure A.5: The $\Delta\phi$ -projections of the out-of-plane PbPb-data for all p_T -ranges. From left to right: increasing $p_{T,t}$, from top to bottom: increasing $p_{T,a}$. The colors represent projections of the data over different η -ranges. All backgrounds are provided by the PDF method, except for the highest p_T -bins where statistics wasn't sufficient as has been indicated in plot.

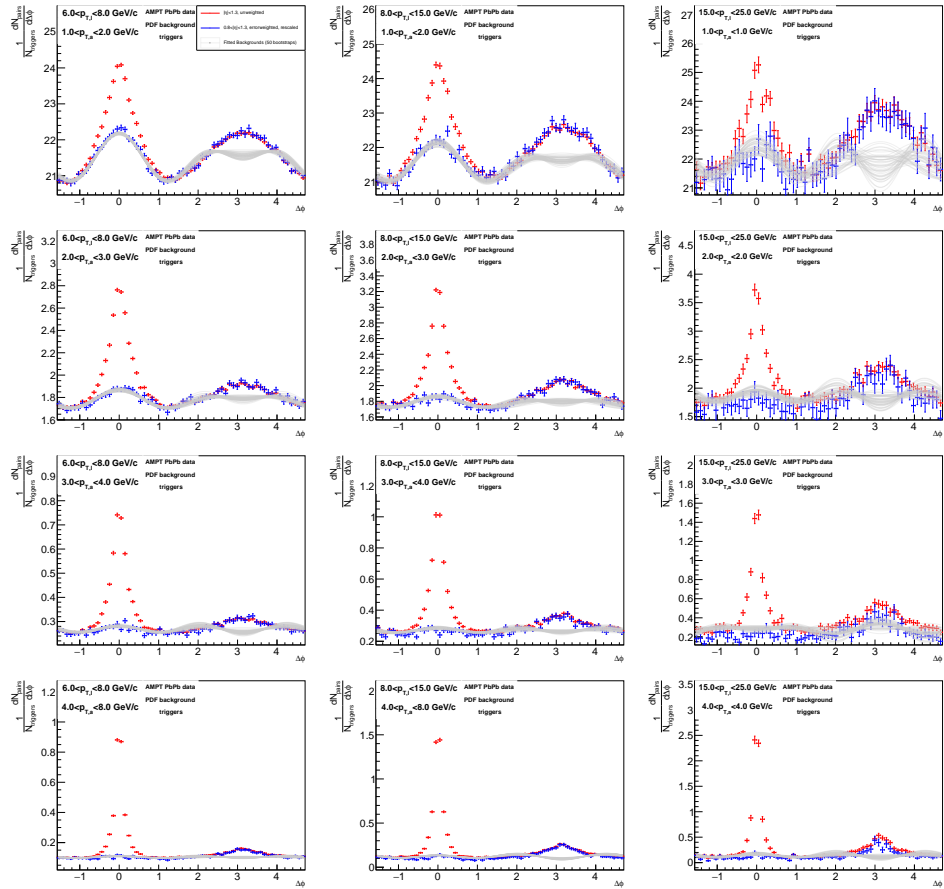


Figure A.6: The $\Delta\phi$ -projections of the plane-inclusive PbPb-MC-data for all p_T -ranges. From left to right: increasing $p_{T,t}$, from top to bottom: increasing $p_{T,a}$. The colors represent projections of the data over different η -ranges.

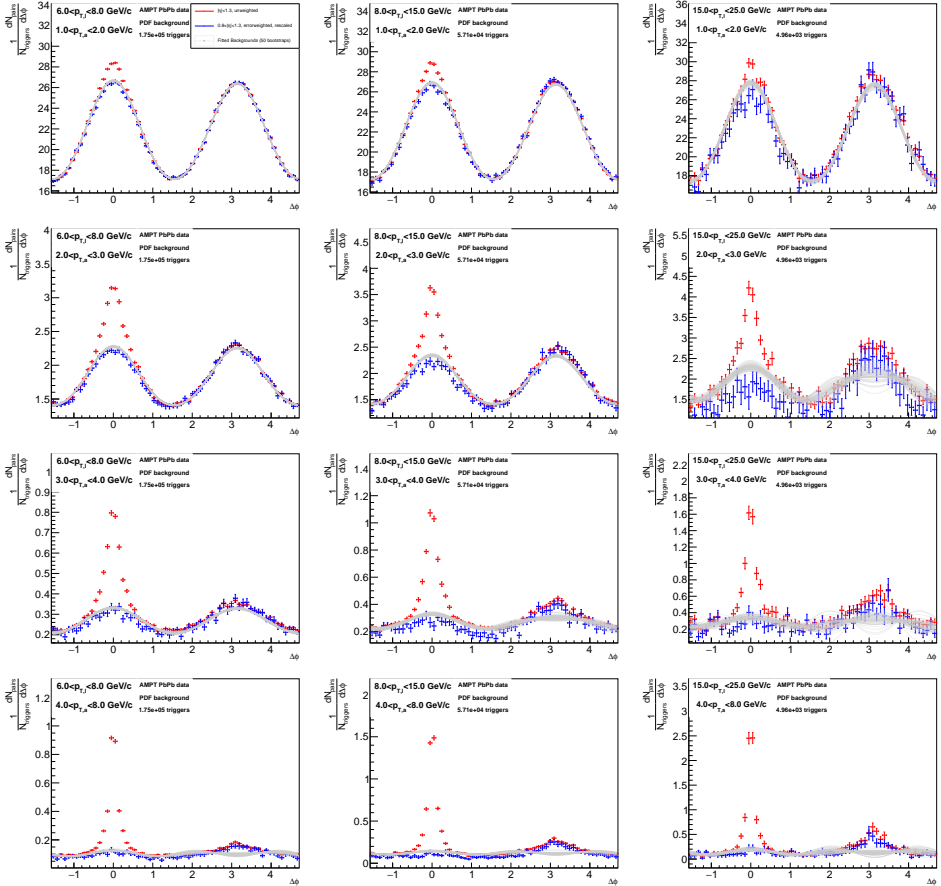


Figure A.7: The $\Delta\phi$ -projections of the in-plane PbPb-MC-data for all p_T -ranges. From left to right: increasing $p_{T,t}$, from top to bottom: increasing $p_{T,a}$. The colors represent projections of the data over different η -ranges. The fit uses $S_{4,4} = 0.7$.

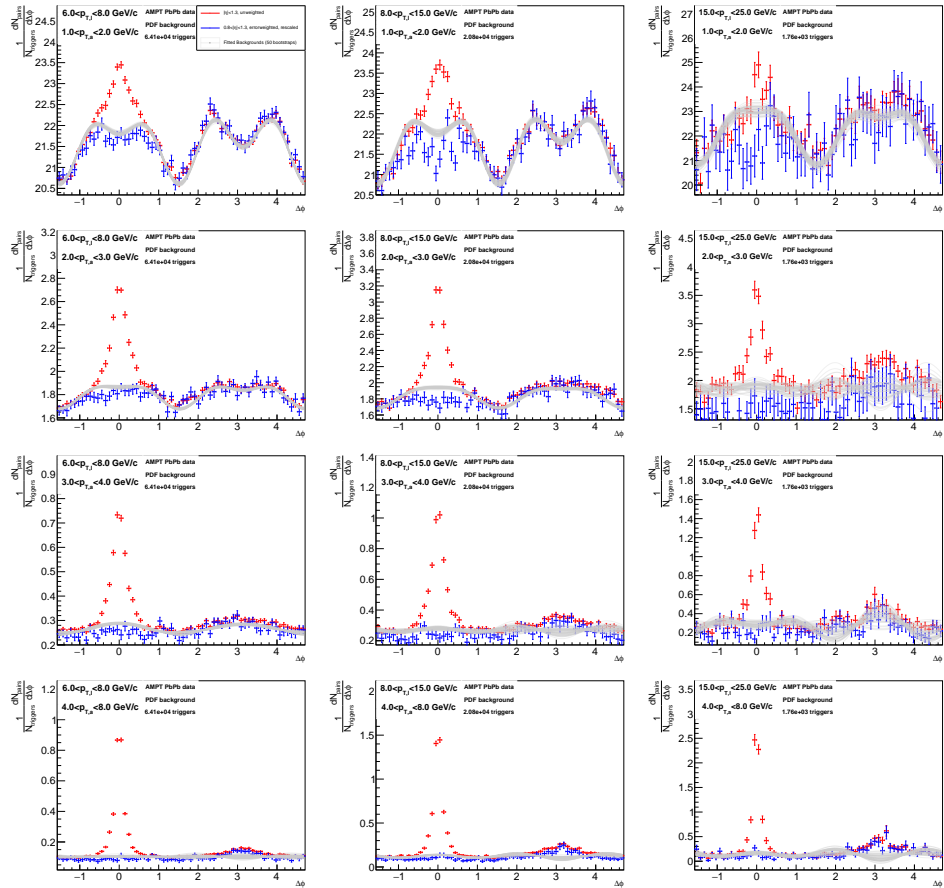


Figure A.8: The $\Delta\phi$ -projections of the mid-plane PbPb-MC-data for all p_T -ranges. From left to right: increasing $p_{T,t}$, from top to bottom: increasing $p_{T,a}$. The colors represent projections of the data over different η -ranges. The fit uses $S_{4,4} = 0.7$.

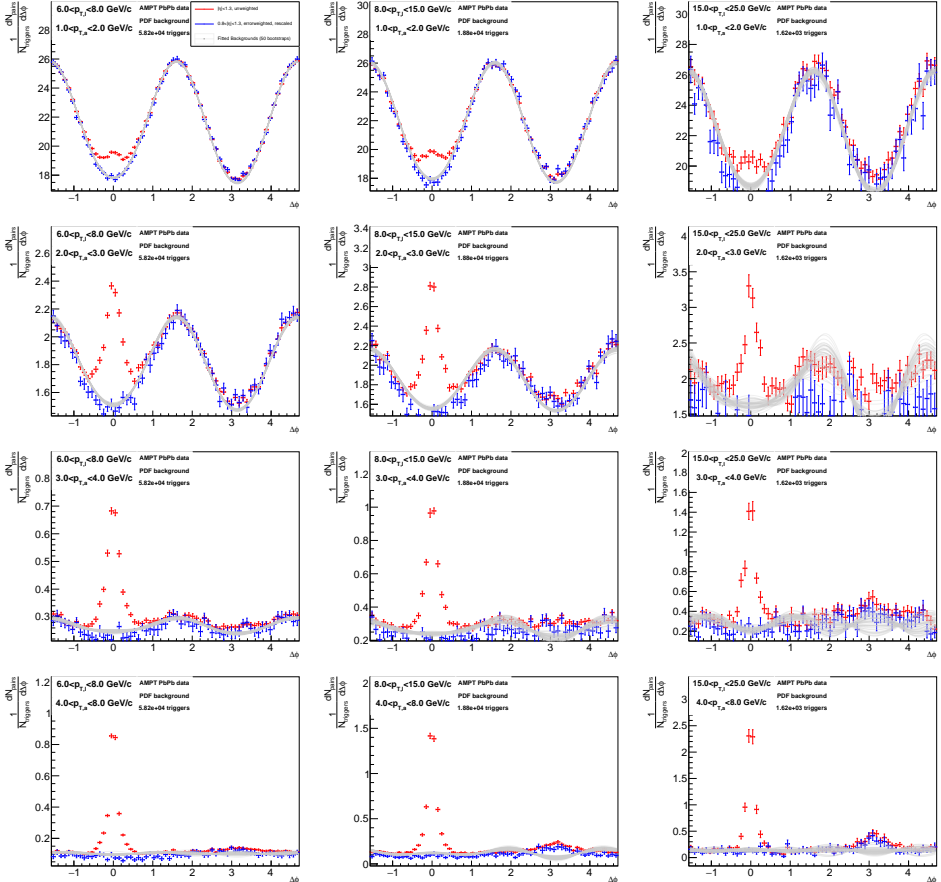


Figure A.9: The $\Delta\phi$ -projections of the out-of-plane PbPb-MC-data for all p_T -ranges. From left to right: increasing $p_{T,t}$, from top to bottom: increasing $p_{T,a}$. The colors represent projections of the data over different η -ranges. The fit uses $S_{4,4} = 0.7$.

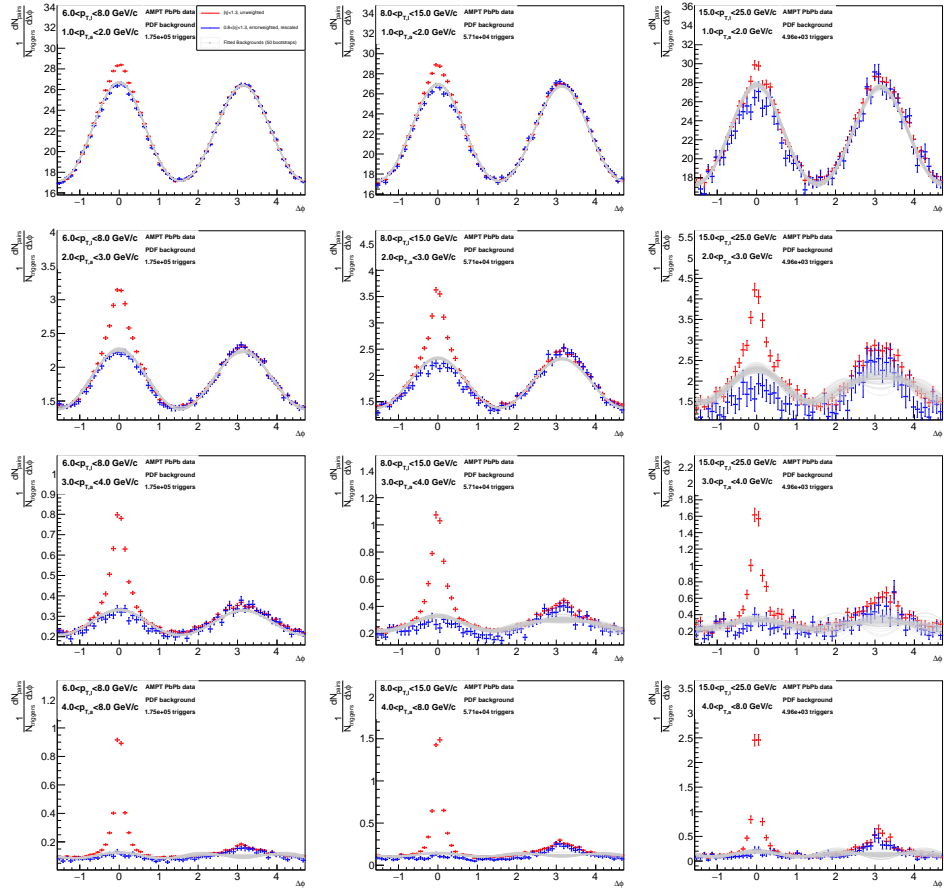


Figure A.10: The $\Delta\phi$ –projections of the in-plane PbPb-MC-data for all p_T -ranges. From left to right: increasing $p_{T,t}$, from top to bottom: increasing $p_{T,a}$. The colors represent projections of the data over different η -ranges. The fit uses $S_{4,4} = 0.1$.

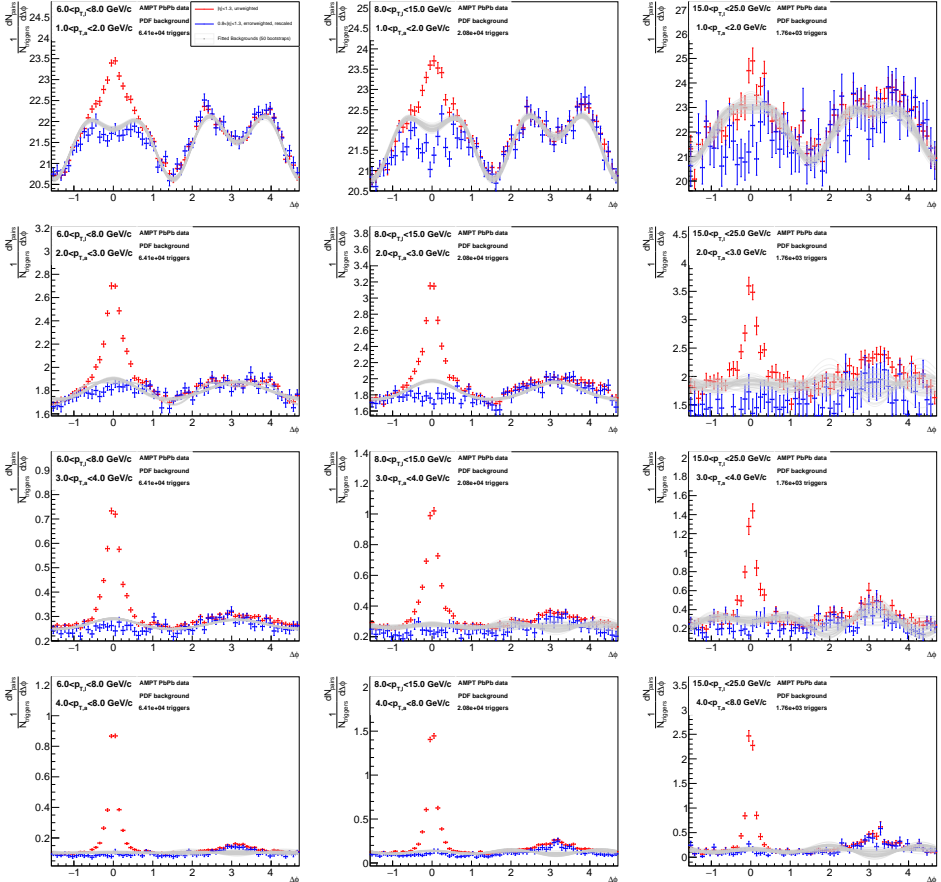


Figure A.11: The $\Delta\phi$ -projections of the mid-plane PbPb-MC-data for all p_T -ranges. From left to right: increasing $p_{T,t}$, from top to bottom: increasing $p_{T,a}$. The colors represent projections of the data over different η -ranges. The fit uses $S_{4,4} = 0.1$.

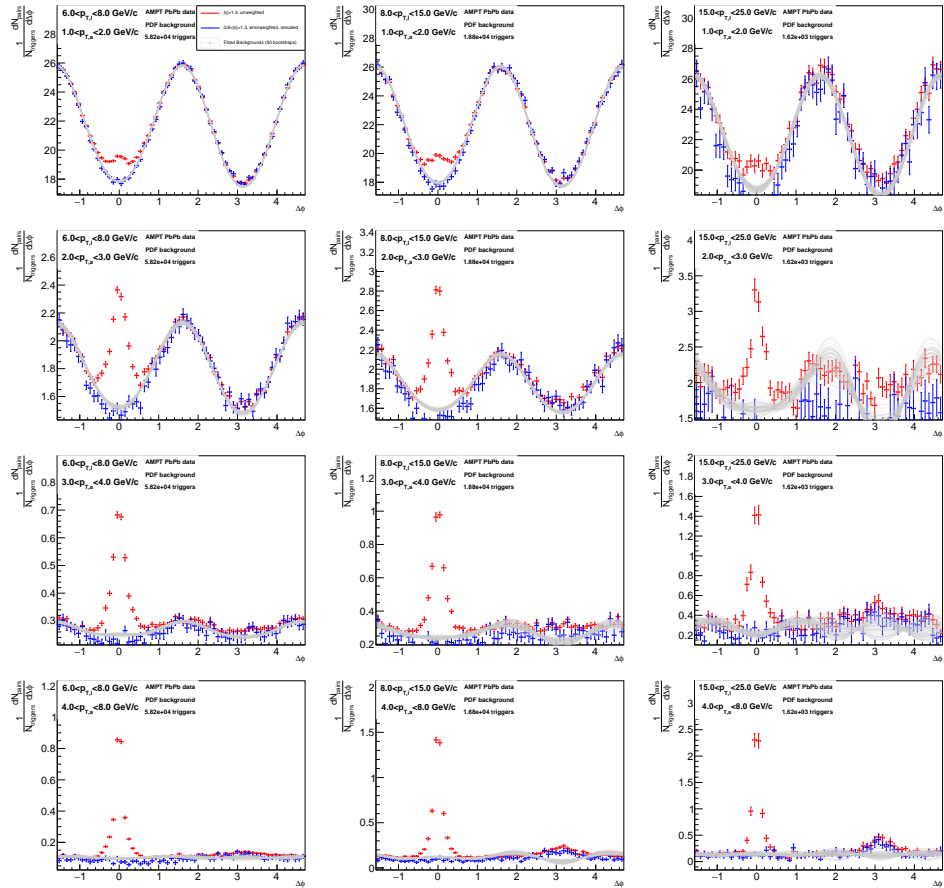


Figure A.12: The $\Delta\phi$ -projections of the out-of-plane PbPb-MC-data for all p_T -ranges. From left to right: increasing $p_{T,t}$, from top to bottom: increasing $p_{T,a}$. The colors represent projections of the data over different η -ranges. The fit uses $S_{4,4} = 0.1$.

$p_{T,t}$	$p_{T,a}$	Y_{near}	$\sigma_{Y\text{near}}$	Y_{away}	$\sigma_{Y\text{away}}$
6.0 – 8.0	1.0 – 2.0	$6.52e + 01$	$7e + 00$	$4.18e + 00$	$4e + 00$
6.0 – 8.0	2.0 – 3.0	$3.78e + 01$	$2e + 00$	$3.07e + 00$	$1e + 00$
6.0 – 8.0	3.0 – 4.0	$2.08e + 01$	$1e + 00$	$2.99e + 00$	$6e - 01$
6.0 – 8.0	4.0 – 8.0	$1.73e + 01$	$6e - 01$	$1.93e + 00$	$2e - 01$
8.0 – 15.0	1.0 – 2.0	$8.15e + 01$	$1e + 01$	$1.55e + 01$	$8e + 00$
8.0 – 15.0	2.0 – 3.0	$5.16e + 01$	$4e + 00$	$1.05e + 01$	$2e + 00$
8.0 – 15.0	3.0 – 4.0	$2.26e + 01$	$1e + 00$	$4.26e + 00$	$8e - 01$
8.0 – 15.0	4.0 – 8.0	$3.16e + 01$	$9e - 01$	$4.38e + 00$	$5e - 01$
15.0 – 25.0	1.0 – 2.0	$1.12e + 02$	$4e + 01$	$7.46e + 01$	$2e + 01$
15.0 – 25.0	2.0 – 3.0	$8.56e + 01$	$4e + 01$	$3.94e + 01$	$2e + 01$
15.0 – 25.0	3.0 – 4.0	$2.49e + 01$	$8e + 00$	$2.29e + 00$	$6e + 00$
15.0 – 25.0	4.0 – 8.0	$5.64e + 01$	$3e + 00$	$1.67e + 01$	$2e + 00$

Table A.5: The jet-yields in PbPb of jets with out-of-plane triggers.

Appendix B

Associated yield ratio

Figure B.1 shows the results when using the Fourier background. Figure B.2 shows the results when using the PDF background.

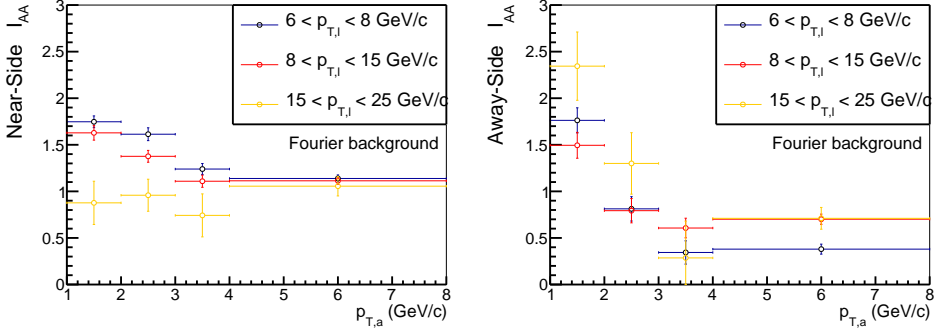


Figure B.1: The I_{AA} for the near-side charged jet (left) and the away-side charged jet (right) in the plane-inclusive analysis. Background determined by performing the Fourier-analysis on the near-side.

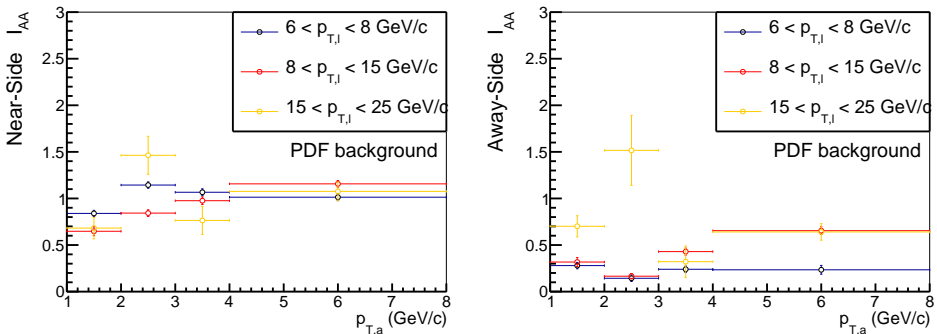


Figure B.2: The I_{AA} for the near-side charged jet (left) and the away-side charged jet (right) in the plane-inclusive analysis. Background determined by using the plane-inclusive derivation of the PDF method. With $8 < p_{T,t} < 15$ GeV/c at $p_{T,a} > 4$ GeV/c or $15 < p_{T,t} < 25$ GeV/c at $p_{T,a} > 3$ GeV/c a flat background is subtracted instead.

Appendix C

Comparison with other work

The vernacular between the equations in Section 1.5.4 and [63] differs on some points. Furthermore there are slight differences between assumptions. Listed below are the significant differences.

- In [63] the calculation is performed for a unsymmetrized sector \mathcal{R}' , instead of the \mathcal{R} used here. This results in the addition of a sine term, though it is clear that this term disappears at the addition of the symmetric partner of \mathcal{R}' .
- The result of Equation 1.34 are extended to work for comparison with an event plane of any order in equation 3 from [63]. The equations here are simplified for Ψ_2 , which means several values of $S_{n,m}$ drop out.
- Most notably [63] assumes less restrictions on the correlations between several event planes. In and after Equation 1.23 the assumption was made that there is no correlation between Ψ_n and Ψ_m for $m \neq n$ and both unequal to 2. This leads to the factorisation of the $C_{n,m,j}$ factors defined in [63] into $S_{n,n}$ and $S_{m,m}$. The dependence on j , the order of event plane on which the trigger selection takes place, is still there, but it is now hidden in the definition of $\Delta\Psi_n$. This simplification has the advantage of reducing the amount of model correlation parameters that are not straightforward to measure in practice. at the disadvantage of introducing a possible bias if this assumption is too strong. It is however an assumption that probably does not hold for cases when $j \neq 2$, since the second order event plane probably has the strongest correlations with the others.

Bibliography

- [1] Morad Aaboud et al. Measurement of jet fragmentation in Pb+Pb and pp collisions at $\sqrt{s_{NN}} = 5.02$ TeV with the ATLAS detector. *Phys. Rev. C*, 98(2):024908, 2018.
- [2] Morad Aaboud et al. Comparison of Fragmentation Functions for Jets Dominated by Light Quarks and Gluons from pp and Pb+Pb Collisions in ATLAS. *Phys. Rev. Lett.*, 123(4):042001, 2019.
- [3] Georges Aad et al. Measurement of inclusive jet charged-particle fragmentation functions in Pb+Pb collisions at $\sqrt{s_{NN}} = 2.76$ TeV with the ATLAS detector. *Phys. Lett. B*, 739:320–342, 2014.
- [4] Georges Aad et al. Z boson production in Pb+Pb collisions at $\sqrt{s_{NN}} = 5.02$ TeV measured by the ATLAS experiment. *Phys. Lett. B*, 802:135262, 2020.
- [5] K. Aamodt et al. The ALICE experiment at the CERN LHC. *JINST*, 3:S08002, 2008.
- [6] K. Aamodt et al. The ALICE experiment at the CERN LHC. *JINST*, 3:S08002, 2008.
- [7] K Aamodt et al. Alignment of the ALICE Inner Tracking System with cosmic-ray tracks. *JINST*, 5:P03003, 2010.
- [8] Betty Abelev et al. Centrality Dependence of Charged Particle Production at Large Transverse Momentum in Pb–Pb Collisions at $\sqrt{s_{NN}} = 2.76$ TeV. *Phys. Lett. B*, 720:52–62, 2013.
- [9] Betty Bezverkhny Abelev et al. Performance of the ALICE Experiment at the CERN LHC. *Int. J. Mod. Phys.*, A29:1430044, 2014.
- [10] J. Adam, D. Adamová, M.M. Aggarwal, G. Aglieri Rinella, M. Agnello, N. Agrawal, Z. Ahammed, S.U. Ahn, S. Aiola, A. Akindinov, and et al. Azimuthal anisotropy of charged jet production in $s_{NN}=2.76$ teV pb–pb collisions. *Physics Letters B*, 753:511–525, Feb 2016.
- [11] L. Adamczyk et al. Beam Energy Dependence of Jet-Quenching Effects in Au+Au Collisions at $\sqrt{s_{NN}} = 7.7, 11.5, 14.5, 19.6, 27, 39$, and 62.4 GeV. *Phys. Rev. Lett.*, 121(3):032301, 2018.

- [12] J. Adams et al. Evidence from d + Au measurements for final state suppression of high p(T) hadrons in Au+Au collisions at RHIC. *Phys. Rev. Lett.*, 91:072304, 2003.
- [13] A. Adare et al. Measurement of two-particle correlations with respect to second- and third-order event planes in Au+Au collisions at $\sqrt{s_{NN}} = 200$ GeV. *Phys. Rev. C*, 99(5):054903, 2019.
- [14] S. S. et al. PHENIX Collaboration Adler. Azimuthal angle correlations for rapidity separated hadron pairs in d + Au collisions at $\sqrt{s_{NN}} = 200$ GeV. *Phys. Rev. Lett.*, 96:222301, Jun 2006.
- [15] H. Agakishiev et al. Event-plane-dependent dihadron correlations with harmonic v_n subtraction in Au + Au collisions at $\sqrt{s_{NN}} = 200$ GeV. *Phys. Rev. C*, 89(4):041901, 2014.
- [16] H. Agakishiev et al. Measurements of dihadron correlations relative to the event plane in Au+Au collisions at $\sqrt{s_{NN}} = 200$ GeV. *Chin. Phys. C*, 45(4):044002, 2021.
- [17] G. Aglieri Rinella, A. Kluge, and M. Krivda. The level 0 pixel trigger system for the ALICE experiment. *JINST*, 2:P01007, 2007.
- [18] Mark G. Alford, Andreas Schmitt, Krishna Rajagopal, and Thomas Schäfer. Color superconductivity in dense quark matter. *Rev. Mod. Phys.*, 80:1455–1515, 2008.
- [19] ALICE Collaboration. Elliptic flow of charged particles at midrapidity relative to the spectator plane in pb-pb and xe-xe collisions, 2022.
- [20] B. Andersson, G. Gustafson, and B. Söderberg. A general model for jet fragmentation. *Z. Phys. C - Particles and Fields*, 20:317–329, dec 1983.
- [21] G. Aad et al ATLAS Collaboration. Observation of a centrality-dependent dijet asymmetry in lead-lead collisions at $\sqrt{s_{NN}} = 2.76$ TeV with the ATLAS detector at the LHC. *Physical Review Letters*, 105(25), dec 2010.
- [22] G. Aad et al. ATLAS Collaboration. Measurement of charged-particle spectra in pb+pb collisions at $\sqrt{s_{NN}} = 2.76$ TeV with the ATLAS detector at the LHC. *Journal of High Energy Physics*, 2015(9), sep 2015.
- [23] M. Aaboud et al ATLAS Collaboration. Measurement of the nuclear modification factor for inclusive jets in pb+pb collisions at $\sqrt{s_{NN}} = 5.02$ TeV with the ATLAS detector. *Physics Letters B*, 790:108–128, mar 2019.
- [24] Y. Belikov, M. Ivanov, K. Safarik, and J. Bracinik. TPC tracking and particle identification in high density environment. *eConf*, C0303241:TULT011, 2003.
- [25] Yu Belikov, K. Safarik, and B. Batyunya. Kalman Filtering Application for Track Recognition and Reconstruction in ALICE Tracking System. 1997.
- [26] S. Bethke. α_s (2019): Precision measurements of the qcd coupling, 2019.

[27] J. Bielcikova, S. Esumi, K. Filimonov, S. Voloshin, and J. P. Wurm. Elliptic flow contribution to two particle correlations at different orientations to the reaction plane. *Phys. Rev.*, C69:021901, 2004.

[28] Ante Bilandzic. Anisotropic flow measured from multi-particle azimuthal correlations for pb–pb collisions at 2.76 TeV by ALICE at the LHC. *Nuclear Physics A*, 904-905:515c–518c, may 2013.

[29] Ante Bilandzic, Raimond Snellings, and Sergei Voloshin. Flow analysis with cumulants: Direct calculations. *Physical Review C*, 83(4), apr 2011.

[30] René Brun, F. Bruyant, Federico Carminati, Simone Giani, M. Maire, A. McPher-
son, G. Patrick, and L. Urban. GEANT Detector Description and Simulation
Tool. 1994.

[31] Matteo Cacciari, Gavin P. Salam, and Gregory Soyez. FastJet user manual. *The
European Physical Journal C*, 72(3), mar 2012.

[32] Jorge Casalderrey-Solana, José Guilherme Milhano, and Urs Achim Wiedemann.
Jet quenching via jet collimation. *Journal of Physics G: Nuclear and Particle
Physics*, 38(3):035006, jan 2011.

[33] CERN. Root a data analysis framework. <https://root.cern.ch/>. Accessed:
2019-01-08.

[34] Serguei Chatrchyan et al. Studies of jet quenching using isolated-photon+jet
correlations in PbPb and pp collisions at $\sqrt{s_{NN}} = 2.76$ TeV. *Phys. Lett. B*,
718:773–794, 2013.

[35] Serguei Chatrchyan et al. Measurement of Jet Fragmentation in PbPb and pp
Collisions at $\sqrt{s_{NN}} = 2.76$ TeV. *Phys. Rev. C*, 90(2):024908, 2014.

[36] Serguei Chatrchyan et al. Studies of dijet transverse momentum balance and
pseudorapidity distributions in pPb collisions at $\sqrt{s_{NN}} = 5.02$ TeV. *Eur. Phys.
J. C*, 74(7):2951, 2014.

[37] ALICE collaboration. The alice off-line project. <http://alice-offline.web.cern.ch>. Accessed: 2019-01-08.

[38] ALICE collaboration. More details on the alice tpc. <http://alice.web.cern.ch/detectors/more-details-alice-tpc>. Accessed: 2018-12-15.

[39] ALICE collaboration. Time projection chamber. <http://alice.web.cern.ch/content/time-projection-chamber>. Accessed: 2018-12-15.

[40] ALICE Collaboration. Alice: Technical design report of the inner tracking
system. 1999.

[41] ALICE Collaboration. Exploring jet profiles in pb–pb collisions at 5.02 TeV
with the alice detector. *Nuclear Physics A*, 982:639–642, 2019.

- [42] ATLAS collaboration. Measurement of event-plane correlations in $\sqrt{s_{NN}} = 2.76$ TeV lead-lead collisions with the ATLAS detector. *Physical Review C*, 90(2), aug 2014.
- [43] Megan Connors, Christine Nattrass, Rosi Reed, and Sevil Salur. Jet measurements in heavy ion physics. *Reviews of Modern Physics*, 90(2), jun 2018.
- [44] M.J. Cush. Standard_model_of_elementary_particles.svg. https://en.wikipedia.org/wiki/File:Standard_Model_of_Elementary_Particles.svg. Accessed: 2022-08-16.
- [45] Philippe de Forcrand, Mikhail A. Stephanov, and Urs Wenger. On the phase diagram of QCD at finite isospin density. *PoS*, LATTICE2007:237, 2007.
- [46] R. Ehlers. Jet-Hadron Correlations Measured in Pb–Pb Collisions at $\sqrt{s_{NN}}$ with ALICE. PhD thesis, Yale University, 2020.
- [47] S. Chatrchyan et al. Observation and studies of jet quenching in PbPb collisions at $\sqrt{s_{NN}} = 2.76$ TeV. *Physical Review C*, 84(2), aug 2011.
- [48] K. Aamodt et al. ALICE Collaboration. Particle-yield modification in jetlike azimuthal dihadron correlations in pb-pb collisions at $\sqrt{s_{NN}} = 2.76$ TeV. *Physical Review Letters*, 108(9), mar 2012.
- [49] R. Aaij et al. LHCb Collaboration. Observation of a narrow pentaquark state, $pc(4312)^+$, and of the two-peak structure of the $pc(4450)^+$. *Physical Review Letters*, 122(22), jun 2019.
- [50] Lyndon Evans and Philip Bryant. LHC Machine. *JINST*, 3:S08001, 2008.
- [51] ALICE LCG Task Force. Alien - alice environment grid framework. <http://alien.web.cern.ch/>. Accessed: 2019-01-08.
- [52] M. Gell-Mann. A schematic model of baryons and mesons. *Physics Letters*, 8(3):214–215, 1964.
- [53] ALICE internal document. Hybrid tracks. <https://twiki.cern.ch/twiki/bin/viewauth/ALICE/HybridTracks>. Accessed: 2022-08-17.
- [54] Vardan Khachatryan et al. Measurement of transverse momentum relative to dijet systems in PbPb and pp collisions at $\sqrt{s_{NN}} = 2.76$ TeV. *JHEP*, 01:006, 2016.
- [55] Bao-An Li and Che Ming Ko. Formation of superdense hadronic matter in high energy heavy-ion collisions. *Phys. Rev. C*, 52:2037–2063, Oct 1995.
- [56] Zi-Wei Lin, Che Ming Ko, Bao-An Li, Bin Zhang, and Subrata Pal. Multiphase transport model for relativistic heavy ion collisions. *Physical Review C*, 72(6), dec 2005.
- [57] Christopher McGinn. Photon-jet correlations in pp and PbPb collisions at 5.02 TeV with CMS. *Nucl. Part. Phys. Proc.*, 289-290:333–337, 2017.

[58] José Guilherme Milhano and Korinna Christine Zapp. Origins of the di-jet asymmetry in heavy ion collisions, 2015.

[59] Michael L. Miller, Klaus Reygers, Stephen J. Sanders, and Peter Steinberg. Glauber modeling in high energy nuclear collisions. *Ann. Rev. Nucl. Part. Sci.*, 57:205–243, 2007.

[60] Michael L. Miller, Klaus Reygers, Stephen J. Sanders, and Peter Steinberg. Glauber modeling in high-energy nuclear collisions. *Annual Review of Nuclear and Particle Science*, 57(1):205–243, nov 2007.

[61] R. A. Millikan. On the elementary electrical charge and the avogadro constant. *Phys. Rev.*, 2:109–143, Aug 1913.

[62] J. L. Nagle and M. P. McCumber. Heavy ion initial conditions and correlations between higher moments in the spatial anisotropy. *Physical Review C*, 83(4), apr 2011.

[63] Christine Nattrass and Takahito Todoroki. Event plane dependence of the flow modulated background in dihadron and jet-hadron correlations in heavy ion collisions. *Phys. Rev. C*, 97(5):054911, 2018.

[64] NobelPrize.org. The nobel prize in physics 1979. <https://www.nobelprize.org/prizes/physics/1979/summary>. Accessed: 2022-08-17.

[65] WLCG Project Office. Welcome to the worldwide lhc computing grid. <http://wlcg.web.cern.ch/>. Accessed: 2019-01-08.

[66] Guang-You Qin and Berndt Müller. Explanation of dijet asymmetry in pb-pb collisions at the large hadron collider. *Physical Review Letters*, 106(16), apr 2011.

[67] Guang-You Qin and Xin-Nian Wang. Jet quenching in high-energy heavy-ion collisions. *Int. J. Mod. Phys. E*, 24(11):1530014, 2015.

[68] Paul Romatschke. Momentum broadening in an anisotropic plasma. *Physical Review C*, 75(1), jan 2007.

[69] Gavin P. Salam. Towards jetography. *The European Physical Journal C*, 67(3-4):637–686, may 2010.

[70] Christian Schmidt and Sayantan Sharma. The phase structure of QCD. *Journal of Physics G: Nuclear and Particle Physics*, 44(10):104002, aug 2017.

[71] Albert M Sirunyan et al. Observation of Medium-Induced Modifications of Jet Fragmentation in Pb-Pb Collisions at $\sqrt{s_{NN}} = 5.02$ TeV Using Isolated Photon-Tagged Jets. *Phys. Rev. Lett.*, 121(24):242301, 2018.

[72] Torbjorn Sjostrand, Stephen Mrenna, and Peter Z. Skands. PYTHIA 6.4 Physics and Manual. *JHEP*, 05:026, 2006.

[73] Oleksiy Sokolov. *Prototyping of the Silicon Strip Detectors for the Inner Tracker of the ALICE experiment*. 2006.

- [74] L. Adamczyk et al STAR Collaboration. Dijet imbalance measurements in $\sqrt{s_{NN}} = 200$ GeV at STAR. *Physical Review Letters*, 119(6), aug 2017.
- [75] M. Verweij. Modelling and measurement of jet quenching in relativistic heavy-ion collisions at the LHC. PhD thesis, Utrecht University, 2013.
- [76] S. Voloshin and Y. Zhang. Flow study in relativistic nuclear collisions by Fourier expansion of Azimuthal particle distributions. *Z. Phys.*, C70:665–672, 1996.
- [77] Sergei A. Voloshin. Toward the energy and the system size dependence of elliptic flow: working on flow fluctuations, 2006.
- [78] Sergei A. Voloshin, Arthur M. Poskanzer, and Raimond Snellings. Collective phenomena in non-central nuclear collisions. *Landolt-Bornstein*, 23:293–333, 2010.
- [79] Xin-Nian Wang and Miklos Gyulassy. hijing: A monte carlo model for multiple jet production in pp, pA, and AA collisions. *Phys. Rev. D*, 44:3501–3516, Dec 1991.
- [80] Xin-Nian Wang and Miklos Gyulassy. HIJING: A Monte Carlo model for multiple jet production in p p, p A and A A collisions. *Phys. Rev.*, D44:3501–3516, 1991.
- [81] C. S. Wu, E. Ambler, R. W. Hayward, D. D. Hopps, and R. P. Hudson. Experimental test of parity conservation in beta decay. *Phys. Rev.*, 105:1413–1415, Feb 1957.
- [82] Bin Zhang. ZPC 1.0.1: a parton cascade for ultrarelativistic heavy ion collisions. *Computer Physics Communications*, 109(2-3):193–206, apr 1998.
- [83] G Zweig. An SU₃ model for strong interaction symmetry and its breaking; Version 2. page 80 p, Feb 1964. Version 1 is CERN preprint 8182/TH.401, Jan. 17, 1964.

Samenvatting

Het bestuderen van hoogenergetische partons in botsingen van zware ionen en van protonen kan ons inzicht bieden in de sterke kracht. Deze restanten van hoogenergetische botsingen fragmenteren en hadronizeren in een sproei van partonen, zogenaamde jets, die ook duidelijk zichtbaar zijn in de verdelingen van de geproduceerde deeltjes. Bij een botsing van zware ionen wordt deze jet vervormd in een proces genaamd ‘jet quenching’, waarbij het parton en zijn fragmentatieproducten interacties aangaan met het Quark Gluon Plasma (QGP). In dit proces wisselen de partons uit de jet energie uit met het QGP, waarbij ze gemiddeld genomen energie verliezen, waarbij de geometrische vorm en het energieprofiel van de sproei van partonen wijzigt. Intuïtief zou men verwachten dat de effecten van het quenching schalen met de totale afstand die een parton door het medium aflegt. Een mogelijke wijze om dit effect te meten gebruikt de van nature onstane azimuthale asymmetrie in niet-centrale zware-ionenbotsingen. De elliptische flow die waargenomen wordt in deze botsingen zorgt voor meer deeltjesproductie in het botsingsvlak. De mate van quenching zou dus af moeten hangen van of de jet in het botsingsvlak ligt of er loodrecht op staat.

In dit werk wordt een meting gepresenteerd naar het verschil tussen jets afhankelijk van de hoek met het botsingsvlak voor drie gelijke boogsectoren. Dit wordt gedaan met behulp van het bestuderen van de correlaties tussen paren van hadronen. Bij kleine onderlinge hoeken zit een bijdrage van jets, al kan er zeker bij lage energie een relatief hoge achtergrond aanwezig zijn. Hiervoor wordt een model gebruikt dat de combinatorische achtergrond in drie sectoren aan elkaar verbindt. Hierbij wordt extra aandacht geschenken aan de correlaties tussen de symmetrievlakken van de botsing. Dit model is getest in een abstract Monte Carlo model waar gebruik wordt gemaakt van een bootstrap om de gemiddelde waarde en onzekerheden van de parameters uit te rekenen. Deze methodiek blijkt noodzakelijk om de juiste onzekerheden te achterhalen. Bij het gebruik daarvan kunnen de aan het model aangerijkte parameters nauwkeurig gereproduceerd worden.

Daarna wordt hetzelfde achtergrondmodel gebruikt in een analyse van de 2011 ALICE data over lood-lood botsingen. Verscheidene tekenen geven blijkt dat het reactievak afhankelijke achtergrond (PDF) model de achtergrond niet zo goed omschrijft als verwacht op basis van het abstracte Monte Carlo model, met name voor lagere transversale impuls van de geassocieerde deeltje ($p_{T,a}$). Er zijn verscheidene controles uitgevoerd om te kijken of binnen de grenzen van het PDF model deze spanning

opgelost kon worden. De resultaten voor de jet piek aan de nulzijde kunnen echter niet consistent gemaakt worden met de meer betrouwbare methode van het aftrekken van de achtergrond bij grote $\Delta\eta$ (LDE model), behalve voor $p_{T,a} > 3$ GeV/c aan de nulzijde en $p_{T,a} > 4$ GeV/c voor de pi-zijde. Aangezien een analyse van de piek aan de pi-zijde niet mogelijk is met het LDE model, en aangezien het PDF model niet werkt bij hoge impuls, waar de achtergrond te klein voor een betrouwbare schatting, wordt ook een model gebaseerd op een Fourier analyse rond de nulzijde bekeken. Dit model produceert ook significant andere resultaten in het lage impulsbereik. Voor al deze modellen wordt de I_{plane} parameter geïntroduceerd, een fractie van de bijdrage van geassocieerde deeltjes met een hoog-energetisch deeltje dat een bepaalde oriëntatie heeft tot het reactievlak, gedeeld door de bijdrage van geassocieerde deeltjes met een hoog-energetisch deeltje dat alleen op impuls geselecteerd wordt. Een vrijwel identieke analyse wordt ook uitgevoerd op een AMPT Monte Carlo model, waar dezelfde inconsistenties optreden voor lagere $p_{T,a}$.

Voor zowel de AMPT Monte Carlo en de ALICE data kunnen we concluderen dat de LDE resultaten tussen de Fourier en de PDF resultaten inzitten. De verschillen tussen deze methoden zijn significant in verhouding tot de statistische onzekerheid. Bij een hoge $p_{T,a}$ wordt geen verschil gevonden tussen de I_{plane} parameters binnen de huidige experimentele en theoretische randvoorwaarden. Ook in AMPT-model is het verwachte effect van de padlengte-afhankelijkheid op het geassocieerde aantal deeltje klein en niet meetbaar binnen de huidige onzekerheden. Bij lagere $p_{T,a}$ zijn de verschillen tussen achtergrondmodellen te groot om conclusies te trekken. Om over dit energetische bereik ook een uitspraak te doen is een uitbreiding van het achtergrondmodel nodig, en verscheidene mogelijke verbeteringen worden besproken.

Summary

The study of high-energy partons in heavy ion collisions and proton collisions can provide us with an insight into the strong interaction. These products of hard collisions fragment and hadronize in a parton shower, so-called jets. In heavy ion collision the parton shower is modified in a process called quenching, wherein the parton and its products are interacting with a Quark Gluon Plasma (QGP). In this process the parton shower transfers energy to the QGP, on average ‘losing’ energy, changing the geometric shape and energy profile. Intuitively one would expect the quenching effects to scale with the path length in the medium. A possible observable which could measure this path length dependence uses the naturally occurring azimuthal differences in non-central heavy ion collisions. The elliptic flow observed in these events is linked to the second order event plane. Whether jets are in the direction of this event plane or perpendicular to it influences possibly the amount of quenching.

In this work the difference between jets was studied depending on their angle to the event plane for three different equally large bins. This was done with the help of the study of correlations between pairs of hadrons. When the angles between them are small there is a contribution that can be attributed to jets, even though at low energies a sizeable background is present as well. This is subtracted with a model that connects the combinatorial background in the three plane-bins. Special attention was paid to the roll of the correlations between event planes. This model was tested in a Toy Monte Carlo model where a bootstrap was used to compute the average value and the errors. This procedure is necessary to establish the correct uncertainties, and is able to reproduce the input parameters reliably.

Then the same background model was used in an analysis of the 2011 ALICE data of Lead-Lead collisions. Here several signs are present that the plane dependent trigger background fit (PDF) model does not perform as well as expected on basis of the Toy Monte Carlo Model, especially at lower transverse momenta of the associated particle ($p_{T,a}$). Several cross checks have been performed to see whether this difference could be explained within the confines of the PDF model by changing the event plane correlation or resolution parameters. But results for the near-side jet peak are not consistent with the more reliable method of large $\Delta\eta$ (LDE) subtraction, except for $p_{T,a} > 3$ GeV/c on the near-side and $p_{T,a} > 4$ GeV/c on the away side. Since an analysis of the away-side is not possible with the LDE model, and the PDF model is not suitable for the high momentum range where statistics is low, a model based on a

Fourier analysis of the near-side range is introduced. This reproduces different results as well in the low momentum region. For all these models the I_{plane} parameters are introduced, a fraction of the associated particle yield from a trigger that has a specific angle to the event plane through a associated particle yield from a trigger without selection. A near-identical analysis is performed in a AMPT Monte Carlo model, where the same inconsistencies are present for the lower $p_{T,a}$.

For both the AMPT Monte Carlo and the ALICE data we can conclude that the LDE results are mostly in between the Fourier and the PDF results. The differences between these methods are significant with respect to the statistical uncertainty. At high $p_{T,a}$ no difference could be found within the current experimental and theoretical constraints. The expected effect of the path length dependence in the AMPT model is also small, and not distinguishable within current uncertainties. At lower $p_{T,a}$ the differences between background models are too large to draw conclusion. In order to test this at these energies some extension of the background model is necessary, and several of these possible improvements are discussed.

Acknowledgements

First of all, I would like to thank my daily supervisor dr. ir. Marco van Leeuwen and promotor prof. dr. Raimond Snellings for the opportunities they have given me, and the many interesting science discussions we have had. I knew very little about particle physics when I started my PhD, and a lot of the knowledge contained in this work has been passed on to me by you. Thanks to you I have learned a lot about particle physics, research in general, and even about myself.

And also an invaluable thanks to Floris van Doorn, who helped me when I was completely stuck. Your listening ears have had to deal with hearing a lot of complaining, excuses, and repetition. You have been the arbiter of my progress, but were never judgemental, and somehow you always had very valuable advice for a subject you supposedly do not know that much about.

Some people can help while they might not be aware they are doing so. Jacopo Margutti, you probably have no idea how much your words have meant to me, and how they helped me to keep on going. Thank you for doing the right thing, in generally everything.

Thank you to all Utrecht and Nikhef colleagues that made working there fun. Redmer, Misha, Davide, Mike, Panos, Thomas, Alessandro, Monique, Rihan, Barbara, Auro, Lennart, Jasper, Jay, Henrique, Christina, Luuk, Chiara, Nagmeh, Deepa, You, and all the others.

Furthermore I would like to thank several people in the ALICE collaboration: Marta Verweij, for her work on the hybrid tracks, Jan Fiete Grosse-Oeseringhaus, for his help and advice on the existing code for dihadron correlations, Satyajit Jena, for running more trains on time than the Dutch railway, Victor Gonzalez, for his advice on subsampling of grid results, David Chinellato, for the percentile distribution of the impact parameter, and lastly Christine Natrass, Michael Oliver, and Raymond Ehlers, for the useful advice and discussion via e-mails. And a further thanks to everyone from the ALICE collaboration that I forgot to mention.

Furthermore I'd like to thank Danny van Elswijk, Bas de Groot and many other colleagues at Statistics Netherlands for their giving me moral support and time to finish this work.

I would advise everyone to thank Esger, it's thanks to L^AT_EX and him that this

document is so easy on your eye.

Bedankt aan al mijn vrienden, die mijn gemopper aangehoord hebben, en er ook waren op de momenten dat ik niet te hard moest werken. Of het nu tijdens een lange avond beschavingen bouwen was, of tijdens het simuleren van een pandemie in een pandemie, of in een klasieke oudheid met aardappels, jullie waren altijd goed voor een opbeurende gezelligheid.

En als allerlaatste heel veel dank aan mijn familie. Rieta, Wilken, dankjulliewel voor alle tijd die jullie met de kinderen doorbrengen, en voor alle steunende woorden.

Pap, mam, jullie hebben zo'n groot deel van mij gevormd, en dan komt daar iets uit voort dat voor jullie waarschijnlijk vrijwel onleesbaar en onherkenbaar is. Ik hoop dat dat niet als een deprimerende metafoor voor het ouderschap voelt. Jullie hebben niet heel veel hoeven te betekenen in de totstandkoming van dit proefschrift, en dat is precies wat jullie hebben betekent voor dit proefschrift. Het is niet alleen in de wetenschap dat we op de schouders van reuzen staan. Dankjulliewel.

Annelies, je hebt me de afgelopen jaren heel veel steun, tijd en geduld geschenken, zelfs als je die soms zelf ook nodig had. Je hebt veel meer betekend voor mijn PhD dan ik voor jouwe, en daar ben ik je erg dankbaar voor. En Leander, Athena en Amarin, jullie zijn een groot obstakel geweest bij de voortgang, maar tegelijk ook een zeer krachtige brandstof. Voor alle tijd en slaap die jullie van mijn promotie afsnoepten, kreeg ik waanzinnig veel geluk en doorzettingsvermogen terug uit jullie lieve lachjes en warme knuffels.

Curriculum Vitae

Darius Keijdener

15-10-1989 Born in Utrecht, the Netherlands

Education

2011-2013 *Msc. Theoretical Physics*
Utrecht University, Utrecht, the Netherlands

2007-2011 *Bsc. Physics and Mathematics (simultaneously)*
Utrecht University, Utrecht, the Netherlands

2001-2007 *Gymnasium beta*
Stedelijk Gymnasium Johan van Oldebarneveldt,
Amersfoort, the Netherlands

Work Experience

2018-present *Statistical Researcher*
Statistics Netherlands (Centraal Bureau voor de Statistiek),
the Hague, the Netherlands

2013-2017 *PhD Candidate*
Institute for Subatomic Physics / GRASP
Utrecht University, Utrecht, the Netherlands

